Karlsruher Institut für Technologie

Schriftenreihe
Kontinuumsmechanik im Maschinenbau

30

Johannes Keursten

Thermoviscoelastic Modeling of Thermoplastic Polymers

KIT Scientific Publishing

Johannes Keursten

Thermoviscoelastic Modeling of Thermoplastic Polymers

Schriftenreihe
Kontinuumsmechanik im Maschinenbau
Band 30

Karlsruher Institut für Technologie (KIT)
Institut für Technische Mechanik
Bereich Kontinuumsmechanik

Hrsg. Prof. Dr.-Ing. habil. Thomas Böhlke

Eine Übersicht aller bisher in dieser Schriftenreihe erschienenen Bände finden Sie am Ende des Buchs.

Thermoviscoelastic Modeling of Thermoplastic Polymers

by
Johannes Keursten

KIT Scientific Publishing

Karlsruher Institut für Technologie
Institut für Technische Mechanik
Bereich Kontinuumsmechanik

Thermoviscoelastic Modeling of Thermoplastic Polymers

Zur Erlangung des akademischen Grades eines Doktors der Ingenieurwissenschaften von der KIT-Fakultät für Maschinenbau des Karlsruher Instituts für Technologie (KIT) genehmigte Dissertation

von Johannes Keursten, M.Sc.

Tag der mündlichen Prüfung: 19. Dezember 2024
Hauptreferent: Prof. Dr.-Ing. Thomas Böhlke
Korreferent: Prof. Dr. Jeffrey T. Wood
Korreferentin: Prof. Dr. rer. nat. Sabine Enders

Impressum

KIT Scientific Publishing

Karlsruher Institut für Technologie (KIT)
KIT Scientific Publishing
Straße am Forum 2
D-76131 Karlsruhe

www.bibliothek.kit.edu/ksp.php | E-Mail: info@ksp.kit.edu | Shop: www.ksp.kit.edu

Print on Demand 2025 – Gedruckt auf FSC-zertifiziertem Papier

ISSN 2192-693X
ISBN 978-3-7315-1422-0
DOI 10.5445/KSP/1000179538

Publications

This doctoral thesis is partially based on journal articles that are already published. The articles are listed in the following:

- Loredana Kehrer, Johannes Keursten, Valerian Hirschberg, Thomas Böhlke, 2023.
  Dynamic mechanical analysis of PA 6 under hydrothermal influences and viscoelastic material modeling.
  Journal of Thermoplastic Composite Materials 36 (11), 4630-4664.
  https://doi.org/10.1177/08927057231155864[1]

- Johannes Keursten, Loredana Kehrer, Thomas Böhlke, 2023.
  Linear and nonlinear thermoviscoelastic behavior of polyamide 6.
  Proceedings in Applied Mathematics and Mechanics 22 (1), e202200145.
  https://doi.org/10.1002/pamm.202200145[2]

Each section or paragraph that is based on a section or paragraph from one these journal articles is annotated with the corresponding reference. The extracts from the individual publications are not mixed up. The term *based on* referes to the following types of adaption:

  - Adaption of the numbering of equations, figures and tables
  - Change of the citation style

[1] Reprinted by permission of SAGE Publications. The article is published under the **CC-BY-NC 4.0** license, cf. https://creativecommons.org/licenses/by-nc/4.0/deed.

[2] Reproduced by permission of Wiley-VCH GmbH. The article is published under the **CC-BY 4.0** license, cf. https://creativecommons.org/licenses/by/4.0/deed.

- Changes of formula symbols
- Minor linguistic changes
- Some sentences are omitted or added

Figures and tables that are based on the publications are labeled with the corresponding reference. All figures are at least adjusted regarding their size and fontsize. Further changes are explicitely stated.

In addition, the author contributed to the following journal article that is not used within the thesis:

- Alexander Dyck, Leonhard Groß, Johannes Keursten, Loredana Kehrer, Thomas Böhlke, 2024.
  Modeling and FE simulation of coupled water diffusion and viscoelasticity in relaxation tests of polyamide 6.
  Continuum Mechanics and Thermodynamics 36, 935-953.
  https://doi.org/10.1007/s00161-024-01305-4

Zusammenfassung

Thermoplastische Polymere kommen in einer Vielzahl von industriellen Anwendungen zum Einsatz, unter anderem als Matrixmaterial in faserverstärkten Werkstoffen. Ein zentrales physikalisches Phänomen bei Thermoplasten ist der Glasübergang. Im Temperaturbereich des Glasübergangs ist eine signifikante Änderung der thermomechanischen Materialeigenschaften sowie ein ausgeprägt prozessabhängiges Materialverhalten zu beobachten, was in Materialmodellen zu berücksichtigen ist.
In dieser Arbeit wird zunächst die Theorie der linearen Thermoviskoelastizität ausführlich beschrieben. Die allgemeinen thermoviskoelastischen Materialmodelle werden im Rahmen der linear irreversiblen Thermodynamik hergeleitet. Zur Darstellung des mechanischen Verhaltens werden die generalisierten Maxwell- und Kelvin-Modelle verwendet, erweitert um thermische Ausdehungselemente. Es wird gezeigt, dass sich die beiden Modelle in ihren natürlichen Zustandsvariablen unterscheiden. Je nach Lastfall ist eines der beiden Modelle besser geeignet. Eine Umrechnungsmethode zwischen den Materialparametern der beiden Modelle einschließlich thermischer Ausdehnungselemente, basierend auf bekannten numerischen Umrechnungen der rein viskoelastischen Modelle, wird dargestellt. Zur Formulierung des prozessabhängigen kalorischen Modells wird eine Analogie zwischen Spannungsrelaxation und Entropierelaxation genutzt.
Anschließend wird der viskoelastische Teil des Modells auf Temperatur-Frequenz-Versuche von Polyamid 6 angewandt. Betrachtet werden verschieden große Lasten und verschiedene Konditionierungszustände. Die Konstruktion von Masterkurven mithilfe der erweiterten Zeit-Temperatur-

Verschiebung wird ausführlich diskutiert. Der Einfluss der unterschiedlichen Wassergehalte aufgrund unterschiedlicher Konditionierung wird durch eine feuchteabhängige Referenztemperatur berücksichtigt. Die Masterkurven erlauben Rückschlüsse auf die Grenzen der linearen Viskoelastizität mit erweiterter Zeit-Temperatur-Verschiebung. Zusätzlich wird die Parameteridentifikation für ein generalisiertes Maxwell-Modell detailiert beschrieben.
Zuletzt wird der kalorische Teil des Modells auf Temperaturverläufe der Wärmekapazität von Polystyrol in der Umgebung des Glasübergangs angewandt. Betrachtet wird ein im Vergleich zur Literatur vereinfachtes Modell mit einer inneren Temperatur als interne Variable. Das Modell berücksichtigt die Temperaturabhängigkeit der Relaxationszeit durch eine WLF-Gleichung. Zudem wird eine explizite Ratenabhängigkeit ergänzt. Das qualitative Verhalten des Modells und die physikalische Interpretation der inneren Temperatur werden veranschaulicht. Außerdem erfolgt eine Parameteridentifikation anhand von Aufheizkurven. Dabei wird auch beschrieben, wie sich die Anfangswerte der inneren Temperatur ohne Kenntnis der Vorgeschichte numerisch aus experimentellen Daten berechnen lassen. Die Approximation des prozessunabhängigen Verhaltens im Glas- und Gleichgewichtszustand wird ebenfalls behandelt.

Summary

Thermoplastic polymers are used in a variety of industrial applications, e.g., as a matrix material in fiber-reinforced materials. A central physical phenomenon in thermoplastics is the glass transition. In the glass transition regime, a significant change of thermomechanical material properties and a pronounced process-dependent material behaviour is observed, which must be taken into account in material modeling.
In this work, first, the theory of linear thermoviscoelasticity is described in detail. The general thermoviscoelastic material models are derived within the framework of linear irreversible thermodynamics. Generalized Maxwell and Kelvin models are used to model viscoelastic behaviour and are extended by thermal expansion elements. It is shown that the models differ in their natural state variables. Depending on the load case, one of the two models is more suitable. A conversion method between the parameters of the two models including thermal expansion elements is presented as extension of known numerical conversion methods of the purely viscoelastic models. To formulate the process-dependent caloric model, an analogy between stress relaxation and entropy relaxation is used.
Next, the viscoelastic part of the model is applied to temperature-frequency tests of polyamide 6. Different load sizes and conditioning states are considered. The construction of master curves using extended time-temperature superposition is discussed in detail. Using a moisture-dependent reference temperature, the influence of different water contents due to different conditioning states is taken into account. The master curves give implications on the limits of linear viscoelasticity with

extended time-temperature superposition. In addition, the parameter identification for a generalized Maxwell model is discussed in detail.
Last, the caloric part of the model is applied to heating and cooling curves of the heat capacity of polystyrene in the vicinity of the glass transition. Compared to the literature, a simplified model with an internal temperature as an internal variable is considered. The model takes into account the temperature-dependency of the relaxation time by means of a WLF equation. An explicit rate-dependency of the relaxation time is also considered. The qualitative behaviour of the model and the physical meaning of the internal temperature are illustrated. In addition, a parameter identification based on heating curves is conducted. For this purpose, it is shown how the initial values of the internal temperature can be calculated numerically from experimental data although the temperature history of the sample is unknown. The approximation of the process-independent behaviour in the glassy and equilibrium state is also discussed.

Acknowledgments

First and foremost, I would like to express my gratitude to my supervisor Prof. Thomas Böhlke. His guidance, his profound knowledge, and his advices and critical comments have strongly supported my doctoral research. During my studies, his lectures aroused my interest in continuum mechanics and my interest in pursuing a doctorate in this research field.

I would like to thank Prof. Jeff Wood and Prof. Sabine Enders for reviewing my doctoral thesis and for their interest in my work. I would also like to thank Prof. Britta Nestler for chairing my doctoral exam.

I thank Loredana Kehrer for her support and helpful advices, especially at the beginning of my doctoral research. I also thank her for the experimental characterization of PA6 and the constructive collaboration on the joint publication. I would also like to thank all other colleagues during my time at ITM, in particular Alex, Max, Tobias, Benedikt, Celine, Johannes and Claudius. Diverse discussions during coffee breaks, at lunch or at conferences have always enriched my time at the institute. Special thanks go to Ute, Ariane and Tom for their support and assistance regarding administrative tasks and problems.

I am also grateful to have been a doctoral student in the international research training group IRTG 2078. The atmosphere during meetings and discussions with all members of the IRTG was always pleasant and constructive.

Last but not least, I would like to express my deep gratitude to my family. Their helpfulness, patience and forbearance are always a great support for me.

The research documented in this doctoral thesis has been funded by the German Research Foundation (DFG) within the International Research Training Group *Integrated engineering of continuous-discontinuous long fiber reinforced polymer structures* (GRK 2078). The support by the German Research Foundation (DFG) is gratefully acknowledged.

Karlsruhe, April 2025 Johannes Keursten

Contents

Notation, symbols and abbreviations

Notation

a, A, α	Scalar quantity
$\boldsymbol{a}$	First-order tensor
$\boldsymbol{\alpha}, \boldsymbol{A}$	Second-order tensor
$\boldsymbol{A}^{\circ}$	Spherical part of a second-order tensor
$\boldsymbol{A}'$	Deviatoric part of a second-order tensor
$\mathbb{A}$	Fourth-order tensor
$\underline{a}$	Tuple or vector
$\underline{\underline{A}}$	Matrix
$\mathcal{L}(\cdot)$	Laplace transformation
$\mathrm{tr}(\boldsymbol{A})$	Trace of a second-order tensor
$\widetilde{(\cdot)}$	Material parameter corresponding to a GKM
$\widehat{(\cdot)}$	Energetic part of stress or entropy
$\widetilde{(\cdot)}$	Non-energetic part of stress or entropy
$(\cdot)_{\mathrm{c}}$	Caloric part of energy or entropy
$(\cdot)_{\mathrm{m}}$	Mechanical part of energy, stress or entropy
$(\cdot)_{\mathrm{ce}}$	Equilibrium caloric part of energy or entropy
$(\cdot)_{\mathrm{cv}}$	Viscocaloric part of energy or entropy
$(\cdot)_{\mathrm{me}}$	Elastic part of energy, stress or entropy
$(\cdot)_{\mathrm{mv}}$	Viscoelastic part of energy, stress or entropy

Latin letters

$\boldsymbol{a}$	Acceleration
a', a''	Residual weight factors of E' and E''
a_θ	Horizontal shift function
$\boldsymbol{b}$	Volume force density
$\mathcal{B}$	Basic fields
b_θ	Vertical shift function
C	Caloric material parameter
$\mathbb{C}$	Stiffness tensor
c_1, c_2	WLF parameters
c_p	Isobaric heat capacity
c_p^{eq}	Equilibrium heat capacity
c_p^{gl}	Glassy heat capacity
c_p^{red}	Reduced heat capacity
c_v	Isochoric heat capacity
$d(\dot{\theta})$	Rate-dependency function
d_1, d_2	Parameters of the rate-dependency function
e	Specific internal energy
$\boldsymbol{e}$	Unit vector
E, E_i	Young's modulus
$E(t)$	Relaxation modulus
E'	Storage modulus
E''	Loss modulus
E^*	Dynamic modulus
$\mathcal{E}$	Set of input parameters
f	Frequency
$\underline{f}$	Evolution equations
$\boldsymbol{F}$	Deformation gradient
f_V	Fractional free volume
g	Specific free enthalpy
G, G_i	Shear modulus
$G(t)$	Shear relaxation modulus

$\boldsymbol{g}$	Temperature gradient
h	Specific enthalpy
$\boldsymbol{H}$	Displacement gradient
$H(t)$	Heaviside step function
$J(t)$	Bulk creep compliance
K, K_i	Bulk modulus
$K(t)$	Bulk relaxation modulus
$\mathcal{K}$	Constitutive properties
$\boldsymbol{L}$	Velocity gradient
$\boldsymbol{I}$	Unity tensor
$\mathcal{M}$	Constitutive equations
m_1, m_2	Slopes of glassy and equilibrium heat capacity
N	Order of GMM or GKM
p	Pressure
$p_\mathrm{e}, p_\mathrm{v}$	Elastic pressure, viscoelastic pressure
p_s	Entropy production
p_Ψ	Production term (balance equation)
$\mathbb{P}_1$	Symmetric, spherical projector
$\mathbb{P}_2$	Symmetric, deviatoric projector
$\boldsymbol{q}$	Heat flux vector
$\boldsymbol{q}_\Psi$	Flux term (balance equation)
s	Specific entropy
s_Ψ	Supply term (balance equation)
t	Time
$\boldsymbol{u}$	Displacement vector
v, v_0	Specific volume, initial specific volume
$\boldsymbol{v}$	Velocity vector
V	Volume
V_f	Free volume
$\mathbb{V}$	Viscosity tensor
w	Heat supply
$\boldsymbol{x}$	Current position of a material point

$\boldsymbol{X}$	Initial position of a material point
$\underline{y}$	Thermodynamic driving forces
z	Reduced time
$\underline{z}$	Internal variables

Greek letters

α	Thermal expansion coefficient
$\boldsymbol{\alpha}$	Tensor of thermal expansion coefficients
β	Temperature-stress coefficient
$\boldsymbol{\beta}$	Tensor of temperature-stress coefficients
δ	Phase shift
$\Delta\varepsilon$	Strain amplitude
$\Delta\theta$	Temperature difference
$\Delta\sigma$	Stress amplitude
ε	Longitudinal strain
ε_0	Mean strain
ε^*	Complex strain
$\varepsilon_{\mathrm{v}i}$	Longitudinal viscous strain
$\varepsilon^{\mathrm{vol}}$	Volumetric strain
$\varepsilon_{\mathrm{e}i}^{\mathrm{vol}}$	Volumetric elastic strain
$\varepsilon_{\mathrm{v}}^{\mathrm{vol}}, \varepsilon_{\mathrm{v}i}^{\mathrm{vol}}$	Volumetric viscous strain
$\varepsilon_\theta, \varepsilon_{\theta i}$	Thermal strain
$\boldsymbol{\varepsilon}$	Infinitesimal strain tensor
$\boldsymbol{\varepsilon}_{\mathrm{v}i}$	Viscous strain tensor
ζ	Parameter of equilibrium heat capacity function
$\eta_i, \eta_{\mathrm{v}i}, \eta_{\mathrm{si}}$	Viscosity, volume viscosity, shear viscosity
θ	Temperature
θ_0	Reference temperature (regarding thermal expansion)
θ_{g}	Glass transition temperature
θ_{gi}	Interpolated glass transition temperature
θ_{ref}	Reference temperature (regarding TTS)

θ_i	Inflection point temperature
θ_m	Mid point temperature
θ_T	Transition temperature of equilibrium heat capacity
$\theta_\mathrm{v}, \theta_{\mathrm{v}i}$	Internal temperature
$\theta_{\mathrm{v}0}$	Initial internal temperature
λ, λ_i	Caloric relaxation time
$\boldsymbol{\kappa}$	Tensor of thermal conductivity
ν	Poisson's ratio
ξ, ξ_i	Caloric viscosity
ϱ, ϱ_0	Mass density, initial mass density
σ	Normal stress
σ_0	Mean stress
σ^*	Complex stress
$\boldsymbol{\sigma}$	Cauchy stress tensor
τ_i	Relaxation time
$\tau_{\mathrm{v}i}, \tau_{\mathrm{s}i}$	Volume relaxation time, shear relaxation time
φ	Equilibrium part of caloric free energy/free enthalpy
Φ	Dissipation potential
$\boldsymbol{\chi}$	Equation of motion
ψ	Specific free energy
Ψ	General field property
ω	Angular frequency

Abbreviations

DAM	Dry-as-molded
DMA	Dynamic mechanical analysis
DSC	Differential scanning calorimetry
GKM	Generalized Kelvin model
GMM	Generalized Maxwell model
PA6	Polyamide 6
PS	Polystyrene

RH	Relative humidity
TMA	Thermomechanical analysis
TTS	Time-temperature superposition
WLF	Williams-Landel-Ferry

Chapter 1

Introduction

1.1 Motivation

Polymeric materials are processed in a variety of industrial applications. Packaging, building and construction, automotive industry, or electronics are mentioned here as important examples (Menges et al., 2011). Advantageous characteristics of polymers are, e.g., low material and processing costs, good processibility, chemical resistance, electrical insulation properties, and high strength-mass or stiffness-mass ratios (Menges et al., 2011). From the latter, the lightweight potential of polymeric materials arises. The mechanical properties of polymers can be further improved by fiber reinforcements, e.g., carbon or glass fiber reinforcement (Böhlke et al., 2019; Görthofer et al., 2019).

A central physical phenomenon of polymers is the glass transition that is related with a significant change of thermomechanical properties and pronounced viscoelastic behavior (Ehrenstein, 2011). In this work, the specific focus is on thermoplastic polymers. Thermoplastics are processed above the glass transition. The application of thermoplastics usually takes place below the glass transition. However, semicrystalline thermoplastics can also be applied above the glass transition (Stommel et al., 2018). Thus, the glass transition and the related effects must be taken into account by thermomechanical models for the design of thermoplastic components. This work is intended to make a contribution to this from a fundamentals

orientated perspective. The transfer to selected specific problems should also be demonstrated. A detailed summary of the research objectives, the originalty of this work, and the outline of the thesis is given in the following.

1.2 Research objectives

Main objective of this thesis is the derivation and discussion of a complete theory of linear thermoviscoelasticity in a continuum mechanical framework. The considered constitutive models should include viscoelastic behaviour, thermal expansion and caloric behaviour under consideration of temperature-dependencies. A special focus is set on the analogy between the viscoelastic and the caloric models. In addition, the application of the thermoviscoelastic models for selected problems should be addressed. This means that the specific procedure for parameter identification from experimental data, the potential of linear models to reproduce this data and the limits of linear thermoviscoelastic models are to be discussed. In specific, the cyclic viscoelastic behaviour of polyamide 6 (PA6) under hydrothermal influences and the caloric behaviour of polystyrene (PS) during cooling and heating in the vicinity of the glass transition will be considered.

1.3 Originality

The consideration of thermoviscoelastic models in this work shows the following novelties:

Thermoviscoelastic theory. A detailed derivation of a thermoviscoelastic theory in a small strain setup setup based on linear irreversible thermodynamics is given. The terms *entropy relaxation* and *viscocaloric behavior*

are introduced and motivated. The analogy between viscoelasticity and entropy relaxation is strictly emphasized.

Generalized thermorheological models. The extension of the standard models of linear thermoviscoelasticity, generalized Maxwell and Kelvin models, by thermal expansion elements is discussed. It is shown that the models differ in the choice of their natural state variables and their natural thermodynamic potentials. An explicit expression of the free enthalpy for a generalized Kelvin model under volumetric deformations is given. The equivalence of generalized Maxwell model (GMM) and generalized Kelvin model (GKM), including thermal expansion, is shown. Furthermore, a conversion method between the two models is presented. Stiffnesses and viscosities can be converted using numerical methods from the literature. The conversion of the thermal expansion coefficients is then carried out by solving a linear system of equations.

Viscoelasticity of PA6 under hydrothermal influences. By an improved arc length minimization algorithm, extended time-temperature superposition (TTS) is applied to experimental data from cyclic tests of PA6 performed by dynamic mechanical analysis (DMA). Based on constructed master curves, limitations and restrictions of TTS and linear viscoelasticity, when considering PA6, are discussed and illustrated: the need for vertical shifts, restricted temperature and frequency ranges, and onsetting nonlinearity. The influence of moisture on the viscoelastic properties of PA6 is modelled by a moisture-dependent reference temperature. Furthermore, based on master curves, neglectable deviations between temperature-frequency tests performed with and without humidity control are observed.

Entropy relaxation of PS. An analytical formula to describe the heat capacity in the glassy and equilibrium state is adjusted to experimental

data. In addition, a simple model of entropy relaxation is fitted to experimental heating curves within the glass transition regime. The model uses an internal temperature with a relaxation time that depends on the temperature through a WLF equation. It is shown how the initial value of the internal temperature, when solving the evolution equation, can be calculated numerically without the need to know the temperature history of the material. The necessity for an additional dependency of the relaxation time on the temperature rate is motivated.

1.4 Outline of the thesis

The thesis is structured as follows. Chapter 2 summarizes the main fundamentals that are needed for this work. First, thermoplastic polymers are addressed with focus on thermoviscoelastic behavior and the glass transition. Second, the general framework of continuum mechanical material modeling is summarized. In Ch. 3, this framework is applied in order to derive constitutive equations for thermoviscoelastic problems including thermomechanical and caloric behavior. The mechanical and caloric parts of this thermoviscoelastic model are then applied in Ch. 4 and 5, respectively. Viscoelastic behavior of PA6 under hydrothermal influences is addressed in Ch. 4. Based on experimental data, the GMM and time-temperature-superposition are applied. In Ch. 5, the caloric part of the model is addressed. This viscocaloric model is applied and adjusted to experimental measurements on PS. At the end, a conclusion of the thesis is given in Ch. 6.

1.5 State of the art

Linear viscoelasticity. The mechanical behavior of thermoplastic polymers is characterized by pronounced viscoelastic effects (Ehrenstein, 2011;

Stommel et al., 2018). This must be taken into account by the corresponding mechanical models. Detailed overviews on the theory of viscoelasticity can, e.g., be found in Ferry (1980), Tschoegl (1989) and Brinson and Brinson (2015). The integral formulation of linear viscoelasticity is given by a convolution integral, the Boltzmann superposition integral (Schapery, 1969). Differential formulations are given by rheological connections consisting of linear spring and dashpot elements. Maxwell model and Kelvin-Voigt model serve as basic models (Tschoegl, 1989). The Maxwell model allows to describe stress relaxation, whilst the Kelvin-Voigt model allows to describe creep. In both models, only one characteristic time is defined (Serra-Aguila et al., 2019). By series connections of Kelvin-Voigt elements, the GKM arises, whilst by parallel connection of Maxwell elements, the GMM arises. These generalized rheological models display a discrete distribution of relaxation or retardation times (Brinson and Brinson, 2015). Within the Boltzmann superposition integral, GMM and GKM correspond to a Prony series representation (Serra-Aguila et al., 2019). By using fractional derivatives, the spring-dashpot connections can be further generalized in order to reduce the number of material parameters. An overview on these fractional models of linear viscoelasticity was given by Arikoglu (2014). The thermodynamical cosistency of the fractional models was, e.g., shown by Lion (1997). All mentioned models can also be applied for three-dimensional problems in equivalent formulations for both isotropic and anisotropic behavior (Gutierrez-Lemini, 2014). In case of isotropy, a decomposition into a deviatoric and a spherical part is used (Brinson and Brinson, 2015). Corresponding to the relations regarding the moduli and Poisson's ratio in linear elasticity, similar expressions can be derived for the time-dependent viscoelastic properties (Tschoegl et al., 2002b). For an overview on various isotropic, linear viscoelastic models, the reader is referred to Chen et al. (2012).

Parameter identification. The parameter identification of a generalized rheological model from experimental data is known as an ill-posed problem if time constants and stiffnesses are to be determined (Honerkamp and Weese, 1989). A disussion on a regularization of the problem was given by Honerkamp and Weese (1990). As standard approach, a logarithmic distribution of time constants can be prescribed to solve this problem (Bradshaw and Brinson, 1997). To fit experimental data appropriately, at least one time constant per considered time decade should be used (Ghobadi et al., 2015). Jalocha et al. (2015) showed how an optimal set of time constants can be identified. Commonly, the identification of the corresponding stiffnesses is conducted by least-squares optimization (Jalocha et al., 2015).

Conversion of generalized rheological models. Depending on the load case, either the GMM or the GKM can be more adequate. Thus, a conversion method is of interest. In general, both models are equivalent. This can be shown by deriving a single ordinary differential equation (ODE) for both models (Gutierrez-Lemini, 2014). Furthermore, the relations between the general viscoelastic functions, e.g., relaxation modulus and creep compliance, are well known (Ferry, 1980; Brinson and Brinson, 2015). However, the explicit conversion between those functions and thus, between GMM and GKM, is a non-trivial problem (Serra-Aguila et al., 2019). In literature, explicit analytical conversion formulas can only be found for first and second order models (Krawietz, 1986; Serra-Aguila et al., 2019). Furthermore, there are various studies on numerical methods. Park and Schapery (1999) showed a numerical method based on Prony series where the target time constants are prescribed. The method is applicable in time, frequency and Laplace domain. The same authors introduced an approximate analytical method where the Prony series representation is not needed (Schapery and Park, 1999). The numerical interconversion method by Sorvari and Malinen

(2007) evaluates the convolution integral of relaxation modulus and creep compliance. Therefore, a regularization scheme is needed. Luk-Cyr et al. (2013) showed a closure based on the Prony series representation. The method is applicable for one-dimensional and three-dimensional models regardless of the material symmetry. Thermodynamical consistency is ensured. The method by Loy et al. (2015) is also based on the Prony series representation. Time-constants are calculated numerically. Then, the Prony series coefficients are given by analytical formulas. With focus on experimental characterization, Nikonov et al. (2005) suggested an approach how relaxation modulus and creep compliance could be identified from a single experiment, the spring-loading experiment. The method relies on an iterative numerical scheme.

Nonlinear viscoelasticity. In continuum mechanics, there are two types of nonlinearities: nonlinearity due to large deformations (geometric nonlinearity) and nonlinearity due to nonlinear constitutive equations (material nonlinearity), cf. Brinson and Brinson (2015). Generalized rheological models, that are formulated within a finite strain framework, correspond to the former, cf., e.g., Kaliske and Rothert (1997), Bonet (2001) or Johlitz et al. (2007). Nonlinear viscoelastic material behavior can, e.g., be identified by nonlinear isochronous stress-strain curves from creep or tensile tests (Bertilsson and Jansson, 1975; Papanicolaou et al., 2008; Starkova et al., 2011). In cyclic testing, nonlinear viscoelastic behavior leads to the presence of higher harmonics (Cho et al., 2005; Ewoldt and Bharadwaj, 2013; Hirschberg et al., 2020). Nonlinear viscoelastic constitutive equations, according to Brinson and Brinson (2015), can be classified into four types. The simplest approach is to use load-dependent parameters for the generalized rheological models (Troyer et al., 2012; Oskui and Hashemi, 2016; Xu et al., 2020). Nonlinear creep behavior of polymers can be modeled by power laws as, e.g., introduced by Findley et al. (1989) or Scott et al. (1995). Furthermore, integral descriptions of

nonlinear viscoelasticity can be found. Multi-integral descriptions, see Brinson and Brinson (2015), are rarely used due to their complexity. In contrast, the single-integral model by Schapery (1969) is often used to model nonlinear viscoelastic problems (Lai and Bakker, 1996; Beijer and Spoormaker, 2002; Crochon et al., 2010). Under certain assumptions, the integral Schapery model can be reformulated into a differential model, cf. Banks et al. (2011) and Zink et al. (2022).

Time-temperature superposition. Viscoelastic properties of thermoplastic polymers strongly depend on temperature (Ehrenstein, 2011; Stommel et al., 2018). The standard approach to model influences of temperature on viscoelastic behavior is thermorheological simplicity (Ferry, 1980). Regarding the generalized rheological models, this means that all time constants depend on temperature in the same way, expressed by a temperature-dependent factor (Dealy and Plazek, 2009). Within the Boltzmann superposition integral, thermorheological simplicity gives rise to a reduced time scale (Brinson and Brinson, 2015). An increase in temperature accelerates the viscoelastic effects. Furthermore, thermorheological simplicity allows for the construction of master curves from experimental data (Dealy and Plazek, 2009). Measurements of viscoelastic properties at various temperatures can be combined to a master curve at a reference temperature. Therefore, temperature-dependent shifts alongside the logarithmic time or frequency axis are applied. With that, the viscoelastic behavior can be predicted for a larger time or frequency range than covered by experiments (Diani et al., 2012; Hu et al., 2013). This concept is known as time-temperature superposition (Gutierrez-Lemini, 2014). Cole-Cole plots (Cole and Cole, 1941) and van Gurp plots (van Gurp and Palmen, 1998) can be utilized to check if thermorheological simplicity is valid (Guedes, 2011). In these plots, frequency-dependent viscoelastic properties are plotted against each other. If TTS is valid, the resulting plots show a smooth course. There are two standard approaches to model the temperature shift:

the WLF equation and an Arrhenius-type equation (Brinson and Brinson, 2015). The WLF equation was introduced by Williams et al. (1955) and is based on the free volume concept and the Doolittle equation (Doolittle and Doolittle, 1957) for temperature-dependent viscosities. For temperatures above and close to the glass transition, the WLF equation is often used, whilst for temperatures below the glass transition, the Arrhenius-type equation is used (Serra-Aguila et al., 2022). By Tschoegl et al. (2002a), a detailed overview on further approaches was given. In addition, the influence of pressure, that is modeled in a similar way, was discussed. If TTS is not valid, the material behaves thermorheological complex (Brinson and Brinson, 2015). This can, e.g., be caused by temperature-dependent moduli. In this case, however, master curves can still be constructed by adding vertical shifts (Guedes, 2011; Rouleau et al., 2013). By the Rousse model, a relation for the vertical shift factor, that depends on temperature and mass density, can be derived (Capodagli and Lakes, 2008; Dealy and Plazek, 2009). Brinson and Brinson (2015) discussed that the neglection of vertical shifts can lead to significant inaccuracies regarding the master curves.

Shift algorithms. For the construction of master curves, shift algorithms are used to avoid manual shifting. In literature, these methods can be mainly categorized into four types. The closed form algorithm, that was developed by Gergesova et al. (2011), Gergesova et al. (2016) and Oseli et al. (2016), gives an analytical solution for the shift factors. Therefore, a vanishing area between neighbouring curves is demanded. A combination of squared error optimization and polynomial interpolation was used in the methods by Honerkamp and Weese (1993), Sihn and Tsai (1999) and Alwis and Burgoyne (2006). The methods of Cho (2009), Bae et al. (2011) and Maiti (2016) use an arc length minimization for a numerical calculation of the shift factors. Further methods are based on numerical derivatives of the viscoelastic quantities, cf. Caracciolo and Giovagnoni

(1996), Hermida and Povolo (1994), or Naya et al. (2013). If vertical shifts are to be applied, horizontal and vertical shifts should be determined in subsequent steps (Bae et al., 2011).

Influence of moisture. The hydrophilic behavior of polyamides is well known in literature. For PA6, e.g., a maximum water uptake of about $10\mathrm{wt.\%}$ is observed (Domininghaus et al., 2012). The moisture content has a significant influence on the thermomechanical behavior of polyamides. A detailed review article on that was given by Venoor et al. (2021). In PA, water is a plasticizer that affects strength and stiffness (Lim et al., 1999; Jia et al., 2004; Kießling and Ihlemann, 2020). Furthermore, swelling due to water uptake must be taken into account (Monson et al., 2008; Sambale et al., 2021b; Wetzel et al., 2023). The water uptake also leads to an increased chain mobility. Thus, the glass transition is shifted to lower temperatures (Reimschuessel, 1978; Lim et al., 1999; Broudin et al., 2015). Reimschuessel (1978) suggested to express the moisture dependency of the glass transition temperature by an exponential function. Another approach is the Simha-Boyer equation where the inverse of the glass transition depends linearily on the water content (Arhant et al., 2016). Ishisaka and Kawagoe (2004) and Fabre et al. (2018) applied time-water content superposition to model the influence of moisture on viscoelastic properties. A WLF-type equation is used. Alternatively, Walter et al. (2010) suggested to use a moisture-dependent reference temperature within the temperature-dependent WLF equation. Various models regarding water diffusion in PA can be found in literature. Picard et al. (2008) and Preda et al. (2015), e.g., discussed diffusion models with non-constant diffusion coefficients. By Sambale et al. (2019) and Sambale et al. (2021a), moisture gradients in PA6 samples during water sorption were addressed and modeled by a nonlinear diffusion model. Furthermore, coupled models of viscoelasticity and diffusion can be found. Engelhard and Lion (2013) modeled the hydrothermomechanical properties of polymers close

to glass transition based on a quadratic expression of the free enthalpy. Sharma and coworkers developed coupled theories of nonlinear diffusion and viscoelasticity with moisture-dependent stiffnesses for small strains (Sharma et al., 2020) and for finite strains (Sharma and Diebels, 2021). By Kehrer et al. (2023), an unusual increase of stress in relaxation experiments was observed. The increase of the stress indicated a drying of the sample. A coupled model of viscoelasticity and diffusion was applied by Dyck et al. (2024) to reproduce this effect.

Volume and enthalpy relaxation. Especially during glass transition, pronounced process-dependent behavior is observed in thermal expansion and caloric behavior. This behavior is known as volume relaxation (or recovery) regarding thermal expansion and as enthalpy relaxation (or recovery) regarding caloric behavior (Kovacs et al., 1979). There is a large number of experimental studies that showed pronounced enthalpy relaxation in thermoplastic polymers by differential scanning calorimetry (DSC). The studies of Androsch et al. (2014) and Hammami et al. (2019) considering PA6, or Sakatsuji et al. (2013) and Tropin et al. (2015) considering PS are mentioned here as examples. The model by Kovacs et al. (1979) and the model by Tool (1945), Narayanaswamy (1971), and Moynihan et al. (1976) are often used to describe this behavior (Hodge, 1994). The former model is referred to as KAHR model, the latter as TNM model. Both KAHR and TNM model can be applied for volume recovery and enthalpy relaxation, cf. Simon et al. (2001) or Badrinarayanan et al. (2007). Kovacs et al. (1979) defined a differential equation for a departure from equilibrium in their model. This departure can be related to enthalpy or specific volume. The relaxation time of the KAHR model depends on temperature and the departure itself. These dependencies are multiplicatively seperated (Kovacs et al., 1979). To increase the number of degrees of freedom, the total departure can be decomposed into multiple fractional departures (Mittermeier, 2017). Argatov and Kocherbitov (2021) combined

the KAHR evolution equation with a relaxation time that only depends on temperature by an Arrhenius law. With that, a minimal model of enthalpy relaxation was derived and discussed. The TNM model refers to three models that build on each other. Tool (1945) introduced the concept of fictive temperature. The current fictive temperature defines the temperature at which the corresponding material would be in equilibrium (Simon et al., 2001). In Tool's model, an evolution equation for the fictive temperature is defined where the relaxation time depends on both temperature and fictive temperature itself (Mittermeier, 2017). Narayanaswamy (1971) and Moynihan et al. (1976) further developed the model. The basic concept of all three models is an evolution equation of the fictive temperature and a relaxation time, that depends on temperature and fictive temperature in a multiplicative decomposition. Thus, the models are summarized under the term TNM model (Mittermeier, 2017). The applications of the TNM model in more recent publications are based on the version by Moynihan et al. (1976). A Kohlrausch-Williams-Watt (KWW) function (Kohlrausch, 1854; Williams and Watts, 1970) is often used to model nonexponential behavior in the evolution of the fictive temperature, see, e.g., Hodge (1994) or Andreozzi et al. (2005). Furthermore, nonlinearity is taken into account by a weighting factor regarding temperature-dependency and dependency on fictive temperature (Tropin et al., 2015). A discussion on the TNM model regarding parameter identification was, e.g., given by Svoboda and Málek (2013). Simon (1997) and Liu et al. (2013) combined the TNM model with Fourier's law of heat conduction to model the influence of temperature gradients on enthalpy relaxation. For calculations of the evolution of the fictive temperature, a numerical scheme must be used, cf. Weyer et al. (2001). Three further models of enthalpy relaxation in polystyrene were addressed in the study of Tropin et al. (2015). In an extended TNM model, the relaxation time was formulated via the empirical Vogel-Fulcher-Tammann-Hesse expression (Vogel, 1921; Fulcher, 1925; Tammann and Hesse, 1926). This model was also used by Weyer et al. (2001) and Weyer et al. (2005) to describe the complex heat capacity

in temperature modulated DSC. By using the molecular-kinetic theory of Adam and Gibbs (1965), further approaches for the relaxation time of the TNM model were derived. The Adam-Gibbs theory was also used by Scherer (1984), Hodge (1991) and Ngai (1999). Last, Tropin et al. (2015) presented the Gutzow-Schmelzer method, see Gutzow et al. (2008), Tropin et al. (2011a) and Tropin et al. (2011b). This model is based on a liquid hole-lattice theory regarding the kinetics of glass transition. Mittermeier (2017) described volume recovery and enthalpy relaxation in a continuum mechanical framework. For the former, thermal expansion elements were added to a GMM of volumetric strains. To model enthalpy relaxation, internal temperatures were introduced. By an quadratic expression of the free energy and linear irreversible thermodynamics, evolution equations of the viscous strains and internal temperatures were derived. The relaxation times were modeled by an extended WLF equation leading to explicit dependencies on temperature and free volume or free entropy. A similar model was used by Lion et al. (2017). In this study, the relaxation times were assumed to only depend on temperature, modeled by the standard WLF equation.

Chapter 2

Fundamentals

2.1 Thermoplastic polymers

2.1.1 Classification of polymers

Polymers are organic materials that consist of large molecules, so called *macromolecules*. The chemical structure of these macromolecules is given by repeating units of monomers (Menges et al., 2011). Polymeric material are mainly classified into three types: *thermoplastics*, *thermosets* and *elastomeres*. The macromolecules of thermoplastic polymers are linear or branched chain molecules. Due to this strcuture, thermoplastic polymers are meltable. Thermoplastics with branched molecules are softer than those with linear molecules. Thermoplastic polymers can be further classified into semicrystalline and amorphous thermoplastics. Especially linear,

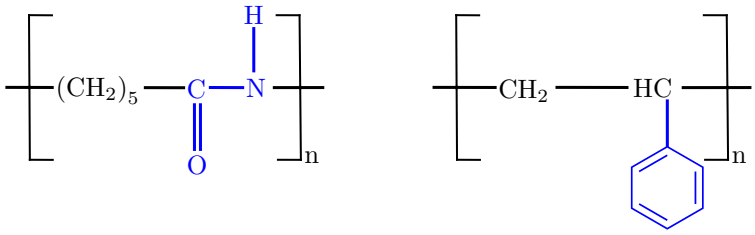

(a) Polyamide 6 **(b)** Polystyrene

Figure 2.1: Chemical structure of the thermoplastic polymers polyamide 6 and polystyrene

regularily ordered polymer chains allow for the growth of crystalline regions below the melting point. These crystalline regions then coexist with amorphous regions, giving a semicrystalline structure (Menges et al., 2011). For details regarding the crystallization in polymers, the reader is referred to Janeschitz-Kriegl (2018).
In contrast to thermoplastics, the macromolecules of thermosets and elastomeres show cross-linking between the molecular chains. The cross-linking in elastomeres is wide-meshed which leads to a softer material that allows for large elastic deformations. In thermosets, the cross-linking is close-meshed which leads to a stiffer and brittle material. Due to the cross-linking, a liquid state of thermosets and elastomeres does not exist (Menges et al., 2011).

2.1.2 Polyamide 6 and polystyrene

In this work, the thermoplastic polymers PA6 and PS are considered in specific. The chemical structures of the corresponding monomers are depicted in Fig. 2.1. The functional group of PA, the amide group, is marked in blue. As the monomer consists of $5 + 1$ carbon atoms, the name PA6 is derived. In PA6, crystallization is observed. A degree of crystallinity of up to 60% can be reached (Domininghaus et al., 2012). Furthermore, the hydrophilic characteristic of the amide group allows for a maximum water uptake of $10\text{wt.}\%$ (Domininghaus et al., 2012). The functional group of PS, the phenyl group, is also marked in blue. PS can be classified by the tacticity regarding the cyclic phenyl group. Isotactic PS (all phenyl groups located on the same side) and syndiotactic PS (alternating location) are semicrystalline. In atactic PS, the phenyl group is located randomly which leads to a purely amorphous polymer. The maximum water uptake of PS is $0.1\text{wt.}\%$ (Domininghaus et al., 2012). In Tab. 2.1, selected thermomechanical properties of PA6 and PS are listed.

	PA6	PS
ϱ in $\mathrm{g/cm^3}$	1.13	1.05
E in GPa	1.4	3.3
α in $\mathrm{K^{-1}}$	$8 \cdot 10^{-5}$	$7 \cdot 10^{-5}$
c_p in $\mathrm{kJ/(kgK)}$	1.8	1.3
κ in $\mathrm{W/(mK)}$	0.29	0.18
θ_g in °C	60 (dry)	100

Table 2.1: Selected thermomechanical properties of PA6 and PS under standard conditions according to Domininghaus et al. (2012): Mass density ϱ, Young's modulus E, thermal expansion coefficient α, specific heat capacity c_p, thermal conductivity κ, glass transition temperature θ_g.

2.1.3 Glass transition

The glass transition is a central phenomenon when considering the thermomechanical properties of polymers. Generally speaking, the glass transition is a transition from a brittle *glassy state* to a softer *rubbery state* (Stommel et al., 2018). Regarding the thermomechanical behaviour, the following observations can be made.

- The stiffness decreases siginficantly (Kehrer et al., 2023).
- During the glass transition, pronounced viscoelastic effects are observed (Kehrer et al., 2023).
- The thermal expansion coefficient increaes (Simon et al., 2001).
- The heat capacity increases, whilst the slope regarding the temperature-dependency of the heat capacity decreases (Androsch et al., 2014).
- During cooling, enthalpy and specific volume decrease montonically. In contrast, the behavior during heating is non-monotonic. This effect is referred to as volume and enthalpy relaxation (Mittermeier, 2017).
- For faster processes, e.g., higher load frequencies or rates, the glass transition is shifted to higher temperatures (Tropin et al., 2015).

Although the glass transition is observed in a temperature interval, a glass transition temperature is defined. It is the temperature, where the

physical properties change the most (Ehrenstein, 2011). The glass transition is observed for amorphous materials. In semicrystalline polymers, this means that the glass transition is only related to the amorphous phase (Ehrenstein, 2011). However, below the glass transition temperature, no crystallization is observed (Janeschitz-Kriegl, 2018). According to Gedde (1999), there are three theories for the glass transition. In the *kinetic theory*, the glass transition is seen as purely kinetic phenomenon, cf., e.g., Kovacs et al. (1979). The glass transition is observed when the time-scale of the experiment is smaller than the time-scale in which the polymer reaches its equilibrium. Another theory is the *free volume theory*. The free volume is the volume of the polymer that is not occupied by molecular mass (Brinson and Brinson, 2015). It allows for movements of the polymer chains. If the free volume is too small to allow for movement, the glass transition is reached. The WLF equation (Williams et al., 1955) and the Doolittle equation (Doolittle and Doolittle, 1957) are based on the free volume concept. In the *thermodynamic theory*, according to Gibbs and DiMarzio (1958), it is stated that there is a true thermodynamic transition in the equilibrium properties of the material.

2.1.4 Experimental characterization

Regarding the experimental thermoviscoelastic characterization of thermoplastic polymers, three experimental methods are of special interest: DMA to measure thermoviscoelastic properties, DSC to measure caloric properties, and dilatometry to measure the thermal expansion coefficient. In the following, DMA and DSC are addressed, as experimental input by these methods is used in Ch. 4 and 5.

Dynamic mechanical analysis. For the characterization of thermoviscoelastic properties, DMA is commonly used. A detailed overview on DMA is given, e.g., by Menard (2008). A short summary on the basic concpets of DMA is given here. In DMA testing, four types of experiments

can be considered. In *stress relaxation tests*, a constant strain load is applied and the relaxation behavior of the stress is measured. Vice versa, in *creep tests*, a constant stress load is applied and the creep behavior of the strain is measured. Furthermore, the viscoelastic behavior after unloading can be characterized in creep-recovery tests. *Thermal mechanical analysis* (TMA) is comparable to stress relaxation where, in addition, the temperature is varied. With TMA, the thermal expansion coefficient and the glass transition temperature can be measured. These three types can be seen as static tests as the mechanical load does not change.
In contrast, a sinusoidal load is applied in *dynamic testing*. Depending on the type of the DMA, torsional or axial loadings are considered. Torsional loadings are used for both solids and liquids, axial loadings are only used for solids. By resonance analyzers, a fixed frequency is applied either in a stress-controlled or strain-controlled way. The measurement of the phase shift and the amplitude of the material response allows to compute all viscoelastic properties, cf. Sec. 4.2.3. In frequency scans, the viscoelastic properties are characterized for multiple frequencies. Furthermore, DMA fixtures are always combined with a temperature control which allows to apply temperature scans. The latter can, e g., be used to determine the glass transition temperature. Temperature-frequency sweeps combine frequency and temperature scans.

Differential scanning calorimetry. DSC is an important method for the characterization of caloric properties. A detailed overview is, e.g., given by Höhne et al. (2003). Again, the central concepts are summarized here. Basically, DSC is a method for measuring the heat required for a sample to follow a predefined temperature process. DSC is a differential measuring method as, additionally to the sample to be analyzed, a reference sample with known thermal properties is required.
There are mainly two types of DSC: *heat flux DSC* and *power compensating DSC*. In heat flux DSC, a heat exchange path with known thermal

resistance is given. The temperature difference between sample and reference is measured over time. As the heat flow rate is proportional to the temperature difference, the heat flow rate can be directly derived. In power-compensating DSC, the temperature difference is hold close to zero via a control circuit. The heat flow rate, which is needed for that, is measured over time.
Based on the temperature process that is prescribed via thermal control, there are mainly three modes of operation: *isothermal*, *constant temperature rate* (heating or cooling) and *modulated temperature* (sinusoidal). From the output signal of temperature difference or heat flow rate, caloric properties of the sample can be derived. For example, the temperature-dependent heat capacity can be calculated under constant temperature rates. Note that DSC is applied under isobaric conditions. Thus, only the isobaric heat capacity can be determined. In modulated temperature DSC, the complex heat capacity can be characterized. Furthermore, DSC is used to determine, e.g., enthalpy, entropy, heat of transitions, the glass transition temperature or the degree of crystallinity.

2.2 Continuum thermomechanics

2.2.1 Kinematics

In the following, the fundamentals of continuum mechanics are briefly summarized. For more details, the reader is, e.g., referred to Šilhavý (1997), Haupt (2002) or Liu (2002). By kinematics, a formal framework to describe the motion and deformation of a body Ω is given.

Motion. The equation of motion

$$\boldsymbol{x} = \boldsymbol{\chi}(\boldsymbol{X}, t) \tag{2.1}$$

is introduced (Gurtin et al., 2010). Here, $\boldsymbol{X}$ denotes the reference position of a material point in the initial configuration of Ω. The current position of a material point at time t is then given by $\boldsymbol{x}$. In general, field properties can be parametrized either in the current configuration, *Eulerian description*, or in the reference configuration, *Lagrangian description* (Liu, 2002). In this work, as common in solid mechanics, the Lagrangian description is used meaning that all field properties depend on $\boldsymbol{X}$. Furthermore, the displacement

$$\boldsymbol{u}(\boldsymbol{X}, t) = \boldsymbol{\chi}(\boldsymbol{X}, t) - \boldsymbol{X}, \tag{2.2}$$

the velocity

$$\boldsymbol{v}(\boldsymbol{X}, t) = \dot{\boldsymbol{x}} = \dot{\boldsymbol{u}} = \frac{\partial \boldsymbol{\chi}(\boldsymbol{X}, t)}{\partial t} \tag{2.3}$$

and the acceleration

$$\boldsymbol{a}(\boldsymbol{X}, t) = \ddot{\boldsymbol{x}} = \ddot{\boldsymbol{u}} = \frac{\partial^2 \boldsymbol{\chi}(\boldsymbol{X}, t)}{\partial t^2} \tag{2.4}$$

are defined (Liu, 2002).

Deformation. Next, deformation is considered. Therefore, the deformation gradient

$$\boldsymbol{F} = \frac{\partial \boldsymbol{x}}{\partial \boldsymbol{X}} \tag{2.5}$$

is defined (Haupt, 2002). With Eq. (2.2), the displacement gradient is given by

$$\boldsymbol{H} = \frac{\partial \boldsymbol{u}}{\partial \boldsymbol{X}} = \boldsymbol{F} - \boldsymbol{I}. \tag{2.6}$$

If $||\boldsymbol{H}|| \ll 1$ holds, the deformation can be considered small (Haupt, 2002). If, additionally, the displacement is small, the following approximations can be used (Haupt, 2002)

$$\boldsymbol{x} \approx \boldsymbol{X}, \quad \frac{\partial(\cdot)}{\partial \boldsymbol{x}} \approx \frac{\partial(\cdot)}{\partial \boldsymbol{X}}. \tag{2.7}$$

In words, the Eulerian and the Lagrangian description coincide. Furthermore, under these assumptions, all strain tensors are equivalent, given by the symmetric part of $\boldsymbol{H}$, the infinitesimal strain tensor

$$\boldsymbol{\varepsilon} = \frac{1}{2}\left(\boldsymbol{H} + \boldsymbol{H}^{\mathsf{T}}\right). \tag{2.8}$$

The infinitesimal strain tensor can be decomposed into a spherical part $\boldsymbol{\varepsilon}^{\circ}$ and a deviatoric part $\boldsymbol{\varepsilon}'$ by

$$\boldsymbol{\varepsilon} = \boldsymbol{\varepsilon}^{\circ} + \boldsymbol{\varepsilon}', \tag{2.9}$$

$$\boldsymbol{\varepsilon}^{\circ} = \frac{1}{3}\mathrm{tr}(\boldsymbol{\varepsilon})\boldsymbol{I} = \frac{1}{3}\varepsilon^{\mathrm{vol}}\boldsymbol{I}, \tag{2.10}$$

$$\boldsymbol{\varepsilon}' = \boldsymbol{\varepsilon} - \boldsymbol{\varepsilon}^{\circ} \tag{2.11}$$

(Liu, 2002). In case of small deformations, the volumetric strain $\varepsilon^{\mathrm{vol}}$ expresses the relative change in specific volume by

$$\varepsilon^{\mathrm{vol}} = \frac{v - v_0}{v_0} = \varrho_0 v - 1 = \frac{\varrho_0 - \varrho}{\varrho} \tag{2.12}$$

(Liu, 2002). Here, v_0 and ϱ_0 denote the specific volume and the mass density in the initial state respectively. The velocity gradient and its symmetric part are given by

$$\boldsymbol{L} = \frac{\partial \boldsymbol{v}}{\partial \boldsymbol{x}} \approx \dot{\boldsymbol{H}}, \quad \boldsymbol{D} = \frac{1}{2}\left(\boldsymbol{L} + \boldsymbol{L}^{\mathsf{T}}\right) \approx \dot{\boldsymbol{\varepsilon}} \tag{2.13}$$

(Gurtin et al., 2010). Under small deformations and small displacements, $\boldsymbol{D}$ can be approximated by the strain rate tensor.

Temperature. In thermomechanical coupled problems, the temperature θ is an additional base field. The temperature gradient is given by (Haupt, 2002)

$$\boldsymbol{g} = \frac{\partial \theta}{\partial \boldsymbol{X}} \approx \frac{\partial \theta}{\partial \boldsymbol{x}}. \tag{2.14}$$

2.2.2 Balance equations

In thermomechanics, the balance equations define fundamental laws that must be fullfilled by all thermomechanical processes on the material volume Ω. The general balance equation is given by

$$\frac{\mathrm{d}}{\mathrm{d}t}\int_{\Omega}\Psi\,\mathrm{d}V=\int_{\Omega}\left(p_{\Psi}+s_{\Psi}\right)\mathrm{d}V+\int_{\partial\Omega}\boldsymbol{q}_{\Psi}\cdot\,\mathrm{d}\boldsymbol{A} \tag{2.15}$$

(Liu, 2002). The volumetric density of the balanced field property is denoted by Ψ. A change of the property can be caused by production p_{Ψ} by supply s_{Ψ} and by flux through the surface $\boldsymbol{q}_{\Psi}$. For this general balance equation, small deformations and small displacements are assumed. By additionally assuming continuous fields and by applying the Reynolds transport theorem and the divergence theorem, Eq. (2.15) is reformulated to

$$\int_{\Omega}\left(\frac{\partial\Psi}{\partial t}+\operatorname{div}\left(\Psi\boldsymbol{v}\right)\right)\,\mathrm{d}V=\int_{\Omega}\left(p_{\Psi}+s_{\Psi}+\operatorname{div}\left(\boldsymbol{q}_{\Psi}\right)\right)\,\mathrm{d}V \tag{2.16}$$

(Liu, 2002). Then, by considering an infinitesimal volume element, the local balance equation can be derived (Liu, 2002), giving

$$\frac{\partial\Psi}{\partial t}+\operatorname{div}\left(\Psi\boldsymbol{v}\right)=p_{\Psi}+s_{\Psi}+\operatorname{div}\left(\boldsymbol{q}_{\Psi}\right). \tag{2.17}$$

In the following, the specific balance equations for thermomechanical systems are summarized.

Balance of mass. The volume density Ψ is specified by the mass density ϱ. Production and supply vanish (Haupt, 2002). If no diffusion processes are considered, the flux also vanishes. This gives

$$\frac{\partial\varrho}{\partial t}+\operatorname{div}\left(\varrho\boldsymbol{v}\right)=0. \tag{2.18}$$

Balance of linear momentum. The considered volume density is specified by $\varrho \boldsymbol{v}$. In the balance of linear momentum, the supply is given by the volume force density $\varrho \boldsymbol{b}$, the production vanishes and the flux is given by the Cauchy stress tensor $\boldsymbol{\sigma}$ (Haupt, 2002). Then, by using the balance of mass, Eq. (2.18), the balance of linear momentum reads

$$\varrho \dot{\boldsymbol{v}} = \varrho \ddot{\boldsymbol{u}} = \varrho \boldsymbol{b} + \operatorname{div}(\boldsymbol{\sigma}) . \tag{2.19}$$

Balance of angular momentum. For the balance of angular momentum, a *Boltzmann continuum* is considered, meaning that there are no rotational degrees of freedom, i.e., no spin. By neglecting moment densities, the balance of angular momentum simplifies to an algebraic equation, the symmetry of the Cauchy stress (Liu, 2002)

$$\boldsymbol{\sigma} = \boldsymbol{\sigma}^{\mathsf{T}}. \tag{2.20}$$

Balance of energy. The volume density is given by the total energy which is the sum of the internal energy ϱe and the kinetic energy $\varrho \boldsymbol{v} \cdot \boldsymbol{v}/2$. The supply is specified by the heat sources ϱw and the power of the volume force density $\varrho \boldsymbol{b} \cdot \boldsymbol{v}$. The flux is the sum of the heat flux vector $\boldsymbol{q}$ and the power of the surface forces $\boldsymbol{\sigma}^{\mathsf{T}} \boldsymbol{v}$. As there is no production term, the balance of energy reads

$$\varrho \dot{e} + \frac{1}{2} \varrho \boldsymbol{v} \cdot \boldsymbol{v} = \varrho w + \varrho \boldsymbol{b} \cdot \boldsymbol{v} - \operatorname{div}(\boldsymbol{q}) + \operatorname{div}\left(\boldsymbol{\sigma}^{\mathsf{T}} \boldsymbol{v}\right) \tag{2.21}$$

(Haupt, 2002). Under the assumption of a small velocity, $\boldsymbol{v} \approx \boldsymbol{0}$, the balance of energy simplifies to the balance of internal energy (Liu, 2002),

$$\varrho \dot{e} = \varrho w - \operatorname{div}(\boldsymbol{q}) + \boldsymbol{\sigma} \cdot \dot{\boldsymbol{\varepsilon}}, \tag{2.22}$$

where, additionally, the approximation $\operatorname{div}\left(\boldsymbol{\sigma}^{\mathsf{T}} \boldsymbol{v}\right) \approx \boldsymbol{\sigma} \cdot \dot{\boldsymbol{\varepsilon}}$ was used.

Balance of entropy. The volume density is specified by the specific entropy s. The supply and the flux are assumed to be given by w/θ and $\boldsymbol{q}/\theta$ respcetively. Furthermore, the entropy production is ϱp_s. The balance of entropy reads

$$\varrho \dot{s} = \varrho \frac{w}{\theta} - \operatorname{div}\left(\frac{\boldsymbol{q}}{\theta}\right) + \varrho p_s \tag{2.23}$$

(Gurtin et al., 2010). By the second law of thermodynamics, the entropy production must be non-negative. Furthermore, the heat source w can be eliminated by using Eq. (2.22) and the internal energy can be replaced by the free Energy ψ via the Legendre-Transformation $e = \psi + s\theta$. This gives the *Clausius-Duhem inequality* (Gurtin et al., 2010)

$$\frac{1}{\varrho}\boldsymbol{\sigma} \cdot \dot{\boldsymbol{\varepsilon}} - \dot{\psi} - s\dot{\theta} - \frac{1}{\varrho\theta}\boldsymbol{q} \cdot \boldsymbol{g} \geq 0. \tag{2.24}$$

2.2.3 Constitutive modeling

In continuum thermomechanics of solids, basically, the displacement field $\boldsymbol{u}$ and the temperature field θ are of interest. Therefore, the balance of linear momentun, Eq. (2.19), and the balance of internal energy, Eq. (2.22), should be solved. In general, this system of partial differential equations is underconstrained as the stress $\boldsymbol{\sigma}$, the heat flux $\boldsymbol{q}$, and the internal energy e are unknown. Furthermore, a set of internal variables $\underline{z}$ could be needed to account for the configuration of the material on the microscopic level. The basic fields are then given by

$$\mathcal{B} = \{\boldsymbol{u}, \theta, \underline{z}\} \tag{2.25}$$

(Liu, 2002). The set of unknowns that will be modeled by material specific constitutive theory is

$$\mathcal{K} = \{\boldsymbol{\sigma}, \boldsymbol{q}, \psi, s, \underline{f}\}. \tag{2.26}$$

The entropy is added to the set as the Clausius-Duhem inequality, Eq. (2.24), is considered to ensure thermodynamical consistency of the constitutive models. The evolution on the internal variables is defined by $\dot{\underline{z}} = \underline{f}(\cdot)$, a discussion on that is given in Sec. 2.2.4. Furthermore, instead of the internal energy e, the free energy ψ is considered. In general, the constitutive equations are given by

$$\mathcal{K} = \mathcal{M}(\mathcal{E}(\mathcal{B})), \tag{2.27}$$

where $\mathcal{E}$ is the set of input parameters. This set is defined to be

$$\mathcal{E}(\mathcal{B}) = \{\boldsymbol{\varepsilon}, \dot{\boldsymbol{\varepsilon}}, \theta, \dot{\theta}, \boldsymbol{g}, \underline{z}\}, \tag{2.28}$$

where only parameters that satisfy the principle of material objectivity are used (Liu, 2002). Furthermore, a decomposition of the stress is introduced via

$$\begin{aligned} \boldsymbol{\sigma}(\boldsymbol{\varepsilon}, \dot{\boldsymbol{\varepsilon}}, \theta, \dot{\theta}, \boldsymbol{g}, \underline{z}) &= \widehat{\boldsymbol{\sigma}}(\boldsymbol{\varepsilon}, \theta, \underline{z}) + \breve{\boldsymbol{\sigma}}(\boldsymbol{\varepsilon}, \dot{\boldsymbol{\varepsilon}}, \theta, \dot{\theta}, \boldsymbol{g}, \underline{z}), \\ \widehat{\boldsymbol{\sigma}}(\boldsymbol{\varepsilon}, \theta, \underline{z}) &= \boldsymbol{\sigma}(\boldsymbol{\varepsilon}, \dot{\boldsymbol{\varepsilon}} = \mathbf{0}, \theta, \dot{\theta} = 0, \boldsymbol{g} = \mathbf{0}, \underline{z}) \end{aligned} \tag{2.29}$$

(Šilhavý, 1997). The energetic part of the stress is denoted by $\widehat{\boldsymbol{\sigma}}$, whilst $\breve{\boldsymbol{\sigma}}$ is the non-energetic part. Analogously, a decomposition of the entropy is introduced, giving

$$\begin{aligned} s(\boldsymbol{\varepsilon}, \dot{\boldsymbol{\varepsilon}}, \theta, \dot{\theta}, \boldsymbol{g}, \underline{z}) &= \widehat{s}(\boldsymbol{\varepsilon}, \theta, \underline{z}) + \breve{s}(\boldsymbol{\varepsilon}, \dot{\boldsymbol{\varepsilon}}, \theta, \dot{\theta}, \boldsymbol{g}, \underline{z}), \\ \widehat{s}(\boldsymbol{\varepsilon}, \theta, \underline{z}) &= s(\boldsymbol{\varepsilon}, \dot{\boldsymbol{\varepsilon}} = \mathbf{0}, \theta, \dot{\theta} = 0, \boldsymbol{g} = \mathbf{0}, \underline{z}). \end{aligned} \tag{2.30}$$

Next, the Clausius-Duhem inequality is evaluated based on the *Coleman-Noll procedure* (Coleman and Noll, 1963). By applying the differential of the free energy $\psi(\boldsymbol{\varepsilon}, \dot{\boldsymbol{\varepsilon}}, \theta, \dot{\theta}, \boldsymbol{g}, \underline{z})$ and using Eq. (2.29) and (2.30), the dissipation

inequality is

$$\left(\frac{\widehat{\boldsymbol{\sigma}}}{\varrho} - \frac{\partial\psi}{\partial\boldsymbol{\varepsilon}}\right)\cdot\dot{\boldsymbol{\varepsilon}} - \left(\widehat{s} + \frac{\partial\psi}{\partial\theta}\right)\dot{\theta} + \breve{\boldsymbol{\sigma}}\cdot\dot{\boldsymbol{\varepsilon}} - \breve{s}\dot{\theta} \\ -\frac{\partial\psi}{\partial\dot{\boldsymbol{\varepsilon}}}\cdot\ddot{\boldsymbol{\varepsilon}} - \frac{\partial\psi}{\partial\dot{\theta}}\ddot{\theta} - \frac{\partial\psi}{\partial\boldsymbol{g}}\cdot\dot{\boldsymbol{g}} - \frac{\partial\psi}{\partial\underline{z}}\cdot\dot{\underline{z}} - \frac{\boldsymbol{q}\cdot\boldsymbol{g}}{\varrho\theta} \geq 0. \tag{2.31}$$

The inequality must be satisfied for all thermodynamic processes. By considering only reversible processes, potential relations for the free energy can be derived,

$$\widehat{\boldsymbol{\sigma}} = \varrho\frac{\partial\psi}{\partial\boldsymbol{\varepsilon}}, \quad \widehat{s} = -\frac{\partial\psi}{\partial\theta}. \tag{2.32}$$

Furthermore, by assuming that

$$\frac{\partial\psi}{\partial\dot{\boldsymbol{\varepsilon}}} = \mathbf{0}, \quad \frac{\partial\psi}{\partial\dot{\theta}} = 0, \quad \frac{\partial\psi}{\partial\boldsymbol{g}} = \mathbf{0}, \quad -\frac{\partial\psi}{\partial\underline{z}} = \underline{y} \tag{2.33}$$

holds for all thermodynamic processes, it is concluded that the free energy is given by $\psi = \psi(\boldsymbol{\varepsilon}, \theta, \underline{z})$. The dissipation inequality is then reduced to

$$\breve{\boldsymbol{\sigma}}\cdot\dot{\boldsymbol{\varepsilon}} - \breve{s}\dot{\theta} + \underline{y}\cdot\dot{\underline{z}} - \frac{\boldsymbol{q}\cdot\boldsymbol{g}}{\varrho\theta} \geq 0. \tag{2.34}$$

With the non-energetic stress $\breve{\boldsymbol{\sigma}}$, the non-energetic entropy $\breve{s}$, the thermodynamic driving force $\underline{y}$ and the heat flux $\boldsymbol{q}$, dissipative processes can be modeled. In fluid mechanics, e.g., the non-energetic stress is often modeled by the law for Newtonian fluids,

$$\breve{\boldsymbol{\sigma}} = \mathbb{V}[\dot{\boldsymbol{\varepsilon}}], \tag{2.35}$$

where $\mathbb{V}$ denotes the viscosity tensor (Šilhavý, 1997). If the viscosity tensor is semi-positive definite, the dissipation $\breve{\boldsymbol{\sigma}}\cdot\dot{\boldsymbol{\varepsilon}}$ is non-negative. The heat

flux vector can be modeled, e.g., by Fourier's law of heat conduction

$$\boldsymbol{q} = -\boldsymbol{\kappa}\boldsymbol{g}, \tag{2.36}$$

where $\boldsymbol{\kappa}$ denotes the tensor of heat conduction coefficients (Šilhavý, 1997). If $\boldsymbol{\kappa}$ is semi-positive definite, the dissipation $\boldsymbol{q} \cdot \boldsymbol{g}/(\varrho\theta)$ is non-negative. The modeling of the evolution of the internal variables is discussed in the following subsection.

2.2.4 Evolution of internal variables

In general, the displacement and the temperature field can be determined by solving the balance of linear momentum and the balance of internal energy. In some cases, additional internal variables are necessary to describe the material behavior. As some examples, plastic strains (Gurtin et al., 2010), viscous strains (Haupt, 2002) or crystallinity (Lion and Johlitz, 2016) can be mentioned. Then, evolution equations are needed to solve thermomechanical problems. In this work, the focus is on evolution equations in the form of ordinary differential equations (ODEs). To ensure thermodynamical consistency, the dissipation $\underline{y} \cdot \dot{\underline{z}}$ must be non-negative, see Eq. (2.34). In general, the evolution equation is given by an first order ODE, reading

$$\dot{\underline{z}} = \underline{f}(\boldsymbol{\varepsilon}, \dot{\boldsymbol{\varepsilon}}, \theta, \dot{\theta}, \boldsymbol{g}, \underline{z}). \tag{2.37}$$

In the follwing, three types of evolution equations are discussed.

Potential type. The thermodynamic driving force $\underline{y} = -\partial\psi/\partial\underline{z}$ is derived from the free energy. It is assumed that the rate of the internal variables is a function of the driving force and defined as the derivative of a dissipation potential Φ with respct to the driving force,

$$\dot{\underline{z}} = \underline{f}(\mathcal{E}, \underline{y}) = \frac{\partial\Phi(\mathcal{E}, \underline{y})}{\partial\underline{y}}. \tag{2.38}$$

If the dissipation potential is non-negative and convex for all $\mathcal{E}$ and, if $\Phi(\mathcal{E}, \underline{y} = \underline{0}) = 0$ holds, the dissipation itself is non-negative. Furthermore, for vanishing driving force, the dissipation potential has a global minimum and, thus, the internal variable does not change. Materials that are given by a specific free free energy and a dissipation potential are known as *generalized standard materials* (Halphen and Nguyen, 1975).

Linear irreversible thermodynmics. A straightforward way to ensure thermodynmical consistency is to define $\underline{f}$ as a linear function of the driving force,

$$\dot{\underline{z}} = \underline{\underline{A}}(\mathcal{E})\underline{y} \tag{2.39}$$

(Šilhavý, 1997). Then, the dissipation is given by

$$\underline{y} \cdot \dot{\underline{z}} = \underline{y} \cdot \underline{\underline{A}}(\mathcal{E})\underline{y}. \tag{2.40}$$

If $\underline{\underline{A}}$ is semi-positive definit for all $\mathcal{E}$, thermodynamical consistency is ensured. Furthermore, a dissipation potential can be derived. As a side note, the model of a Newtonian fluid in Eq. (2.35) and Fourier's law in Eq. (2.36) also follow the scheme of linear irreversible thermodynamics.

Relaxation type. In some cases, the evolution equation of an internal variable can be reformulated into an evolution equation (relaxation equation) of the corresponding driving force. This relaxation equation looks like

$$\underline{y} + \tau(\mathcal{E})\dot{\underline{y}} = \underline{F}(\mathcal{E}) \tag{2.41}$$

(Šilhavý, 1997). If the strain rate and the temperature rate are vanishing, the driving force relaxes to a constant value. For a positive relaxation time τ and a linear function $\underline{F}$, the dissipation is positive. The relaxation type of evolution equations is given, e.g., in viscoelasticity. A more specific discussion on that is given in Ch. 3.

2.2.5 Thermodynamic potentials for volumetric deformations

In the previous subsections, the free energy ψ was chosen as the basic potential to describe equilibrium behavior. However, in some cases other potentials could be more suitable. This is addressed here. For simplification, internal variables are neglected and only volumetric processes are considered, meaning that the stress is $\boldsymbol{\sigma} = -p\boldsymbol{I}$ and the strain is $\varepsilon^{\mathrm{vol}}/3\boldsymbol{I}$. The pressure is denoted by p. The volumetric strain $\varepsilon^{\mathrm{vol}}$ can be replaced by the specific volume, see Eq. (2.12). The balance of internal energy and the Clausius-Duhem inequality simplify to

$$\varrho\dot{e} = \varrho w - \operatorname{div}(\boldsymbol{q}) - \underbrace{p\dot{\varepsilon}^{\mathrm{vol}}}_{=p\dot{v}/\varrho_0}, \tag{2.42}$$

$$-\frac{1}{\varrho}p\dot{\varepsilon}^{\mathrm{vol}} - \dot{\psi} - s\dot{\theta} - \frac{1}{\varrho\theta}\boldsymbol{q}\cdot\boldsymbol{g} \geq 0. \tag{2.43}$$

State variables. In thermodynamics, the equilibrium state of a system is completely described by a thermodynamic potential. A thermodynamic potential depends on independent state variables. The dependent state variables are then given by the derivatives of the potential with respect to the independent state variables (Müller, 2001). If no mixture is considered, the state variables are given by temperature θ, pressure p, specific entropy s and specific volume v.[1] Only two of these state variables are independent. In the context of Sec. 2.2.3, the independent variables are basic fields and the dependent state variables are constitutive properties. Which state variables are the independent ones depends on the boundary conditions of the system. The set of independent (natural) state variables of a system then defines the natural potential of a system.

[1] In case of an integral formulation, entropy and volume are used. Both are extensive properties, whilst temperature and pressure are intensive properties. In a local formulation, all state variables are intensive properties.

With that, four thermodynamic potentials arise: specific free energy ψ, specific free enthalpy g, specific internal energy e and specific enthalpy h. The transformations between the potentials are given by Legendre transformations (Müller, 2001). In the following, the free energy and the free enthalpy are discussed in detail as the temperature is one of their natural state variables. In contrast, for internal energy and enthalpy, the specific entropy is a natural state variable which is unusual in continuum thermomechanics.

Free energy. The natural state variables of the free energy (or Helmholtz energy) are the specific volume and temperature. By applying the Coleman-Noll procedure, see. Sec 2.2.3, to Eq. (2.43), potential relations for pressure and specific entropy can be derived,

$$p = -\frac{\partial \psi}{\partial v} = -\varrho \frac{\partial \psi}{\partial \varepsilon^{\mathrm{vol}}}, \quad s = -\frac{\partial \psi}{\partial \theta}. \tag{2.44}$$

Via Legendre transformation, the other potentials can be calculated by

$$\begin{aligned} e = \psi + s\theta = -\theta^2 \frac{\partial(\psi/\theta)}{\partial \theta}, \quad g = \psi + pv = -v^2 \frac{\partial(\psi/v)}{\partial v}, \\ h = \psi + s\theta + pv. \end{aligned} \tag{2.45}$$

For a general deformation state, the strain $\boldsymbol{\varepsilon}$ is analogue to the specific volume. Therefore, in case of strain-driven processes, the free energy is the natural arising potential.

Free enthalpy. The natural state variables of the free enthalpy (or Gibbs energy) are pressure and temperature. The potential relations for specific volume and specific entropy are

$$v = \frac{\partial g}{\partial p} = \frac{1}{\varrho}(1 + \varepsilon^{\mathrm{vol}}), \quad s = -\frac{\partial g}{\partial \theta}, \tag{2.46}$$

whilst the Legendre transformations read

$$h = g + s\theta = -\theta^2 \frac{\partial(g/\theta)}{\partial\theta}, \quad \psi = g - pv = -p^2 \frac{\partial(g/p)}{\partial p},$$
$$e = g + s\theta - pv. \tag{2.47}$$

The general stress state $\boldsymbol{\sigma}$ is analogue to the pressure. Thus, for stress-driven processes, the free enthalpy is the natural arising potential.

Chapter 3

Constitutive theory of thermoviscoelasticity

3.1 Introduction

In Sec. 2.2.3 - 2.2.5, the general constitutive equations of small-strain thermomechanics are summarized. These equations must be further specified based on the physical behavior of the considered material. To model the thermomechanical behavior of thermoplastic polymers, in this work, the characteristics listed in Sec. 2.1.3 are taken into account. This includes viscoelasticity and process-dependent behavior regarding thermal expansion and caloric behavior in the glass transition regime. These properties are mainly driven by relaxation processes that can be modeled via internal variables. Thus, the relaxation processes are considered within the energetic part of the material response. Non-energetic parts of stress and entropy are neglected, which gives $\widehat{\boldsymbol{\sigma}} = \boldsymbol{\sigma}$ and $\widehat{s} = s$. To account for the glass transition, a temperature-dependency of the relaxation processes is considered. The theory of thermoviscoelasticity that is discussed in the following is restricted to linear irreversible thermodynamics. First order models of thermoviscoelasticity are presented in Sec. 3.2. For clarity, purely volumetric deformations are considered. A generalization of the first-order models, that accounts for multiple relaxation processes, is addressed in Sec. 3.3. Last, the basic equations of three-dimensional viscoelasicity are summarized in Sec. 3.4.

3.2 Volumetric first order models

3.2.1 Additive decomposition of free energy

As the consideration in this section is restricted to purely volumetric deformations, a scalar model is derived. Furthermore, the volumetric strains are considered to be small which means that a constant mass density $\varrho = \varrho_0$ can be assumed. The model consists of two parts. The thermomechanical part describes viscoelasticity and thermal expansion, whilst the other part describes purely caloric behavior. For each part, an internal variable is introduced. These are the viscous strain $\varepsilon_{\mathrm{v}}^{\mathrm{vol}}$ for the mechanical part and the internal temperature θ_{v} for the caloric part. By assuming that both parts are uncoupled, an additive decomposition of the free energy follows,

$$\psi(\varepsilon^{\mathrm{vol}}, \varepsilon_{\mathrm{v}}^{\mathrm{vol}}, \theta, \theta_{\mathrm{v}}) = \psi_{\mathrm{m}}(\varepsilon^{\mathrm{vol}}, \varepsilon_{\mathrm{v}}^{\mathrm{vol}}, \theta) + \psi_{\mathrm{c}}(\theta, \theta_{\mathrm{v}}). \tag{3.1}$$

Mechanical part. To model viscoelasticity, a three-parameter model is applied and expanded by thermal expansion coefficients, see Fig. 3.1. This model consists of a linear elastic spring in parallel connection with a linear viscoelastic Maxwell element. The latter is a series connection of a linear elastic spring and linear viscous dashpot. In addition, thermal expansion elements are connected to the springs. Due to the restriction on volumetric deformations, the stiffnesses of the springs are given by the bulk moduli K_0 and K_1, and the viscosity of the dashpot is given by the volume viscosity $\eta_{\mathrm{v}1}$. The thermal expansion elements cause volumetric thermal strains, $\varepsilon_{\theta i} = 3\alpha_i \Delta\theta$, where $\Delta\theta = \theta - \theta_0$ is the temperature difference regarding the reference temperature θ_0.[1] The mechanical part of the free energy ψ_{m} is given by adding the stored energies due to elastic strains within the

[1] The factor 3 stems from the fact that the thermal strain tensor is defined as $\alpha\Delta\theta\boldsymbol{I}$, whilst the spherical part of the strain tensor is defined as $\varepsilon^{\mathrm{vol}}\boldsymbol{I}/3$.

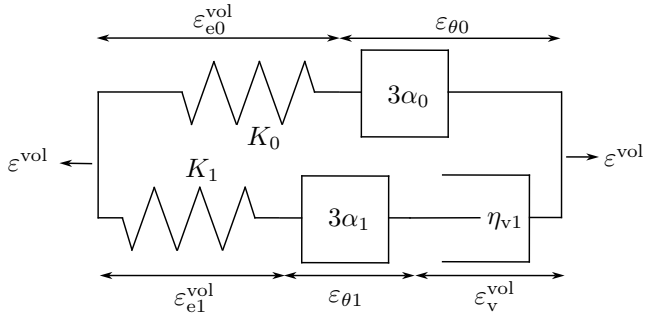

Figure 3.1: Generalized Maxwell model of first order including thermal expansion. The stiffnesses of the springs are denoted by K_0 and K_1, the thermal expansion coefficients by α_0 and α_1 and the volume viscosity by η_{v1}.

springs,

$$\psi_{\mathrm{m}}(\varepsilon^{\mathrm{vol}}, \varepsilon_{\mathrm{v}}^{\mathrm{vol}}, \theta) = \underbrace{\frac{K_0}{2\varrho_0}\left(\varepsilon^{\mathrm{vol}} - 3\alpha_0\Delta\theta\right)^2}_{\psi_{\mathrm{me}}(\varepsilon^{\mathrm{vol}},\theta)} + \underbrace{\frac{K_1}{2\varrho_0}\left(\varepsilon^{\mathrm{vol}} - \varepsilon_{\mathrm{v}}^{\mathrm{vol}} - 3\alpha_1\Delta\theta\right)^2}_{\psi_{\mathrm{mv}}(\varepsilon^{\mathrm{vol}} - \varepsilon_{\mathrm{v}}^{\mathrm{vol}},\theta)}. \tag{3.2}$$

By using the additive decomposition of the strain in series connections, the respective elastic strains are calculated. The equilibrium (elastic) part of the free energy is denoted by ψ_{me}, the non-equilibrium (viscoelastic) part by ψ_{mv}. By the mechanical part of the free energy and the potential relation from Eq. (2.44), a decomposition of the pressure into an elastic pressure p_{e} and a viscoelastic pressure p_{v} follows,

$$p = -\varrho_0 \frac{\partial \psi}{\partial \varepsilon^{\mathrm{vol}}} = -\varrho_0 \frac{\partial \psi_{\mathrm{me}}}{\partial \varepsilon^{\mathrm{vol}}} - \varrho_0 \frac{\partial \psi_{\mathrm{mv}}}{\partial \varepsilon^{\mathrm{vol}}} \tag{3.3}$$

$$= \underbrace{-K_0\left(\varepsilon^{\mathrm{vol}} - 3\alpha_0\Delta\theta\right)}_{p_{\mathrm{e}}} \underbrace{-K_1\left(\varepsilon^{\mathrm{vol}} - \varepsilon_{\mathrm{v}}^{\mathrm{vol}} - 3\alpha_1\Delta\theta\right)}_{p_{\mathrm{v}}}. \tag{3.4}$$

Caloric part. By analogy with the mechanical part of the free energy, the caloric part of the free energy is also decomposed into an equilibrium part

and a non-equilibrium part,

$$\psi_{\mathrm{c}}(\theta,\theta_{\mathrm{v}}) = \underbrace{\varphi(\theta)}_{\psi_{\mathrm{ce}}(\theta)} + \underbrace{\frac{C}{2}(\theta-\theta_{\mathrm{v}})^2}_{\psi_{\mathrm{cv}}(\theta-\theta_{\mathrm{v}})}. \tag{3.5}$$

The equilibrium part ψ_{ce} can be specified by defining an equilibrium heat capacity

$$c_p^{\mathrm{eq}}(\theta) = -\theta\frac{\partial^2\varphi}{\partial\theta^2} \tag{3.6}$$

and integrating with respect to temperature. For the non-equilibrium part ψ_{cv}, analog to the elastic strain, the difference between pyhsical temperature θ and internal temperature θ_{v} contributes to the free energy. This difference can be seen as a deviation from the equilibrium state. In the following, the caloric non-equilibrium behavior is referred to as *viscocaloric* behavior to account for the analogy to viscoelasticity. The physical meaning of the material parameter C will be discussed in Ch. 5. A further dependency on the volumetric strain, which would be similar to thermal expansion within the mechanical part, is neglected here. By the potential relation in Eq. (2.44), the entropy can be calculated

$$\begin{aligned} s = -\frac{\partial\psi}{\partial\theta} &= -\frac{\partial\psi_{\mathrm{me}}}{\partial\theta} - \frac{\partial\psi_{\mathrm{mv}}}{\partial\theta} - \frac{\partial\psi_{\mathrm{ce}}}{\partial\theta} - \frac{\partial\psi_{\mathrm{cv}}}{\partial\theta} \qquad (3.7)\\ &= \underbrace{\frac{3\alpha_0 K_0}{\varrho_0}(\varepsilon^{\mathrm{vol}} - 3\alpha_0\Delta\theta)}_{s_{\mathrm{me}}} + \underbrace{\frac{3\alpha_1 K_1}{\varrho_0}(\varepsilon^{\mathrm{vol}} - \varepsilon_{\mathrm{v}}^{\mathrm{vol}} - 3\alpha_1\Delta\theta)}_{s_{\mathrm{mv}}}\\ &\quad \underbrace{-\varphi'(\theta)}_{s_{\mathrm{ce}}} \underbrace{-C(\theta-\theta_{\mathrm{v}})}_{s_{\mathrm{cv}}}. \qquad (3.8) \end{aligned}$$

The caloric part of the entropy is also decomposed into an equilibrium part s_{ce} and a non-equilibrium part s_{cv}. Furthermore, due to thermal expansion, there is a mechanical part of the entropy which is also decomposed into an elastic part and a viscoelastic part.

3.2.2 Evolution equations

Driving force. The thermodynamic driving forces regarding the evolution of the viscous strain and the internal temperature, according to Eq. (2.33), are given by

$$-\frac{\partial \psi}{\partial \varepsilon_{\mathrm{v}}^{\mathrm{vol}}} = -\frac{\partial \psi_{\mathrm{mv}}}{\partial \varepsilon_{\mathrm{v}}^{\mathrm{vol}}} = \frac{K_1}{\varrho_0}\left(\varepsilon^{\mathrm{vol}} - \varepsilon_{\mathrm{v}}^{\mathrm{vol}} - 3\alpha_1 \Delta\theta\right) = -\frac{p_{\mathrm{v}}}{\varrho_0}, \tag{3.9}$$

$$-\frac{\partial \psi}{\partial \theta_{\mathrm{v}}} = -\frac{\partial \psi_{\mathrm{cv}}}{\partial \theta_{\mathrm{v}}} = C(\theta - \theta_{\mathrm{v}}) = -s_{\mathrm{cv}}. \tag{3.10}$$

The driving force of the viscoelasticity is the negative viscoelastic pressure divided by the mass density. For the viscocaloric behavior, the negative of the non-equilibrium entropy s_{cv} is the driving force. Again, the analogy between the mechanical and the caloric behavior is evident. Next, linear irreversible thermodynamics is applied to define the evolution equations, see Sec. 2.2.4.

Viscous strain. The evolution equation for the viscous strain is introduced by

$$\begin{aligned}\dot{\varepsilon}_{\mathrm{v}}^{\mathrm{vol}} &= -A(\theta,\cdot)\frac{\partial \psi}{\partial \varepsilon_{\mathrm{v}}^{\mathrm{vol}}} = -\frac{\varrho_0}{\eta_{\mathrm{v1}}(\theta,\cdot)}\frac{\partial \psi}{\partial \varepsilon_{\mathrm{v}}^{\mathrm{vol}}} \\ &= \underbrace{\frac{K_1}{\eta_{\mathrm{v1}}(\theta,\cdot)}}_{1/\tau_{\mathrm{v1}}(\theta,\cdot)}\left(\varepsilon^{\mathrm{vol}} - \varepsilon_{\mathrm{v}}^{\mathrm{vol}} - 3\alpha_1\Delta\theta\right) = -\frac{p_{\mathrm{v}}}{\eta_{\mathrm{v1}}(\theta,\cdot)},\end{aligned} \tag{3.11}$$

where τ_{v1} is a relaxation time. Due to the pronounced temperature-dependent behavior of viscoelastic materials, the temperature-dependency of the viscosity is explicitly stated. Furthermore, dependencies on strain, strain rate or temperature rate are conceivable. If a dependency on the driving force or the internal variable itself is considered, the evolution equation becomes nonlinear. This case is excluded in this work. To satisfy

the dissipation inequality, the viscosity must be positive.[2] By derivating the additive decomposition of the volumetric strain within the Maxwell element with respect to time,

$$\dot{\varepsilon}^{\mathrm{vol}} = \dot{\varepsilon}_{\mathrm{v}}^{\mathrm{vol}} - \frac{\dot{p}_{\mathrm{v}}}{K_1} + 3\alpha_1 \dot{\theta}, \tag{3.12}$$

the rate of the viscous strain in Eq. (3.11) can be replaced. This finally gives a relaxation equation for the viscoelastic pressure,

$$\tau_{\mathrm{v}1}(\theta, \cdot)\dot{p}_{\mathrm{v}} + p_{\mathrm{v}} = \eta_{\mathrm{v}1}(\theta, \cdot)(3\alpha_1 \dot{\theta} - \dot{\varepsilon}^{\mathrm{vol}}). \tag{3.13}$$

Note that the dependencies of the relaxation time, e.g., temperature-dependency, result from the dependencies of the viscosity. If a constant strain and a constant temperature are applied, the viscoelastic pressure p_{v} relaxes to zero for infinite times. In case of general viscoelasticity, stress relaxation is observed.

Internal temperature. The evolution equation of the internal temperature is given by

$$\begin{aligned} \dot{\theta}_{\mathrm{v}} &= -B(\theta, \cdot)\frac{\partial \psi}{\partial \theta_{\mathrm{v}}} = -\frac{1}{\xi(\theta, \cdot)}\frac{\partial \psi}{\partial \theta_{\mathrm{v}}} \\ &= \underbrace{\frac{C}{\xi(\theta, \cdot)}}_{1/\lambda(\theta, \cdot)}(\theta - \theta_{\mathrm{v}}) = -\frac{s_{\mathrm{cv}}}{\xi(\theta, \cdot)}, \end{aligned} \tag{3.14}$$

where ξ is a caloric viscosity and λ is a relaxation time. The caloric viscosity must be positive to satisfy the dissipation inequality. Similar to the strain, an additive decomposition of the physical temperature can be derived,

$$\theta = \theta_{\mathrm{v}} - \frac{s_{cv}}{C}. \tag{3.15}$$

[2] By convexity of the free energy, the bulk moduli K_0 and K_1 are positive.

Analog to Eq. (3.13), an relaxation equation for the viscocaloric entropy arises,

$$\lambda(\theta,\cdot)\dot{s}_{\mathrm{cv}} + s_{\mathrm{cv}} = -\xi(\theta,\cdot)\dot{\theta}. \tag{3.16}$$

At a constant temperature, s_{cv} relaxes to zero for infinite times. Thus, for viscocaloric behavior, *entropy relaxation* can be observed. In literature, this behavior is known under the term *enthalpy relaxation*. However, as in Eq. (3.10), the (negative) viscocaloric entropy arises as thermodynamic driving force, the term entropy relaxation seems more reasonable and is used in this work.

Dissipation potential. Due to the linearity of the evolution equations with respect to the driving forces, see Eq. (3.11) and (3.14), a dissipation potentials arises by Eq. (2.38)

$$\Phi(-p_{\mathrm{v}}/\varrho_0, -s_{\mathrm{cv}}) = \underbrace{\frac{\varrho_0(-p_{\mathrm{v}}/\varrho_0)^2}{2\eta_{\mathrm{v1}}(\theta,\cdot)}}_{\Phi_{\mathrm{m}}} + \underbrace{\frac{(-s_{\mathrm{cv}})^2}{2\xi(\theta,\cdot)}}_{\Phi_{\mathrm{c}}}. \tag{3.17}$$

The dissipation potential is convex. Additionally, a minimum exists for vanishing driving forces meaning that the internal variables do not change in this case.

3.3 Generalized thermorheological models

3.3.1 Generalized Maxwell model

In Sec. 3.2, a first order model of thermoviscoelasticity was discussed. The model is basically described by a single relaxation time for each of both model parts. This can be inadequate if load cases are considered that cover multiple time decades, e.g., relaxation or creep tests. Then, a distribution of relaxation times is needed. Discretized distributions of

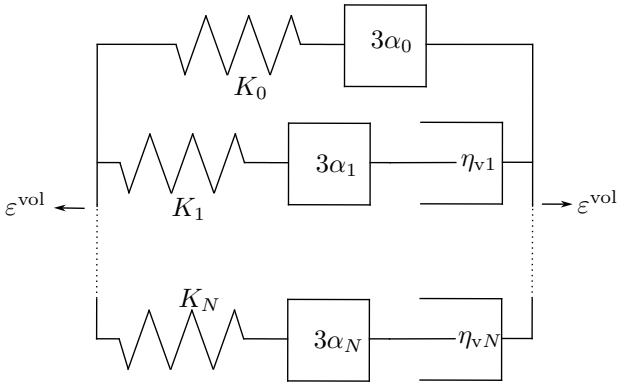

Figure 3.2: Generalized Maxwell model including thermal expansion. The stiffnesses of the springs are denoted by K_i, the thermal expansion coefficients by α_i and the viscosities by $\eta_{\mathrm{v}i}$.

relaxation times are given, e.g., by generalized thermorheological models. These models can be illustrated by connections of thermoelastic springs and viscous dashpots. For strain-driven processes, the GMM is often used, see Fig. 3.2. It is a parallel connection of a thermoelastic spring with N thermoviscoelastic Maxwell elements. The order of the GMM is given by N. In the following, the linear GMM for volumetric deformations is discussed. The free energy results to

$$\begin{aligned}\psi_{\mathrm{m}}(\varepsilon^{\mathrm{vol}}, \varepsilon^{\mathrm{vol}}_{\mathrm{v}1}, \ldots, \varepsilon^{\mathrm{vol}}_{\mathrm{v}N}, \theta) =& \frac{K_0}{2\varrho_0}(\varepsilon^{\mathrm{vol}} - 3\alpha_0\Delta\theta)^2 \\ &+ \sum_{i=1}^{N} \frac{K_i}{2\varrho_0}(\varepsilon^{\mathrm{vol}} - \varepsilon^{\mathrm{vol}}_{\mathrm{v}i} - 3\alpha_i\Delta\theta)^2. \end{aligned} \tag{3.18}$$

In comparison to the first order GMM presented in Sec. 3.2, the equilibrium part is the same, whilst the non-equilibrium part of the free energy consists of N parts. For each of the non-equilibrium parts, a viscous strain is

introduced as internal variable. The resulting pressure, given by

$$\begin{aligned} p &= -\varrho_0 \frac{\partial \psi_{\mathrm{m}}}{\partial \varepsilon^{\mathrm{vol}}} \\ &= \underbrace{-K_0(\varepsilon^{\mathrm{vol}} - 3\alpha_0 \Delta\theta)}_{p_{\mathrm{e}}} + \sum_{i=1}^{N} \underbrace{-K_i(\varepsilon^{\mathrm{vol}} - \varepsilon_{\mathrm{v}i}^{\mathrm{vol}} - 3\alpha_i \Delta\theta)}_{p_{\mathrm{v}i}}, \end{aligned} \tag{3.19}$$

is also decomposed into an elastic part and N viscoelastic parts. As in Eq. (3.11), linear irreversible thermodynamics is applied to derive the evolution equations for the viscous strains $\varepsilon_{\mathrm{v}1}^{\mathrm{vol}}, \ldots, \varepsilon_{\mathrm{v}N}^{\mathrm{vol}}$,

$$\dot{\varepsilon}_{\mathrm{v}i}^{\mathrm{vol}} = -\frac{\varrho_0}{\eta_{\mathrm{v}i}} \frac{\partial \psi_{\mathrm{m}}}{\partial \varepsilon_{\mathrm{v}i}^{\mathrm{vol}}} = \underbrace{\frac{K_i}{\eta_{\mathrm{v}i}}(\varepsilon^{\mathrm{vol}} - \varepsilon_{\mathrm{v}i}^{\mathrm{vol}} - 3\alpha_i \Delta\theta)}_{-p_{\mathrm{v}i}/\eta_{\mathrm{v}i}}, \quad i = 1, \ldots, N. \tag{3.20}$$

The thermodynamic driving force for each viscous strain is the negative viscoelastic pressure of the corresponding Maxwell element divided by the mass density. Temperature-dependencies of the viscosities are not explicitely stated here. This will be addressed in Sec 3.3.5. The relaxation times of the Maxwell elements are given by $\tau_{\mathrm{v}i} = \eta_{\mathrm{v}i}/K_i$. As the evolution equations are decoupled in case of strain-driven processes, the GMM can be seen as the natural model in this case. For stress-driven processes, the volumetric strain in Eq. (3.20) must be replaced via Eq. (3.19) which gives a coupled system of differential equations. For completeness, the dissipation potential is given

$$\Phi_{\mathrm{m}}(-p_{\mathrm{v}1}/\varrho_0, \ldots, -p_{\mathrm{v}N}/\varrho_0) = \sum_{i=1}^{N} \frac{\varrho_0(-p_{\mathrm{v}i}/\varrho_0)^2}{2\eta_{\mathrm{v}i}}. \tag{3.21}$$

The system of first order ODEs in Eq. (3.20) can be reformulated into a single ODE of order N. This gives

$$p + \sum_{k=1}^{N} \frac{a_k}{a_0} \frac{\mathrm{d}^k p}{\mathrm{d}t^k} = -\sum_{k=0}^{N} \frac{b_k}{a_0} \frac{\mathrm{d}^k \varepsilon^{\mathrm{vol}}}{\mathrm{d}t^k} + \frac{3c_0}{a_0} \Delta\theta + \sum_{k=1}^{N} \frac{3c_k}{a_0} \frac{\mathrm{d}^k \theta}{\mathrm{d}t^k}. \tag{3.22}$$

The derivation of the ODE and the definitions of the coefficients are shown in App. A.1.1. By the ODE, it is motivated to refer to a GMM of order N.

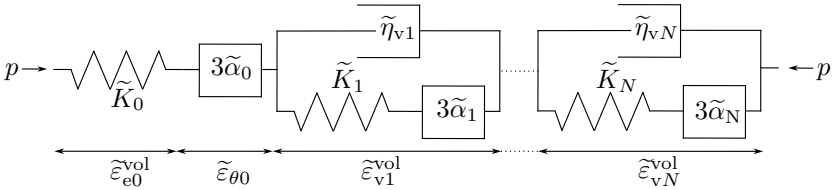

Figure 3.3: Generalized Kelvin model including thermal expansion. The stiffnesses of the springs are denoted by $\widetilde{K}_i$, the thermal expansion coefficients by $\widetilde{\alpha}_i$ and the viscosities of the dashpots by $\widetilde{\eta}_{\mathrm{v}i}$.

3.3.2 Generalized Kelvin model

For stress-driven processes, the GKM is more suitable than the GMM. The GKM is a series connection of a thermoelastic spring with N thermoviscoelastic Kelvin elements, the latter being parallel connections of a spring and a dashpot. As a first step, the free energy is derived by adding the elastic energies of all springs,

$$\begin{aligned}\psi_{\mathrm{m}}(\varepsilon^{\mathrm{vol}}, \widetilde{\varepsilon}^{\mathrm{vol}}_{\mathrm{v}1}, \ldots, \widetilde{\varepsilon}^{\mathrm{vol}}_{\mathrm{v}N}, \theta) = &\frac{p^2(\varepsilon^{\mathrm{vol}}, \widetilde{\varepsilon}^{\mathrm{vol}}_{\mathrm{v}1}, \ldots, \widetilde{\varepsilon}^{\mathrm{vol}}_{\mathrm{v}N}, \theta)}{2\varrho_0 \widetilde{K}_0} \\ &+ \sum_{i=1}^{N} \frac{\widetilde{K}_i}{2\varrho_0} (\widetilde{\varepsilon}^{\mathrm{vol}}_{\mathrm{v}i} - 3\widetilde{\alpha}_i)^2. \end{aligned} \tag{3.23}$$

As pressure-driven processes are considered, a transformation to the free enthalpy is necessary. By Eq. (2.12) and (2.45), the free enthalpy reads

$$\begin{aligned}\widetilde{g}_{\mathrm{m}}(p,\widetilde{\varepsilon}^{\mathrm{vol}}_{\mathrm{v}1},\dots,\widetilde{\varepsilon}^{\mathrm{vol}}_{\mathrm{v}N},\theta) =& \widetilde{\psi}_{\mathrm{m}} + \frac{p}{\varrho_0}(1+\varepsilon^{\mathrm{vol}}) \\ =& -\frac{p^2}{2\varrho_0\widetilde{K}_0} + \frac{p}{\varrho_0}\left(1+3\widetilde{\alpha}_0\Delta\theta\right) \\ &+ \sum_{i=1}^{N}\frac{\widetilde{K}_i}{2\varrho_0}\left(\widetilde{\varepsilon}^{\mathrm{vol}}_{\mathrm{v}i} - 3\widetilde{\alpha}_i\Delta\theta\right)^2 + \frac{p}{\varrho_0}\sum_{i=1}^{N}\widetilde{\varepsilon}^{\mathrm{vol}}_{\mathrm{v}i}. \quad (3.24)\end{aligned}$$

This expression can be decomposed into an elastic part and N viscoelastic parts. The same holds for the volumetric strain, which is now a dependent state variable. Calculation via the potential relation in Eq. (2.46) gives

$$\varepsilon^{\mathrm{vol}} = \varrho_0\frac{\partial\widetilde{g}_{\mathrm{m}}}{\partial p} - 1 = -\frac{p}{\widetilde{K}_0} + 3\widetilde{\alpha}_0\Delta\theta + \sum_{i=1}^{N}\widetilde{\varepsilon}^{\mathrm{vol}}_{\mathrm{v}i}. \quad (3.25)$$

For each Kelvin element, a viscous strain $\widetilde{\varepsilon}^{\mathrm{vol}}_{\mathrm{v}i}$ is introduced as internal variable. Via irreversible thermodynamics, the evolution equations are defined by

$$\dot{\widetilde{\varepsilon}}^{\mathrm{vol}}_{\mathrm{v}i} = -\frac{\varrho_0}{\widetilde{\eta}_{\mathrm{v}i}}\frac{\partial\widetilde{g}_{\mathrm{m}}}{\partial\widetilde{\varepsilon}^{\mathrm{vol}}_{\mathrm{v}i}} = -\frac{1}{\widetilde{\eta}_{\mathrm{v}i}}\underbrace{\left(\widetilde{K}_i(\widetilde{\varepsilon}^{\mathrm{vol}}_{\mathrm{v}i} - 3\widetilde{\alpha}_i\Delta\theta) + p\right)}_{\widetilde{p}_{\mathrm{v}i}}, \quad i=1,\dots,N. \quad (3.26)$$

The thermodynamic driving force in each Kelvin element is the negative viscous pressure divided by the mass density of the corresponding dashpot. The expression $\widetilde{\tau}_{\mathrm{v}i} = \widetilde{\eta}_{\mathrm{v}i}/\widetilde{K}_i$ is called volume retardation time. In contrast to the GMM, the evolution equations of the GKM are decoupled in case of stress-driven processes. Therefore, the GKM is the natural model for stress-driven processes. For completeness, the dissipation potential of the

GKM is given

$$\widetilde{\Phi}_{\mathrm{m}}(-\widetilde{p}_{\mathrm{v}1}/\varrho_0,\ldots,-\widetilde{p}_{\mathrm{v}N}/\varrho_0)=\sum_{i=1}^{N}\frac{\varrho_0(-\widetilde{p}_{\mathrm{v}i}/\varrho_0)^2}{2\widetilde{\eta}_{\mathrm{v}i}}. \tag{3.27}$$

Just as for the GMM, the system of ODEs in Eq. (3.26) can be reformulated into a single ODE of order N,

$$p+\sum_{k=1}^{N}\frac{\widetilde{a}_k}{\widetilde{a}_0}\frac{\mathrm{d}^k p}{\mathrm{d}t^k}=-\sum_{k=0}^{N}\frac{\widetilde{b}_k}{\widetilde{a}_0}\frac{\mathrm{d}^k\varepsilon^{\mathrm{vol}}}{\mathrm{d}t^k}+\frac{3\widetilde{c}_0}{\widetilde{a}_0}\Delta\theta+\sum_{k=1}^{N}\frac{3\widetilde{c}_k}{\widetilde{a}_0}\frac{\mathrm{d}^k\theta}{\mathrm{d}t^k}. \tag{3.28}$$

The derivation and definition of the coefficients is shown in App. A.1.2.

3.3.3 Generalized viscocaloric model

A generalization of the viscocaloric model presented in Sec. 3.2 is also conceivable. In the following, the governing equations of the generalized viscocaloric model are shortly summarized. The free energy is given by

$$\psi_{\mathrm{c}}(\theta,\theta_{\mathrm{v}1},\ldots,\theta_{\mathrm{v}M})=\varphi(\theta)+\sum_{i=1}^{M}\frac{C_i}{2}(\theta-\theta_{\mathrm{v}i})^2. \tag{3.29}$$

Due to the purely caloric behavior, the free energy ψ_{c} is identical to the free enthalpy g_{c}. The resulting entropy is

$$s_{\mathrm{c}}=-\frac{\partial\psi_{\mathrm{c}}}{\partial\theta}=-\varphi'(\theta)+\sum_{i=1}^{M}\underbrace{-C_i(\theta-\theta_{\mathrm{v}i})}_{s_{\mathrm{cv}i}}. \tag{3.30}$$

By linear irreversible thermodynamics, the evolution equations of the internal variables are

$$\dot{\theta}_{\mathrm{v}i}=-\frac{1}{\xi_i}\frac{\partial\psi_{\mathrm{c}}}{\partial\theta_{\mathrm{v}i}}=\underbrace{\frac{C_i}{\xi_i}}_{1/\lambda_i}(\theta-\theta_{\mathrm{v}i}) \tag{3.31}$$

and a dissipation potential arises

$$\Phi_{\mathrm{c}}(-s_{\mathrm{cv}1},\dots,-s_{\mathrm{cv}M}) = \sum_{i=1}^{M} \frac{-s_{\mathrm{cv}i}^2}{2\xi_i}. \tag{3.32}$$

3.3.4 Boltzmann superposition

So far, the thermoviscoelastic models were discussed in their differential formulation. With that, their thermodynamical consistency can be directly seen. However, as the evolution equations are linear and, thus, analytically solvable, integral formulations can be derived. First, a general output function

$$y(t) = kx(t)H(t), \quad H(t) = \begin{cases} 1, & t \geq 0, \\ 0, & t < 0 \end{cases} \tag{3.33}$$

is considered. The load k is applied as a step function and $x(t)$ defines the response function. Due to linearity, a general load can be approximated by superposition of multiple step loads,

$$y(t) = k_0 H(t)x(t) + \sum_{i=1}^{N} (k_i - k_{i-1})H(t-t_i)x(t-t_i). \tag{3.34}$$

Consideration of a limit case gives the integral expression

$$\begin{aligned} y(t) &= k_0 H(t)x(t) + \lim_{\substack{N\to\infty \\ \Delta t\to 0}} \sum_{i=1}^{N} (k_i - k_{i-1})H(t-t_i)x(t-t_i) \\ &= \int_0^t x(t-s)\frac{\mathrm{d}k(s)}{\mathrm{d}s}\,\mathrm{d}s \end{aligned} \tag{3.35}$$

(Brinson and Brinson, 2015). This convolution integral is called *Boltzmann superposition integral* and can be used to derive integral formulations of the

generalized thermorheological models[3]. In general, the lower bound of the integration is set to $s = -\infty$. Here, the loads are assumed to be applied at $t = 0$ or later. Thus, both formulations are equivalent.

GMM. Solving the evolution equations of the GMM in Eq. (3.20) for a constant pressure p and a constant temperature difference $\Delta\theta$ and assuming vanishing initial values gives

$$\varepsilon_{\mathrm{v}i}^{\mathrm{vol}} = (\varepsilon^{\mathrm{vol}} - 3\alpha_i \Delta\theta)\left(1 - \exp\left(-\frac{t}{\tau_{\mathrm{v}i}}\right)\right), \quad i = 1, \ldots, N. \tag{3.36}$$

Inserting these expressions into Eq. (3.19) then leads to

$$\begin{aligned} p(t) = &- \underbrace{\left(K_0 + \sum_{i=1}^{N} K_i \exp\left(-\frac{t}{\tau_{\mathrm{v}i}}\right)\right)}_{K(t)} \varepsilon^{\mathrm{vol}} \\ &+ \underbrace{3\left(\alpha_0 K_0 + \sum_{i=1}^{N} \alpha_i K_i \exp\left(-\frac{t}{\tau_{\mathrm{v}i}}\right)\right)}_{\beta(t)} \Delta\theta. \end{aligned} \tag{3.37}$$

The bulk relaxation modulus is denoted by $K(t)$, whilst $\beta(t)$ is the transient temperature-stress coefficient (Zocher and Groves, 1997). For a GMM, both properties are given by so called *Prony series*. Applying Eq. (3.35), gives the Boltzmann superposition integral of a GMM,

$$p(t) = -\int_0^t K(t-s)\dot{\varepsilon}^{\mathrm{vol}}(s)\,\mathrm{d}s + \int_0^t \beta(t-s)\dot{\theta}(s)\,\mathrm{d}s - \beta(t)\theta_0 H(t). \tag{3.38}$$

GKM. The same procedure is repeated for the GKM. Solving Eq. (3.26) for a constant pressure and a constant temperature, assuming vanishing

[3] If the load $k(t)$ is given by a step function, the function is not continously differentiable at the jump. However, by using the Dirac delta function, the integral can still be solved.

initial values, and inserting the solution into Eq. (3.25) gives

$$\varepsilon^{\mathrm{vol}}(t) = -\underbrace{\left(\sum_{i=0}^{N}\frac{1}{\widetilde{K}_i} - \sum_{i=1}^{N}\frac{1}{\widetilde{K}_i}\exp\left(-\frac{t}{\widetilde{\tau}_{\mathrm{v}i}}\right)\right)}_{J(t)} p$$
$$+3\underbrace{\left(\sum_{i=0}^{N}\widetilde{\alpha}_i - \sum_{i=1}^{N}\widetilde{\alpha}_i\exp\left(-\frac{t}{\widetilde{\tau}_{\mathrm{v}i}}\right)\right)}_{\alpha(t)}\Delta\theta. \tag{3.39}$$

The bulk creep compliance $J(t)$ and the transient thermal expansion coefficient $\alpha(t)$ (Pettermann and DeSimone, 2018) are also given by Prony series. The Boltzmann superpositon integral reads

$$\varepsilon^{\mathrm{vol}}(t) = -\int_0^t J(t-s)\dot{p}(s)\,\mathrm{d}s + 3\int_0^t \alpha(t-s)\dot{\theta}(s)\,\mathrm{d}s - 3\alpha(t)\theta_0 H(t). \tag{3.40}$$

In Tab. 3.1, the instantaneous ($t \to 0$) and equilibrium material response ($t \to \infty$) of GMM and GKM are summarized.

Caloric model. To derive the Boltzmann superposition integral of the generalized caloric model, Eq. (3.31) and (3.30) are solved for a constant temperature and vanishing initial values, giving

$$s_{\mathrm{c}}(t) = -\varphi'(\theta(t)) - \underbrace{\left(\sum_{i=1}^{M} C_i\exp\left(-\frac{t}{\lambda_i}\right)\right)}_{C(t-s)}\theta. \tag{3.41}$$

With that, the Boltzmann superposition integral of the entropy reads

$$s(t) = -\varphi'(\theta(t)) - \int_0^t C(t-s)\dot{\theta}(s)\,\mathrm{d}s. \tag{3.42}$$

	GMM	GKM
K_{t0}	$\sum_{i=0}^{N} K_i$	$\widetilde{K}_0$
α_{t0}	$\beta_{t0}/(3K_{t0})$	$\widetilde{\alpha}_0$
β_{t0}	$\sum_{i=0}^{N} 3\alpha_i K_i$	$3\widetilde{\alpha}_0\widetilde{K}_0$
K_∞	K_0	$\left(\sum_{i=0}^{N} \widetilde{K}_i^{-1}\right)^{-1}$
α_∞	α_0	$\sum_{i=0}^{N} \widetilde{\alpha}_i$
β_∞	$3\alpha_0 K_0$	$3\alpha_\infty K_\infty$

Table 3.1: Stiffness, thermal expansion coefficient and temperature-stress coefficient of GMM and GKM for the limiting cases. The instantaneous material response for $t \to 0$ is denoted by the subscript $t0$, the equilibrium behavior for $t \to \infty$ by the subscript ∞.

3.3.5 Time-temperature superposition

Reduced time. In general, viscoelastic material behavior strongly depends on temperature. An increase in temperature leads to an acceleration of viscoelastic effects. The most common way to model temperature-dependency of viscoelastic properties is *thermorheological simplicity*. The basic idea is to introduce a reduced time. An increase in temperature then leads to a faster time scale. With that, the Boltzmann superposition integrals are expanded by considering a reduced time scale. As an example, the bulk relaxation modulus in Eq. (3.38) becomes

$$p(t) = -\int_0^t K(z(t) - z(s), \theta_{\mathrm{ref}}) \dot{\varepsilon}^{\mathrm{vol}}(s)\, \mathrm{d}s, \tag{3.43}$$

where the reduced time is defined by (Brinson and Brinson, 2015)

$$z(t) = \int_0^t \frac{\mathrm{d}w}{a_\theta(\theta(w))}. \tag{3.44}$$

The function $a_\theta(\theta)$ is the temperature shift function which satisfies the following properties

$$a_\theta(\theta_{\mathrm{ref}}) = 1, \quad a_\theta > 0, \quad a'_\theta(\theta) < 0 \tag{3.45}$$

(Kehrer et al., 2023). At the reference temperature θ_{ref}, the reduced time is identical to the physical time. The reference temperature of the shift function is not necessarily identical to the reference temperature θ_0 regarding thermal expansion. Often, θ_{ref} is set to the glass transition temperature.

Time shift. For isothermic processes, the temperature-dependent relaxation modulus is given by

$$K(t,\theta) = K_0 + \sum_{i=1}^{N} K_i \exp\left(-\frac{t}{a_\theta(\theta)\tau_{\mathrm{v}i}}\right) \tag{3.46}$$

(Kehrer et al., 2023). From that, it can be seen that all relaxation times of the GMM depend on temperature in the same way,

$$\tau_{\mathrm{v}i}(\theta) = a_\theta(\theta)\tau_{\mathrm{v}i0}, \quad i = 1, \ldots, N. \tag{3.47}$$

In words, the relaxation time is given by a constant reference parameter that is scaled with a temperature-dependent shift function. By definition, the same holds for the viscosities. With the temperature-dependency of the viscosities, the glass transition can be modeled, see Ch. 5. Furthermore, the following relation holds

$$K(t,\theta) = K(t/a_\theta, \theta_{\mathrm{ref}}) = K(10^{\log t - \log a_\theta}, \theta_{\mathrm{ref}}) \tag{3.48}$$

(Kehrer et al., 2023). Thus, a change in temperature leads to a shift of the relaxation modulus alongside the logarithmic time axis (time-temperature superposition). This motivates the term *(horizontal) shift function*.

WLF equation. An overview on various shift functions is, e.g., given by Tschoegl et al. (2002a). Most frequently, the WLF equation is used. The derivation of the WLF equation is shortly summarized here. It was introduced by Williams et al. (1955) and is based on the free volume theory. The free volume V_f is seen as the volume between molecules that allows for molecular motion. Therefore, an increasing free volume leads to increasing motion and, thus, to a decreasing viscosity of the material. Doolittle and Doolittle (1957) give an expression for viscosities depending on the fractional free volume f_V,

$$\eta = A \exp\left(B\left(\frac{1}{f_V} - 1\right)\right), \quad f_V = \frac{V_\mathrm{f}}{V}. \tag{3.49}$$

A linear temperature-dependency of the fractional free volume is assumed,

$$f_V = f_V^{\mathrm{ref}} + \alpha_f(\theta - \theta_{\mathrm{ref}}), \tag{3.50}$$

where α_f is the expansitivity of the fractional free volume (Tschoegl et al., 2002a). Inserting Eq. (3.50) into Eq. (3.49) and considering the ratio of the temperature-dependent viscosity and the reference viscosity then gives the WLF shift function,

$$\begin{aligned} \ln a_\theta &= \ln\left(\frac{\eta}{\eta_{\mathrm{ref}}}\right) = B\left(\frac{1}{f_V} - \frac{1}{f_V^{\mathrm{ref}}}\right) \\ &= -\frac{c_1(\theta - \theta_{\mathrm{ref}})}{c_2 + \theta - \theta_{\mathrm{ref}}}. \end{aligned} \tag{3.51}$$

Vertical shift. If, in addition to the viscosities, the stiffnesses are also temperature-dependent, TTS is not applicable. Assuming that all stiffnesses depend on temperature in the same way gives rise to an additional vertical shift alongside the logarithmic modulus axis. This can be seen as *extended TTS* (Kehrer et al., 2023) where the relaxation modulus is given by

$$K(t, \theta) = b_\theta(\theta) K_{\mathrm{ref}}(t/a_\theta, \theta_{\mathrm{ref}}). \tag{3.52}$$

An explicit expression for the vertical shift function b_θ can be derived, e.g., by the Rouse model (Rouse, 1953; Dealy and Plazek, 2009)

$$b_\theta(\theta) = \frac{\varrho\theta}{\varrho_{\mathrm{ref}}\theta_{\mathrm{ref}}}. \tag{3.53}$$

3.3.6 Conversion

To recall, the GMM is the natural model for strain-driven processes whilst the GKM is the natural model for stress-driven processes. This raises the question if both models can be converted into each other. As stated before, both models can be described by an ODE of order N, see App. A.1.1 and A.1.2. If the coefficients of the ODEs are identical, both models are equivalent. A comparion of coefficients leeds to a nonlinear equation system, see Eq. (A.6) - (A.11) and Eq. (A.15) - (A.18). In the following, a stepwise conversion of the GMM and GKM parameters is discussed.

Conversion of stiffnesses and viscosities. By looking at Eq. (3.22) and (3.28), it can be seen that the conversion of stiffnesses and viscosities can be seperated from the conversion of the thermal expansion coefficients. The comparison of coefficients regarding the time derivatives of pressure and volumetric strain is not influenced by the coefficients regarding the time derivatives of the temperature. Thus, the first step is to convert the purely mechanical parameters (stiffnesses and viscosities). Analytical solutions for first and second order models are given by Serra-Aguila et al. (2019). For higher order models, the derivation of analytical solutions becomes more and more difficult. Thus, numerical approaches seem more promising. The method by Loy et al. (2015), which is based on the Prony series representation and its Laplace transformation, is recommended here. In a first step, relaxation or retardation times are determined numerically. Subsequently, the corresponding Prony series coefficients can be calculated via analytical formulas. At the end, stiffnesses and viscosities of GMM or

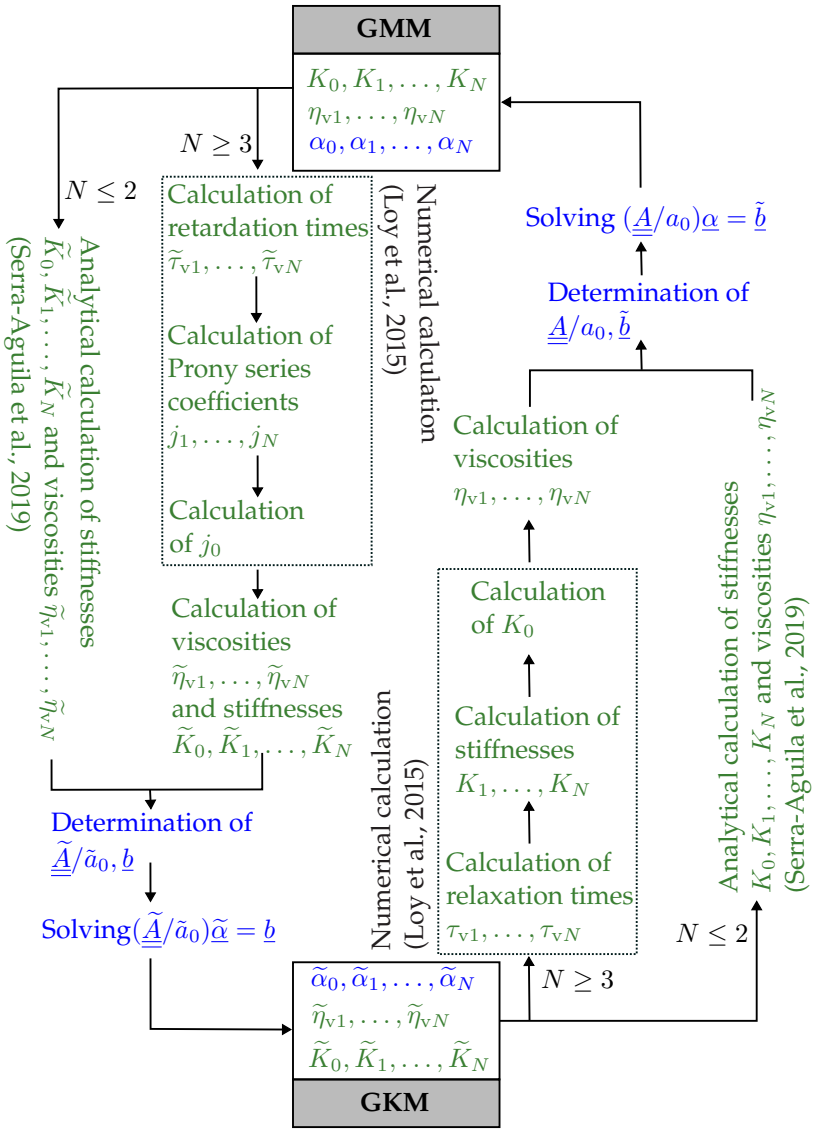

Figure 3.4: Flow diagram of the conversion of generalized thermorheological models including thermal expansion

GKM can be calculated from the determined time constants and Prony series coefficients. A description of the method is given in App. A.2 in more detail.

Conversion of thermal expansion coefficients. The next step is to convert the thermal expansion coefficients based on the already known stiffnesses and viscosities. By comparison of coefficients regarding the time derivatives of temperature in Eq. (3.22) and (3.28) and the formulas in Eq. (A.9) - (A.11) and (A.17) - (A.18), a linear equation system arises

$$\underbrace{\frac{\underline{\underline{A}}}{a_0}\underline{\alpha}}_{\underline{b}} = \underbrace{\frac{\widetilde{\underline{\underline{A}}}}{\widetilde{a}_0}\widetilde{\underline{\alpha}}}_{\widetilde{\underline{b}}}, \tag{3.54}$$

$$\underline{\alpha} = (\alpha_0, \alpha_1, \ldots, \alpha_N)^{\mathsf{T}}, \quad \widetilde{\underline{\alpha}} = (\widetilde{\alpha}_0, \widetilde{\alpha}_1, \ldots, \widetilde{\alpha}_N)^{\mathsf{T}}.$$

Depending on the generalized thermorheological model that is used as input, either the vector $\underline{b}$ or the vector $\widetilde{\underline{b}}$ is known. Furthermore, based on the preciding conversion of stiffnesses and viscosities, the matrix $\underline{\underline{A}}/a_0$ or $\widetilde{\underline{\underline{A}}}/\widetilde{a}_0$ is also known. Thus, it is evident that the conversion of thermal expansion coefficients is conducted by solving a linear equation system. A flow diagram of the whole method is shown in Fig. 3.4.

Temperature-dependency. It has to be noted that the precedingly described method is based on a derivation where the dependency of the viscosities on temperature was not considered. If time-temperature superposition holds, however, the method can still be applied. In case of TTS, the temperature-dependency of the viscosities is given by a temperature-dependent scaling factor that is identical for all viscosities. By assuming that this factor is identical for the GMM and the GKM, the shift function has no effect on the comparison of coefficients of Eq. (3.22) and (3.28). The

same holds for a vertical shift function where all stiffnesses depend on temperature in the same way.

3.4 Three-dimensional viscoelasticity

3.4.1 Anisotropic viscoelasticity

In Sec. 3.2 and 3.3, thermoviscoelastic behavior was only considered for purely volumetric deformations. In this section, an expansion of the GMM (Fig. 3.2) for a general deformation is shown. The basic structure does not change. For the anisotropic GMM, the stiffnesses of the springs are given by the stiffness tensors $\mathbb{C}_i$, the viscosities are given bis viscosity tensors $\mathbb{V}_i$, and the thermal expansion coefficient tensors are $\boldsymbol{\alpha}_i$. The viscous strains are now given by second order tensors $\boldsymbol{\varepsilon}_{\mathrm{v}i}$. Then, the free energy with the strain tensor as natural state variable is given by

$$\begin{aligned}\psi_{\mathrm{m}}(\boldsymbol{\varepsilon}, \boldsymbol{\varepsilon}_{\mathrm{v}1}, \ldots, \boldsymbol{\varepsilon}_{\mathrm{v}N}, \theta) =& \frac{\mathbb{C}_0}{2\varrho_0}[\boldsymbol{\varepsilon} - \boldsymbol{\alpha}_0\Delta\theta] \cdot (\boldsymbol{\varepsilon} - \boldsymbol{\alpha}_0\Delta\theta) \\ &+ \sum_{i=1}^{N} \frac{\mathbb{C}_i}{2\varrho_0}[\boldsymbol{\varepsilon} - \boldsymbol{\varepsilon}_{\mathrm{v}i} - \boldsymbol{\alpha}_i\Delta\theta] \cdot (\boldsymbol{\varepsilon} - \boldsymbol{\varepsilon}_{\mathrm{v}i} - \boldsymbol{\alpha}_i\Delta\theta).\end{aligned} \tag{3.55}$$

By linear irreversible thermodynamics, the evolution equations are defined

$$\begin{aligned}\dot{\boldsymbol{\varepsilon}}_{\mathrm{v}i} &= -\varrho_0 \mathbb{V}^{-1} \frac{\partial \psi_{\mathrm{m}}}{\partial \boldsymbol{\varepsilon}_{\mathrm{v}i}} \\ &= \mathbb{V}_i^{-1} \underbrace{\mathbb{C}_i[\boldsymbol{\varepsilon} - \boldsymbol{\varepsilon}_{\mathrm{v}i} - \boldsymbol{\alpha}_i\Delta\theta]}_{\boldsymbol{\sigma}_{\mathrm{v}i}}, \quad i = 1, \ldots, N,\end{aligned} \tag{3.56}$$

where the viscosity tensors $\mathbb{V}_i$ must be semi-positive definite to satisfy the Clausius-Duhem inequaltiy. The resulting Cauchy stress is given by

$$\boldsymbol{\sigma} = \varrho_0 \frac{\partial \psi_{\mathrm{m}}}{\partial \boldsymbol{\varepsilon}} = \mathbb{C}_i[\boldsymbol{\varepsilon} - \boldsymbol{\alpha}_0 \Delta\theta] + \sum_{i=1}^{N} \mathbb{C}_i[\boldsymbol{\varepsilon} - \boldsymbol{\varepsilon}_{\mathrm{v}i} - \alpha \Delta\theta] \tag{3.57}$$

$$= \int_0^t \mathbb{C}(t-s)[\dot{\boldsymbol{\varepsilon}}(s)]\,\mathrm{d}s - \int_0^t \boldsymbol{\beta}(t-s)\dot{\theta}(s)\,\mathrm{d}s + \boldsymbol{\beta}(t)\theta_0 H(t), \tag{3.58}$$

where the Boltzmann superposition is applied to tensors. The temperature-stress coefficients are denoted by $\boldsymbol{\beta}_i = \mathbb{C}_i[\boldsymbol{\alpha}_i]$. For completeness, the dissipation potential is given

$$\Phi_{\mathrm{m}}(-\frac{\boldsymbol{\sigma}_{\mathrm{v}1}}{\varrho_0}, \ldots, -\frac{\boldsymbol{\sigma}_{\mathrm{v}N}}{\varrho_0}) = \sum_{i=1}^{N} \frac{\varrho_0}{2} \mathbb{V}_i^{-1} \left[-\frac{\boldsymbol{\sigma}_{\mathrm{v}i}}{\varrho}\right] \cdot \left(-\frac{\boldsymbol{\sigma}_{\mathrm{v}i}}{\varrho}\right). \tag{3.59}$$

3.4.2 Isotropic viscoelasticity

By assuming isotropic material behavior, the stiffnesses and viscosities are given by their spectral decompositions,

$$\mathbb{C}_i = 3K_i \mathbb{P}_1 + 2G_i \mathbb{P}_2, \quad \mathbb{V}_i = 3\eta_{\mathrm{v}i} \mathbb{P}_1 + 2\eta_{\mathrm{s}i} \mathbb{P}_2. \tag{3.60}$$

The shear moduli are denoted by G_i and the shear viscosities by $\eta_{\mathrm{s}i}$. Due to the isotropy, the deviatoric and the spherical part of the material response can be considered seperately,

$$\psi_{\mathrm{m}} = \psi_{\mathrm{m}}^{\mathrm{vol}}(\varepsilon^{\mathrm{vol}}, \varepsilon_1^{\mathrm{vol}}, \ldots, \varepsilon_N^{\mathrm{vol}}, \theta) + \psi_{\mathrm{m}}^{\mathrm{dev}}(\boldsymbol{\varepsilon}', \boldsymbol{\varepsilon}'_{\mathrm{v}0}, \ldots, \boldsymbol{\varepsilon}'_{\mathrm{v}N}). \tag{3.61}$$

The decomposition of the strain and the stress is given by

$$\boldsymbol{\varepsilon} = \boldsymbol{\varepsilon}' + \frac{1}{3}\varepsilon^{\mathrm{vol}} \boldsymbol{I}, \quad \boldsymbol{\sigma} = \boldsymbol{\sigma}' - p\boldsymbol{I}. \tag{3.62}$$

As the spherical part was already discussed in Sec. 3.3, only the governing equations of the deviatoric part are shown here. The derivation of the equations is completely analog. However, as, in case of isotropy, thermal expansion is a purely volumetric deformation, the corresponding terms do not exist for shear deformations. The deviatoric part of the free energy is

$$\psi_{\mathrm{m}}^{\mathrm{dev}}(\boldsymbol{\varepsilon}', \boldsymbol{\varepsilon}'_{\mathrm{v}0}, \ldots, \boldsymbol{\varepsilon}'_{\mathrm{v}N}) = \frac{G_0}{\varrho_0}\boldsymbol{\varepsilon}' \cdot \boldsymbol{\varepsilon}' + \sum_{i=1}^{N} \frac{G_i}{\varrho_0}(\boldsymbol{\varepsilon}' - \boldsymbol{\varepsilon}'_i) \cdot (\boldsymbol{\varepsilon}' - \boldsymbol{\varepsilon}'_i). \tag{3.63}$$

Thus, the evolution equations of the deviatoric viscous strains are

$$\dot{\boldsymbol{\varepsilon}}'_{\mathrm{v}i} = -\frac{\varrho_0}{2\eta_{\mathrm{s}i}} \frac{\partial \psi_{\mathrm{m}}^{\mathrm{dev}}}{\partial \boldsymbol{\varepsilon}'_{\mathrm{v}i}} = \underbrace{\frac{G_i}{\eta_{\mathrm{s}i}}}_{1/\tau_{\mathrm{s}i}} (\boldsymbol{\varepsilon}' - \boldsymbol{\varepsilon}'_{\mathrm{v}i}), \quad i = 1, \ldots, N, \tag{3.64}$$

where $\tau_{\mathrm{s}i}$ are the shear relaxation times. The additive decomposition of the deviatoric stress and its Boltzmann superposition integral are given by

$$\begin{aligned} \boldsymbol{\sigma}' = \varrho_0 \frac{\partial \psi_{\mathrm{m}}^{\mathrm{dev}}}{\partial \boldsymbol{\varepsilon}'} &= 2G_0\boldsymbol{\varepsilon}' + \sum_{i=1}^{N} \underbrace{2G_i(\boldsymbol{\varepsilon}' - \boldsymbol{\varepsilon}'_{\mathrm{v}i})}_{\boldsymbol{\sigma}'_{\mathrm{v}i}} \\ &= 2\int_0^t G(t-s)\dot{\boldsymbol{\varepsilon}}'(s)\,\mathrm{d}s. \end{aligned} \tag{3.65}$$

The dissipation potential reads

$$\Phi_{\mathrm{m}}^{\mathrm{dev}}(\boldsymbol{\sigma}'_{\mathrm{v}1}, \ldots, \boldsymbol{\sigma}'_{\mathrm{v}N}) = \sum_{i=1}^{N} \frac{\varrho_0}{2\eta_{\mathrm{s}i}} \left(-\frac{\boldsymbol{\sigma}'_{\mathrm{v}i}}{\varrho_0}\right) \cdot \left(-\frac{\boldsymbol{\sigma}'_{\mathrm{v}i}}{\varrho_0}\right). \tag{3.66}$$

Viscoelastic moduli. In elasticity, various elastic parameters are defined, e.g., Young's modulus E, shear modulus G, bulk modulus K, or Poisson's ratio ν. For an isotropic material, only two of these parameters are independent. If the Laplace tranformation of, e.g., Eq. (3.58) is considered

under neglection of thermal expansion, the linear relation

$$\mathcal{L}(\boldsymbol{\sigma}) = s\mathcal{L}(\mathbb{C})(s)[\mathcal{L}(\boldsymbol{\varepsilon})(s)] \tag{3.67}$$

arises. With that, it is evident that the known relations between the elastic moduli must also hold for the viscoelastic moduli on the Laplace domain (Brinson and Brinson, 2015),

$$s\mathcal{L}(G) = \frac{s\mathcal{L}(E)}{2(1 + s\mathcal{L}(\nu))}, \quad s\mathcal{L}(K) = \frac{s\mathcal{L}(E)}{3(1 - 2s\mathcal{L}(\nu))}. \tag{3.68}$$

Thus, in general, Poisson's ratio is a time-dependent function. In case of a constant Poisson's ratio ν_0, the ratios between the relaxation moduli are given by constants (Brinson and Brinson, 2015),

$$G(t) = \frac{E(t)}{2(1 + \nu_0)}, \quad K(t) = \frac{E(t)}{3(1 - 2\nu_0)}. \tag{3.69}$$

For the Prony series representation, this means that the distribution of relaxation times is the same for $G(t)$, $K(t)$ and $E(t)$. Furthermore, the elastic moduli of each spring element in a generalized thermorheological model can be converted by the relations known from elasticity. If $\nu_0 = 0.5$ holds, the materials is incompressible, $K(t) = \infty$ (Brinson and Brinson, 2015).

3.5 Summary of results

In this chapter, a detailed overview on the theory of linear thermoviscoelasticity was given. By first order models, the analogy of viscoelastic and viscocaloric behavior, or stress relaxation and entropy relaxation was shown. The generalization of the thermoviscoelastic models to account for superposition of multiple relaxation processes was also discussed. It was demonstrated that, depending on whether the stress or the strain

is a natural state variable, either the GKM or the GMM is more suitable. Furthermore, a conversion method between GMM and GKM including thermal expansion coefficients was introduced. It was shown that the conversion of stiffnesses and viscosities can be seperated from the conversion of thermal expansion coefficients. The former can be conducted in a first step by applying a conversion method from literature. It was demonstrated that based on the already determined stiffnesses and viscosities, a linear equation system for the conversion of thermal expansion coefficients is given.

Chapter 4

Viscoelasticity in polyamide 6

4.1 Introduction

In this chapter, the viscoelastic part of the thermoviscoelastic model introduced in Ch. 3 is applied. An experimental characterization of PA6 that acounts for hydrothermal influences serves as input. The steps that are required to identify a temperature- and humidity-dependent GMM are discussed in detail. Furthermore, the limitations and restrictions of the model are shown. First, the governing equations of the temperature-dependent GMM for a uniaxial load case are derived in Sec. 4.2. The methods of master curve construction and parameter identification are given in Sec. 4.3. A discussion on master curves and parameter identification based on experimental data of PA6 is given in Sec. 4.4. It has to be noted that the following considerations do not account for any inhomogeneities within the material, e.g., moisture gradients or semicrystallinity. Thus, the displayed material properties describe the effective material behavior of PA6 for the considered testing conditions.

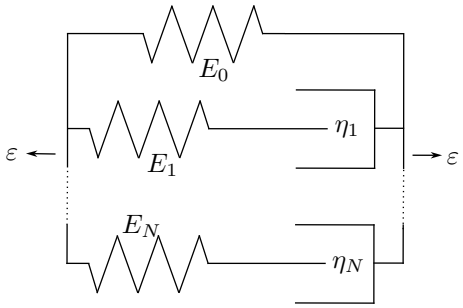

Figure 4.1: Generalized Maxwell model for a uniaxial stress state. The stiffnesses of the springs are denoted by the Young's moduli E_i and the viscosities by η_i.

4.2 Viscoelastic model

4.2.1 Uniaxial GMM

The experimental input in this chapter is given by uniaxial load cases. This means that a longitudinal strain $\varepsilon(t)$ is prescribed. As lateral strains are permitted, a uniaxial stress state results. By assuming isotropic material behavior, the strain and the stress are therefore given by

$$\boldsymbol{\varepsilon}(t) = \varepsilon(t)\boldsymbol{e}_x \otimes \boldsymbol{e}_x - \nu(t)\varepsilon(t)[\boldsymbol{e}_y \otimes \boldsymbol{e}_y + \boldsymbol{e}_z \otimes \boldsymbol{e}_z], \tag{4.1}$$

$$\boldsymbol{\sigma}(t) = \sigma(t)\boldsymbol{e}_x \otimes \boldsymbol{e}_x \tag{4.2}$$

The lateral strain $\nu(t)\varepsilon(t)$ is not measured in the considered experiments. Thus, a scalar model regarding the x-components is used in the following. Due to the prescribed strain, a GMM is suitable. The GMM in Sec. 3.3.1 is adapted for uniaxial stress states, thermal strains are neglected. In Fig. 4.1, the resulting model is illustrated. The stress response is given by

$$\sigma(t) = E_0\varepsilon + \sum_{i=1}^{N} E_i(\varepsilon - \varepsilon_{\mathrm{v}i}) \tag{4.3}$$

and the evolution equations read

$$\dot{\varepsilon}_{\mathrm{v}i} = \underbrace{\frac{E_i}{\eta_i}}_{1/\tau_i} (\varepsilon - \varepsilon_{\mathrm{v}i}), \quad i = 1, \ldots, N. \tag{4.4}$$

The relaxation modulus, analog to Eq. (3.37), is given by the Prony series

$$E(t) = E_0 + \sum_{i=1}^{N} E_i \exp\left(-\frac{t}{\tau_i}\right). \tag{4.5}$$

4.2.2 Cyclic loading

The consideration in this chapter is furthermore restricted to cyclic loadings. In this case, analog to linear elasticity, a linear relation between the complex stress and the complex strain can be formulated (Brinson and Brinson, 2015)

$$\sigma^*(t) = E^*(i\omega)\varepsilon^*(t), \quad \varepsilon^*(t) = \Delta\varepsilon \exp(i\omega t). \tag{4.6}$$

Note that this is only valid for a steady state. The complex modulus is denoted by E^*, the angular frequency of the load by ω. Applying the Boltzmann superposition integral, cf. Eq. (3.35), yields

$$\sigma^*(t) = \int_{-\infty}^{t} E(t-s)\dot{\varepsilon}^*(s)\,\mathrm{d}s \tag{4.7}$$

$$= i\omega\Delta\varepsilon \int_{-\infty}^{t} E(t-s)\exp(i\omega s)\,\mathrm{d}s. \tag{4.8}$$

Next, s is substituted by $u = t - s$ (Brinson and Brinson, 2015), which gives

$$\sigma^*(t) = \Delta\varepsilon \exp(i\omega t)\left(i\omega \int_0^{\infty} E(u)\exp(-i\omega u)\,\mathrm{d}u\right). \tag{4.9}$$

Comparing with Eq. (4.6) shows that the complex modulus is given by

$$E^*(i\omega) = i\omega \int_0^\infty E(t) \exp(-i\omega t)\, \mathrm{d}t = E'(\omega) + iE''(\omega). \tag{4.10}$$

It can be seen that the complex modulus is the half-sided Fourier transformation scaled with $i\omega$ (Brinson and Brinson, 2015). The real part of the complex modulus is the storage modulus E' and the imaginary part is the loss modulus E''. The storage modulus is related to the elastic, non-dissipative part of the material response whilst the loss modulus is related to the viscous, dssipative part of the material response. By inserting Eq. (4.5) into (4.10), the storage and loss modulus can be calculated (Brinson and Brinson, 2015)

$$E'(\omega) = E_0 + \sum_{i=1}^{N} \frac{E_i(\omega\tau_i)^2}{1 + (\omega\tau_i)^2}, \tag{4.11}$$

$$E''(\omega) = \sum_{i=1}^{N} \frac{E_i\omega\tau_i}{1 + (\omega\tau_i)^2}. \tag{4.12}$$

The asymptotic behavior of storage and loss modulus is given by

$$\lim_{\omega\to 0} E' = E_0, \quad \lim_{\omega\to 0} E'' = 0, \tag{4.13}$$

$$\lim_{\omega\to \infty} E' = \sum_{i=0}^{N} E_i, \quad \lim_{\omega\to \infty} E'' = 0, \tag{4.14}$$

cf. Kehrer et al. (2023). In both limiting cases, the material response is elastic with a lower stiffness for very slow loadings and a higher stiffness for very fast loadings.

4.2.3 Temperature-frequency sweeps

As input for a GMM parameter identification, experimental measurements from cyclic DMA tests are used. Therefore, temperature-frequency tests

are considered. In these tests, the temperature is increased in steps. At each temperature level, a sinusoidal strain load with various frequencies $f = \omega/(2\pi)$ is applied (Kehrer et al., 2023),

$$\varepsilon(t) = \varepsilon_0 + \Delta\varepsilon \sin(\omega t). \tag{4.15}$$

A static preload ε_0 is superposed. For each of these frequencies, the steady-state stress response is measured by its amplitude $\Delta\sigma$ and the phase shift δ (Kehrer et al., 2023),

$$\sigma(t) = \sigma_0 + \Delta\sigma \sin(\omega t + \delta). \tag{4.16}$$

Using Eq. (4.6) and (4.10), the storage and loss modulus are then given by

$$E' = \frac{\Delta\sigma}{\Delta\varepsilon}\cos(\delta), \quad E'' = \frac{\Delta\sigma}{\Delta\varepsilon}\sin(\delta), \tag{4.17}$$

cf. Kehrer et al. (2023). The loss factor $\tan\delta$ defines the dissipative part of the material response and is calculated by (Kehrer et al., 2023)

$$\tan\delta = \frac{E''}{E'}. \tag{4.18}$$

4.2.4 Extended time-temperature superposition

Applying extended TTS, cf. Eq. (3.47) and (3.52), to storage and loss modulus in Eq. (4.11) and (4.12) gives

$$E^{(\cdot)}(\omega, \theta) = b_\theta(\theta) E^{(\cdot)}_{\mathrm{ref}}(a_\theta(\theta)\omega, \theta_{\mathrm{ref}}), \tag{4.19}$$

$$\log E^{(\cdot)}(\omega, \theta) = \log b_\theta + \log\left(E^{(\cdot)}_{\mathrm{ref}}\left(10^{\log\omega + \log a_\theta}, \theta_{\mathrm{ref}}\right)\right) \tag{4.20}$$

(Kehrer et al., 2023). This relation holds for both storage and loss modulus. Analog to the reduced time t/a_θ, a reduced frequency is given by $a_\theta\omega$. On the logarithmic frequency domain, an increase in temperature is related

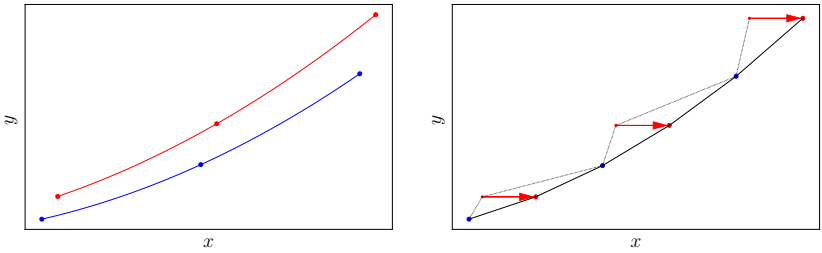

(a) Initial state **(b)** Shift of the red curve

Figure 4.2: Visualization of the shift method. The plots are taken from Figure 1 in Kehrer et al. (2023).

to a (horizontal) shift to lower frequencies. The function a_θ defines a temperature-dependency of the viscosities whilst the function b_θ is related to a temperature-dependency of the Young's moduli and causes a vertical shift.

4.3 Methods

4.3.1 Shift method[1]

In experimental testing, a limited range of frequency can be considered. TTS enables to combine experimental data at different temperature levels to obtain a single master curve by shifting. Thereby, viscoelastic behavior can be characterized for a larger frequency range. To avoid manual shifting, numerical shift methods can be applied.

[1] This subsection is based on the subsection *Method of normalized arc length minimization* in Kehrer et al. (2023).

Method of normalized arc length minimization. The method used in this work is based on the work by Bae et al. (2011). This method is chosen due to its simple implementation and lower requirements to the number of data points. The idea of the method is visualized by Fig. 4.2. On the left, two curves are representatively given. The red curve needs to be shifted and the blue curve serves as reference curve. The shift of the red curve to the final position is shown on the right. For an automated method, a quantitative parameter is defined. In this context, the arc length $l(a)$ is introduced as a function of the shift a. The method determines the shift that minimizes the arc length. Therefore, global optimization is used

$$l(a) \longrightarrow \min_{a \in [a_\mathrm{L}, a_\mathrm{U}]}. \tag{4.21}$$

The lower and upper bounds for the shift, a_L and a_U, are prescribed by the user. Each increment of the global optimization scheme has the following structure

1. Define the reference curve by L_1 and the shifted curve by L_2

$$L_1 = \{(x_1^{(1)}, y_1^{(1)}), \ldots, (x_m^{(1)}, y_m^{(1)})\}, \tag{4.22}$$
$$L_2 = \{(x_1^{(2)} + a, y_1^{(2)}), \ldots, (x_n^{(2)} + a, y_n^{(2)})\}. \tag{4.23}$$

   The number of data points in each list is given by m and n respectively.

2. Combine both lists and sort the resulting list by the x-values in ascending order

$$L = L_1 \cup L_2 := \{(x_1, y_1), \ldots, (x_{m+n}, y_{m+n})\}, \tag{4.24}$$
$$x_1 \leq x_2 \leq \cdots \leq x_{m+n}.$$

3. Calculate the normalized arc length

$$l(a) = \sum_{i=1}^{m+n} \sqrt{\left(\frac{x_{i+1} - x_i}{x_{m+n} - x_1}\right)^2 + \left(\frac{y_{i+1} - y_i}{y_{m+n} - y_1}\right)^2}. \tag{4.25}$$

The method extends the method presented in Bae et al. (2011) and Cho (2009) by normalizing the partial arc lengths with the total x- and y-range. Thereby, the increasing x-range due to shifting is taken into account, see Fig. 4.2b. By swapping x- and y-data, the method can also be applied for vertical shifts. Dual Annealing optimization implemented by the `scipy` package in `Python` is used to solve the minimization problem.

Master curve construction. The shift method will be applied to data from temperature-frequency sweeps. The measured $\tan\delta(\omega)$ and $E'(\omega)$ curves at various temperature levels serve as input. First, the horizontal shift factor a_θ will be determined by using the loss factor since it is not affected by a vertical shift (Bae et al., 2011; Gergesova et al., 2016). Starting from the lowest temperature, the relative shifts between neighboring curves are calculated by the shift method with $a \mathrel{\widehat{=}} \log a_\theta^{(\mathrm{rel})}$, $x \mathrel{\widehat{=}} \log\omega$, and $y \mathrel{\widehat{=}} \tan\delta$. The number of temperature levels is denoted by n_θ and the results are given by

$$\log a_\theta^{(\mathrm{rel})}(\theta_i), \quad \theta_i < \theta_{i+1}, \quad i = 2, \ldots, n_\theta. \tag{4.26}$$

The relative shift at the lowest temperature is set to zero. The total shifts are then calculated by

$$\log a_\theta(\theta_i) = -\log a_\theta^{(\mathrm{rel})}(\theta_{\mathrm{ref}}) + \sum_{j=1}^{i} \log a_\theta^{(\mathrm{rel})}(\theta_j), \quad i = 1, \ldots, n_\theta. \tag{4.27}$$

The reference temperature can be arbitrarely chosen from θ_i. In a second step, the vertical shift is determined. In this context, the above described procedure is repeated with $a \widehat{=} -\log b_\theta^{(\mathrm{ref})}$, $x \widehat{=} \log E'$ and $y \widehat{=} \log \omega$.

4.3.2 Parameter identification[2]

The last step is to identify parameters for a GMM based on given master curves. This means that a set of $2N + 1$ parameters must be identified

$$\widetilde{\mathcal{P}}_N = \{E_0, E_1, \ldots, E_N, \tau_1, \ldots, \tau_N\}. \tag{4.28}$$

In general, this is an ill-posed problem as no unique solution exists (Honerkamp and Weese, 1989; Ghobadi et al., 2015). This problem can be solved by prescribing a distribution of relaxation times. In this work, a logarithmic distribution is used (Bradshaw and Brinson, 1997; Honerkamp and Weese, 1990). Then, only $N + 1$ stiffnesses need to be identified

$$\mathcal{P}_N = \{E_0, E_1, \ldots, E_N\}. \tag{4.29}$$

The number N of Maxwell elements is also prescribed. As a rule of thumb, at least one element per considered frequency decade should be used (Ghobadi et al., 2015; Göhler, 2011). Least squares minimization is used to solve the problem (Bradshaw and Brinson, 1997; Jalocha et al., 2015). Previously, four viscoelastic properties (E', E'', E^*, $\tan\delta$) were introduced for the dynamic load case. Only two of these properties are independent. Here, storage and loss modulus are used as input for the residual (Göhler, 2011; Jalocha et al., 2015). Formally, the master curves are defined by the data points $\{\omega_i, E_i'\}$ and $\{\omega_i, E_i''\}$ for $i = 1, \ldots, n_\omega$, where n_ω represents

[2] This subsection is based on the subsection *Parameter identification* in Kehrer et al. (2023).

the number of data points. The residual is given by

$$r^2(\mathcal{P}_N) = a' \sum_{i=1}^{n_\omega} \left(\frac{E'_i - E'(\omega_i, \mathcal{P}_N)}{E'} \right)^2 + a'' \sum_{i=1}^{n_\omega} \left(\frac{E''_i - E''(\omega_i, \mathcal{P}_N)}{E''} \right)^2 . \tag{4.30}$$

The coefficients a' and a'' allow to weight the residuals of storage and loss modulus (Zink, 2021). The constraints

$$a' + a'' = 1, \quad a' \geq 0, \quad a'' \geq 0 \tag{4.31}$$

are considered. The `scipy` package in `Python` is used to determine an optimal stiffness distribution by a gradient-based optimization method (L-BFGS-B). The stiffnesses are forced to be non-negative.

4.4 Master curves

4.4.1 Experimental input

Experimental temperature-frequency sweeps of PA6 serve as input for the construction of master curves. As the thermoviscoelastic characterization is not part of this work, the experimental methods and results are shortly summarized here. For more details, the reader is referred to Kehrer et al. (2023). The temperature-frequency sweeps were performed by DMA. Two conditioning states of the samples were considered: dry-as-molded (DAM) and ATM-23/50. In the DAM state, the moisture content is less than $0.3\mathrm{wt.\%}$ (Jia and Kagan, 2001). The ATM-23/50 state (ISO 291, 2008) represents standard atmosphere, $23°\mathrm{C}$ and $50\%\mathrm{RH}$, and a moisture content between $2.5\mathrm{wt.\%}$ and $3\mathrm{wt.\%}$ (Vlasveld et al., 2005). Various strain loads were applied with the ratio of strain amplitude $\Delta\varepsilon$ and mean strain ε_0 being the same for all tests. Two tests were performed under humidity control (HC). The testing parameters and the considered frequency and temperature ranges are summarized in Tab. 4.1. In Fig. 4.3, the results of the

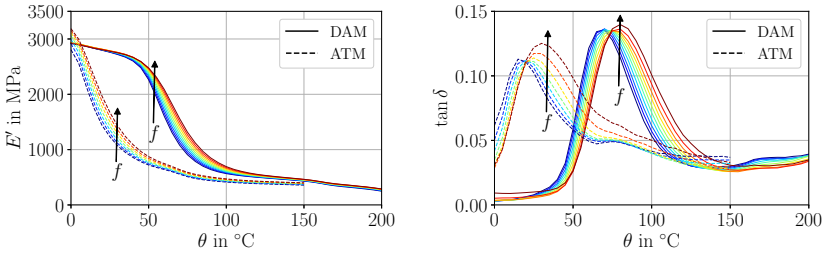

(a) Storage modulus

(b) Loss factor

Figure 4.3: Plot of the temperature-frequency tests at $\varepsilon_0 = 0.1\%$. The frequency is increased from 0.5 Hz (dark blue) to 50 Hz (dark red). DAM and ATM conditioned samples are compared. The plots regarding the DAM sample are taken from Figure 3 in Kehrer et al. (2023).

tests performed at $\varepsilon_0 = 0.1\%$ without humidity control are representatively shown. In both cases, the glass transition can be seen. During the glass transition, there is a significant drop in stiffness represented by the storage modulus. The plot of the loss factors shows that there are pronounced viscoelastic effects during the glass transition. Thus, the temperature at which the loss factor reaches its maximum is often defined as the glass transition temperature (Ehrenstein, 2011). In addition, the curves show frequency-dependent behavior during the glass transition. For the DAM sample, the glass transition temperature shifts from approximately $70°\mathrm{C}$ to $80°\mathrm{C}$ with an increase of the frequency from 0.5 Hz to 50 Hz. In contrast, for the ATM sample, the glass transition temperature shifts from approximately $15°\mathrm{C}$ to $30°\mathrm{C}$. It can be noted that the glass transition temperature is shifted by 50 K between the two conditioning states. An increase of the sample's water content leads to a lower glass transition temperature. The strong impact of humidity or moisture content on the viscoelastic behavior of PA6 is also reported in literature, cf., e.g., Venoor et al. (2021).

Conditioning	HC	ε_0 in %	$\Delta\varepsilon$ in %	f in Hz	θ in °C
DAM	–	0.1	0.05	$0.5 - 50$	$0 - 200$
DAM	–	0.3	0.15	$0.5 - 50$	$0 - 200$
DAM	–	0.5	0.25	$0.5 - 50$	$0 - 200$
ATM-23/50	–	0.1	0.05	$0.5 - 50$	$0 - 150$
ATM-23/50	–	0.3	0.15	$0.5 - 50$	$0 - 150$
DAM	20%RH	0.1	0.05	$0.5 - 50$	$10 - 70$
ATM-23/50	50%RH	0.1	0.05	$0.5 - 50$	$10 - 100$

Table 4.1: Summary of the testing parameters, cf. Kehrer et al. (2023).

4.4.2 Master curve construction

In the following, the construction of master curves is discussed in detail. Before applying the shift method, Cole-Cole plots can be used to estimate if TTS can be applied successfully (Kehrer et al., 2023), see App. B.1. Then, the shift method is applied. The temperature-frequency test of the DAM sample depicted in Fig. 4.3 is used as example here.

Horizontal shifting.[3] In the first iteration, horizontal shifts are determined for the whole set of experimental data of the loss factor to identify limitations of TTS. The reference temperature θ_{ref} is set to $75°\mathrm{C}$ which is an approximation of the glass transition temperature. In Fig. 4.4, the dotted lines represent the measured $\tan(\delta)(\omega)$ curves at various temperature levels (initial state). The solid lines depict the horizontally shifted curves (step I) where the temperature is increasing from the right ($0°\mathrm{C}$) to the left ($200°\mathrm{C}$). At the reference temperature, the respective initial and shifted curve coincide. A smooth master curve should be obtained in domains where TTS is applicable. In general, all partial curves deviate

[3] This paragraph is based on the paragraph *Horizontal shifting* of Section 3 in Keursten et al. (2023).

from the master curve at higher physical frequencies at the right due to an increase of the loss factor. Thus, the measurements at $f > 20$ Hz are not considered in the second iteration. Furthermore, for the highest and lowest temperatures, TTS is also not applicable, see Fig. 4.5. The domains of the highest and lowest temperatures are magnified on the left and on the right respectively. For the highest temperatures, no smooth master curve can be obtained by the shift method. By neglecting the highest frequencies of the partial curves for $\theta \leq 130°\mathrm{C}$, a smooth curve is expected in the second iteration. The curves at $\theta > 130°\mathrm{C}$ are not considered in the second iteration. For the four lowest temperatures, the partial curves are nearly constant if the highest frequencies are neglected. Thus, horizontal shifting does not result in a smooth master curve. The measurements for $\theta < 20°\mathrm{C}$ are not considered in the second iteration. In Fig. 4.6, the result of the second iteration is depicted. A smooth master curve is obtained for the loss factor.

Vertical shifting.[4] Next, the determined horizontal shifts are applied to storage modulus and loss modulus. The result is depicted by the dashed lines in Fig. 4.7. Especially for lower temperatures, the partial curves do not form a smooth master curve. Therefore, vertical shifts are necessary. The vertical shifts are determined based on the storage modulus resulting to the solid lines. In Fig. 4.7b, the calculated shifts are also applied to the loss modulus. Both storage and loss modulus show smooth master curves after horizontal and vertical shifting. The loss factor is not affected by a vertical shift as it is defined as ratio of loss modulus and storage modulus.

[4] This paragraph is based on the paragraph *Vertical shifting* of Section 3 in Keursten et al. (2023).

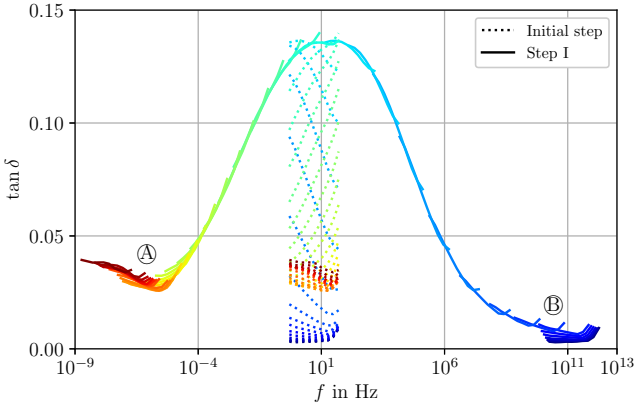

Figure 4.4: Horizontal shifting is applied to the loss factor. The initial state is depicted by the dotted curves. The solid lines result from shifting the dotted lines (step I). The reference temperature is $\theta_{\mathrm{ref}} = 75°\mathrm{C}$. This plot is based on Figure 1 in Keursten et al. (2023), the reference temperature is adapted.

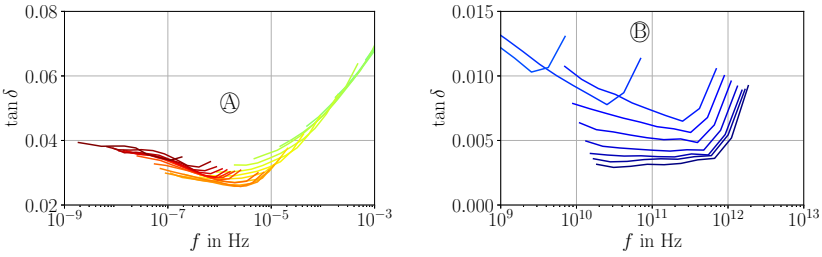

(a) High temperatures

(b) Low temperatures

Figure 4.5: Magnification of the left and right end from the master curve in Fig. 4.4. The two domains correspond with the highest and lowest temperature levels. As no smooth master curve results, TTS is not applicable in these domains. These plots are based on Figure 2 in Keursten et al. (2023), the reference temperature is adapted.

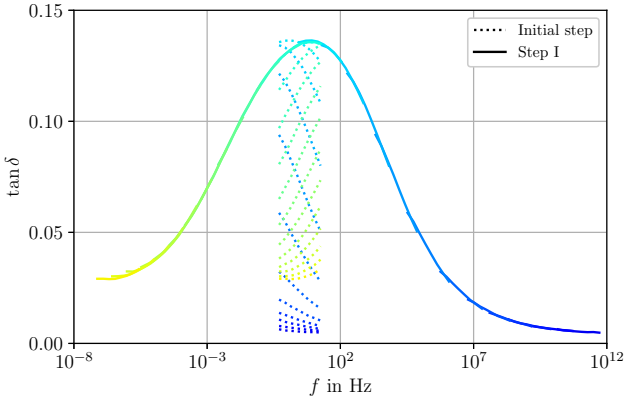

Figure 4.6: Horizontal shifting is applied to the loss factor regarding the reduced set of experimental data. The initial state is depicted by the dotted curves. The solid lines result from shifting the dotted lines (step I). The reference temperature is $\theta_{\mathrm{ref}} = 75\,^{\circ}\mathrm{C}$. This plot is based on Figure 1 in Keursten et al. (2023), the reference temperature is adapted.

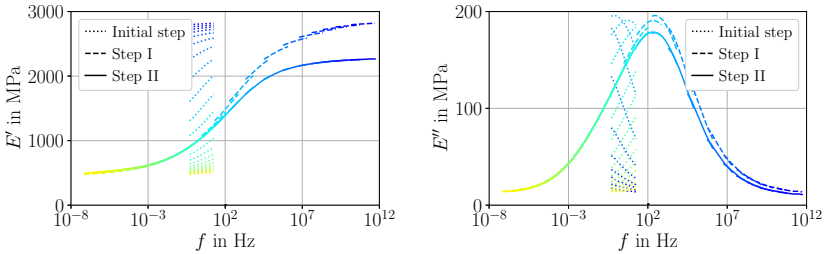

(a) Storage modulus

(b) Loss modulus

Figure 4.7: Extended TTS is applied to E' and E''. The initial state is shown by the dotted curves. By horizontal shifting, the dashed curves result (step 1). Additional vertical shifting yields the solid lines (step 2). These plots are based on Figure 5 and Figure 6 in Keursten et al. (2023), the reference temperature is adapted.

4.4.3 Discussion of master curves[5]

The procedure described above is applied to all temperature-frequency tests. In Tab. 4.2, the considered frequency and temperature ranges, and the reference temperatures are given. The reference temperature is set to the corresponding approximated glass transition temperature for each test, $\theta_{\mathrm{ref}} = 75°\mathrm{C}$ for DAM samples tested without humidity control, $\theta_{\mathrm{ref}} = 60°\mathrm{C}$ for DAM samples tested under humidity control, and $\theta_{\mathrm{ref}} = 25°\mathrm{C}$ for ATM samples. In all cases, the highest frequency levels are neglected to obtain smooth master curves. Thus, TTS is limited to a physical frequency lower than 20 Hz. This does not contradict the plots in Figure 4.7 since these plots include frequencies above the limit of 20 Hz in the sense of reduced frequencies. With increasing moisture, the temperature range, in which TTS is applicable, is shifted to lower temperatures. This can be seen by comparing DAM and ATM samples. For $\varepsilon_0 \leq 0.3\%$, TTS is valid and the limitations in temperature and frequency range are not affected by the load level. For the DAM sample at $\varepsilon_0 = 0.5\%$, TTS is not valid and, thus, no master curve can be given.

Comparison of master curves. In Fig. 4.8 and 4.9, the obtained master curves are shown. Storage modulus and loss modulus are plotted on a double-logarithmic scale. Figure 4.8 depicts the master curves of the tests performed without humidity control. In terms of a linear viscoelastic behavior, the curves should be identical for different load levels. As the red and the blue curves are not identical, the dried samples show nonlinear behavior at a mean strain of $\varepsilon_0 = 0.3\%$. A load shift, analog to the temperature shift, cannot be applied as the curve shapes differ. On the red curve, the inflection point of the storage modulus and the maximum of the loss modulus is reached for a higher frequency. Furthermore,

[5] This subsection is based on the subsections *Master curve construction* and *Comparison of different master curves* in Kehrer et al. (2023).

Conditioning	ε_0 in %	f in Hz	θ in °C	θ_{ref} in °C
DAM	0.1	$0.5 - 18$	$20 - 130$	75
DAM	0.3	$0.5 - 18$	$20 - 130$	75
DAM	0.5	TTS invalid		
ATM	0.1	$0.5 - 10.8$	$0 - 95$	25
ATM	0.3	$0.5 - 10.8$	$0 - 95$	25
DAM, $\Phi = 20\%\mathrm{RH}$	0.1	$0.5 - 19.9$	$10 - 70$	60
ATM, $\Phi = 50\%\mathrm{RH}$	0.1	$0.5 - 19.9$	$10 - 70$	25

Table 4.2: Considered temperature and frequency ranges for the master curve construction, cf. Table 7 in Kehrer et al. (2023).

the loss modulus is not symmetric as it decreases less strongly after its maximum is reached. Additionally, the horizontal shift factors for the higher load are larger resulting in a broader frequency range. For the conditioned samples, nonlinear behavior cannot be detected as the master curves are in good agreement. The master curves for the tests performed with humidity control are shown in Fig. 4.9. A common master curve is provided. In this case, the humidity influence can be modeled by a humidity-dependent glass transition temperature. If, instead, the same reference temperature is chosen for both master curves, a humidity shift can be seen. The master curves for the tests without humidity control in Fig. 4.8 indicate more complex nonlinear behavior. Only the loss modulus shows a common master curve between 10^{-1} Hz and 10^{6} Hz. Therefore, the influence of moisture content cannot be modeled by a shift in this case. In Fig. 4.10, the master curves for tests of ATM23/50 conditioned samples with and without humidity control are compared. The curves are in good agreement. In contrast to, e.g., relaxation tests, the influence of a missing climate control is not as pronounced. Consequently, changes in mechanical properties due to diffusion do not happen at the measurement

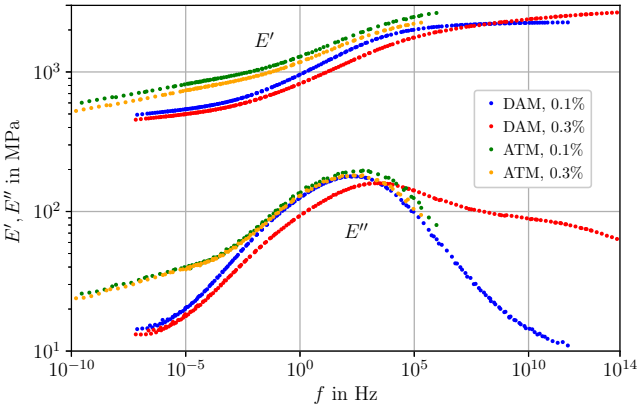

Figure 4.8: Resulting master curves for temperature-frequency tests performed without humidity control. The conditioning state of the sample (DAM vs. ATM23/50) and the load level ($\varepsilon_0 \in \{0.1\%, 0.3\%\}$) are varied. This plot is taken from Figure 8 in Kehrer et al. (2023).

temperatures ($10 - 70°\mathrm{C}$) within the time scale of the experiment.[6] In general, the master curves agree well with the asymptotic properties given by Eq. (4.13) and (4.14). With increasing moisture content, not all of these properties are evident. The reason is that the corresponding master curves are cut off at some point as the considered temperature range is limited. In all curves, the loss modulus shows a pronounced maximum at medium frequencies.

[6] In relaxation tests, the time scale can be larger than in temperature-frequency tests. Thus, in this case, the influence of changing water content can be significant, cf. Kehrer et al. (2023) and Dyck et al. (2024).

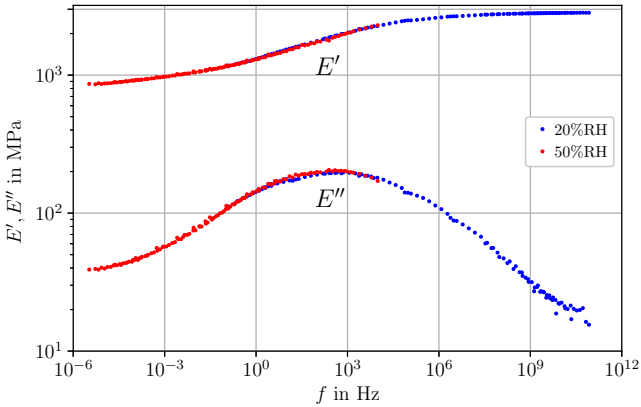

Figure 4.9: Resulting master curves for temperature-frequency tests performed under humidity control. DAM samples were tested at 20%RH and ATM23/50 conditioned samples at 50%RH, both at $\varepsilon_0 = 0.1\%$. This plot is taken from Figure 9 in Kehrer et al. (2023).

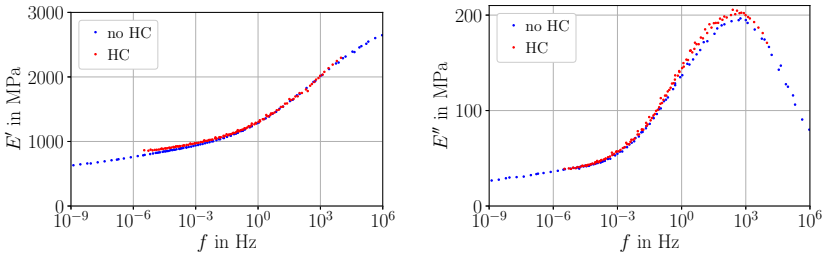

(a) Storage modulus **(b)** Loss modulus

Figure 4.10: Comparison of master curves resulting from temperature-frequency tests performed with and without humidity control (HC). ATM23/50 conditioned samples were tested at $\varepsilon_0 = 0.1\%$. These plots are taken from Figure 10 in Kehrer et al. (2023).

4.4.4 GMM parameter identification[7]

Based on the determined horizontal and vertical shifts, the temperature-dependencies of the relaxation times and stiffnesses are known. Stiffnesses and relaxation times themselves are still to be determined. The discussed master curves can be used as input for a parameter identification. As an example, the parameter identification is discussed for the tests with DAM samples since these tests cover all asymptotic properties in Eq. (4.13) and (4.14). The relaxation times are prescribed in a logarithmic distribution. First, the load case with $\varepsilon_0 = 0.1\%$ is considered. The largest relaxation time is set to the inverse of the minimum frequency decade, $\tau_\mathrm{N} = 10^7$ s. Vice versa, the smallest relaxation time, τ_1, is set to 10^{-12} s. For the stiffnesses, lower and upper bounds are defined: The lower bound is set to zero to avoid negative stiffnesses, the upper bound is set to 2500 MPa which is nearly the maximum storage modulus. Furthermore, the start value for the optimization is also set to zero. The influence of the number of Maxwell elements and of the weighting factors is investigated. In Fig. 4.11 - 4.13, results are shown for various parameters. The black points depict the master curves that serve as input whilst the blue and red curves show the behavior predicted by the parameter fit. By increasing the number of Maxwell elements, the fit becomes more precise and smooth, see Fig. 4.11 and 4.13a. Each Maxwell element causes an inflection point in the storage modulus and a local maximum in the loss modulus. The respective positions are defined by the inverse of the corresponding relaxation time. If the number of relaxation times increases, these local inflection points and maxima are blurred. By using 20 elements, a good fit is already obtained. Thus, the rule of thumb that at least one Maxwell element per frequency decade should be used is confirmed (Ghobadi et al., 2015; Göhler, 2011). For 30 Maxwell elements, only the global inflection point and the global maximum can be seen in Fig. 4.13a. At large frequencies, the storage

[7] This subsection is based on the subsection *Parameter identification* in Kehrer et al. (2023).

modulus is slightly overestimated. The maximum of the loss modulus is slightly underestimated. In Fig. 4.12a, only the storage modulus is considered for the parameter identification, $a'' = 0$. Consequently, E' is perfectly fitted. However, E'' is poorly fitted for low frequencies and slightly underestimated in the frequency range of 10^{-1} to 10^{12} Hz. In contrast, the results for choosing only the loss modulus as input of the parameter identification, $a' = 0$, are depicted in Figure 4.12b. In this case, the loss modulus is perfectly fitted. For the storage modulus, an offset can be seen. The reason is that the loss modulus does not depend on the equilibrium stiffness E_0, see Eq. (4.12). Thus, the start value of E_0 does not change during the optimization. The offset can be minimized by choosing an appropriate start value. To conclude, both storage and loss modulus should be used as input parameters for the parameter identification. Using $a' = a'' = 0.5$ is a reasonable approach. Figure 4.14 shows the corresponding stiffnesses and relaxation times for the parameter fits of Fig. 4.11a, 4.11b and 4.13a. The solid lines visualize the respective values of the equilibrium stiffness. As E_0 is the lower bound of the storage modulus, the value of E_0 does not change significantly by increasing the number of Maxwell elements. The stiffnesses of the Maxwell elements decrease by increasing the number of Maxwell elements. The maximum of these stiffnesses coincides with the inflection point of E' and the maximum of E'' at medium relaxation times. In Fig. 4.13b, the parameter fit for $\varepsilon_0 = 0.3\%$ is shown. Compared to Figure 4.13a, the storage modulus is more overestimated at high frequencies. The reason may be the asymmetric behavior of the loss modulus. To capture this, the stiffnesses at the corresponding relaxation times are larger. This leads to an overestimation of the storage modulus. Espacially for larger frequencies, the GMM cannot capture this behavior accurately. The identified GMM parameters regarding Fig. 4.13 are given in Tab. B.1.

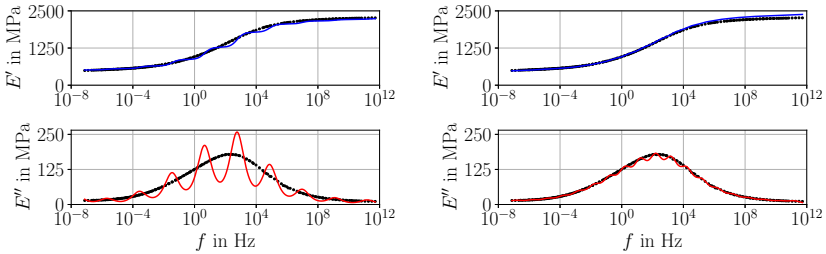

(a) 10 Maxwell elements **(b)** 20 Maxwell elements

Figure 4.11: GMM fit of the master curves for the DAM sample tested at $\varepsilon_0 = 0.1\%$. Storage and loss modulus are weighted equally, $a' = 50\%, a'' = 50\%$, the number of Maxwell elements is varied. The solid lines depict the result of the fit. These plots are taken from Figure 11 in Kehrer et al. (2023).

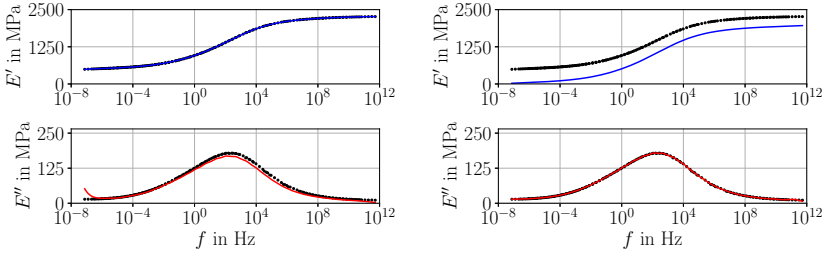

(a) $a' = 100\%, a'' = 0\%$ **(b)** $a' = 0\%, a'' = 100\%$

Figure 4.12: GMM fit of the master curves for the DAM sample tested at $\varepsilon_0 = 0.1\%$. The number of Maxwell elements is 30. The weighting factors of storage and loss modulus are varied. The solid lines depict the result of the fit. These plots are taken from Figure 11 in Kehrer et al. (2023).

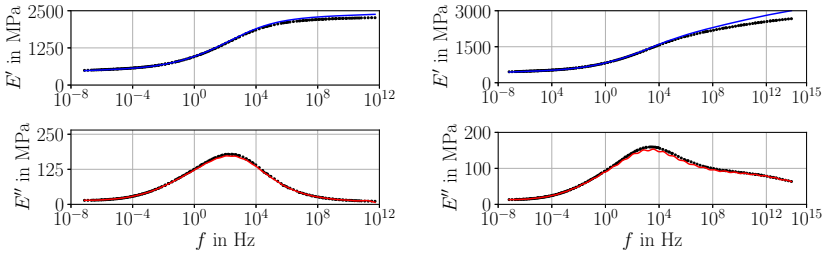

(a) $\varepsilon_0 = 0.1\%$ **(b)** $\varepsilon_0 = 0.3\%$

Figure 4.13: GMM fit of the master curves for the DAM sample tested at two different load levels. Storage and loss modulus are weighted equally, $a' = 50\%, a'' = 50\%$. 30 Maxwell elements are used. These plots are taken from Figure 11 and Figure 13 in Kehrer et al. (2023).

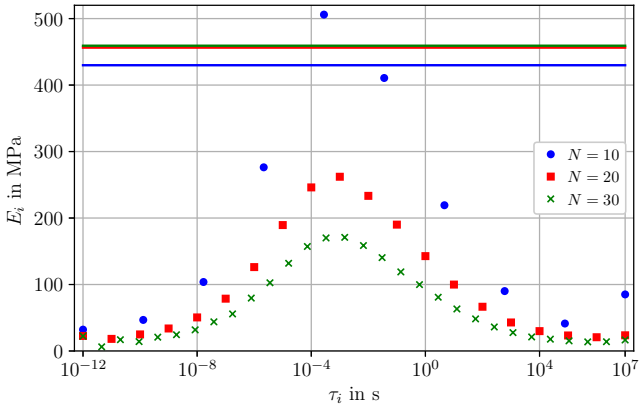

Figure 4.14: Plot of the identified GMM parameters from Fig. 4.11a, 4.11b and 4.13a, where the number of Maxwell elements varies. The solid lines represent the value of E_0. The dots depict the relaxation times and the corresponding stiffnesses. This plot is taken from Figure 12 in Kehrer et al. (2023).

4.5 Summary of results

In this chapter, the temperature-dependent viscoelastic part of the model in Ch. 3 has been applied. Therefore, the viscoelastic behaviour of PA6 under hydrothermal influences in cyclic DMA experiments was considered. First, master curves for storage and loss modulus, and the loss factor were constructed by applying extended TTS including horizontal and vertical shifts. It was shown that the extended TTS is only applicable in a limited range of frequencies, temperatures and strain loads. When considering differently conditioned samples, a moisture-dependent glass transition temperature can be observed. By the master curves, it was shown that the influence of moisture can be modeled by using the respective glass transition temperature as the reference temperature. For DAM samples, onsetting nonlinearity regarding the strain load could be observed at a mean strain of 0.3%. In contrast, for the ATM23/50 conditioned samples, this was not the case. Furthermore, the comparison of master curves obtained by tests with and without humidity control showed that the influence of drying effects is neglectable for the time scale of temperature-frequency tests. Last, the parameter identification for a GMM was discussed using the master curves of the DAM samples as an example. The temperature-dependencies of the GMM are given by the horizontal and vertical shift factors. Relaxation times were prescribed and stiffnesses were determined by least-squares optimization. It was shown that the residual within the optimization should consider both storage and loss modulus. Furthermore, at least one Maxwell element should be used per considered frequency decade which confirms findings from the literature.

Chapter 5

Entropy relaxation in polystyrene[1]

5.1 Introduction

In this chapter, the caloric part of the thermoviscoelastic models described in Ch. 3 is discussed in detail. It is shown how the model is able to predict viscocaloric behavior in the vicinity of the glass transition. The model is related to the kinetic theory of the glass transition. Representatively, the model is adjusted to experimental DSC measurements of the heat capacity of PS. The behavior during heating and cooling at two different temperature rates is considered. First, the model equations are derived and summarized in Sec. 5.2. The adjustment of the model parameters based on experimental measurements and a discusion on the model is given in Sec. 5.3 and 5.4.

[1] The findings of this chapter are further developed and published in Keursten et al. (2025) (note added in proof)

5.2 Viscocaloric model

5.2.1 Governing equations

The first-order viscocaloric model introduced in Sec. 3.2 is used. Thermoviscoelastic effects on the caloric behavior due to viscous thermal expansion behavior are neglected. With Eq. (3.5), the free enthalpy, the entropy and the enthalpy are given by

$$g = \varphi(\theta) + \frac{C}{2}(\theta - \theta_\mathrm{v}), \tag{5.1}$$

$$s = -\frac{\partial g}{\partial \theta} = -\varphi'(\theta) - C(\theta - \theta_\mathrm{v}), \tag{5.2}$$

$$h = g + s\theta = \underbrace{\varphi(\theta) - \theta\varphi'(\theta)}_{\int c_p^\mathrm{eq}(\theta)\,\mathrm{d}\theta} + \frac{C}{2}(\theta - \theta_\mathrm{v})^2 - C\theta(\theta - \theta_\mathrm{v}). \tag{5.3}$$

Due to the purely caloric model, free energy and free enthalpy are identical. The same holds for enthalpy and internal energy. The expression for the free energy is based on the works by Lion et al. (2017) and Mittermeier (2017). In the referenced works, the internal temperature is introduced as a relative quantity, comparable to viscous strains. This means that the internal temperature is a dimensionless variable that is zero at an arbitrarily selectable reference temperature if the material is in equilibrium. In this work, the internal temperature θ_v is an absolute temperature like quantity. This makes the physical meaning of the internal variable clearer as θ_v corresponds to the physical temperature at which the current material state would be the equilibrium state. The internal temperature is equivalent to the fictive temperature introduced by Tool (1945). For all thermodynamic potentials and for the entropy, a decomposition into an equilibrium and a viscocaloric non-equilibrium part is given. The equlibrium parts are basically described by the temperature-dependent function $\varphi(\theta)$ that is related with the equilibrium heat capacity via Eq. (3.6).

The viscocaloric parts contain the internal temperature to account for process-dependent behavior. The evolution equation (3.14) is specified to

$$\dot{\theta}_{\mathrm{v}} = \frac{\theta - \theta_{\mathrm{v}}}{\lambda(\theta, \dot{\theta})}, \quad \theta_{\mathrm{v}}(t=0) = \theta_{\mathrm{v0}}, \tag{5.4}$$

with the initial value θ_{v0}. In contrast to models known from literature, e.g., TNM model or KAHR model, this model does not account for a relaxation time that depends on the internal variable itself. As phenomenological approach, in this work, it is assumed that the relaxation time λ depends explicitely on the temperature and its rate in form of

$$\lambda(\theta, \dot{\theta}) = a_\theta(\theta) d(\dot{\theta}) \lambda_{\mathrm{ref}}. \tag{5.5}$$

Thus, the dependencies on temperature and temperature rate are seperated multiplicatively. The rate-dependent factor d is introduced to account for a rate-dependency that goes beyond the inherent rate-dependency of the relaxation equation. For a constant rate, time-temperature superposition holds. The WLF equation (3.51) is used to model the temperature-dependent shift function a_θ, cf. Lion et al. (2017). The reference temperature of the WLF equation, θ_{ref}, is set to the approximated glass transition temperature θ_{g}. With that, two limiting cases can be identified. First, for $\theta \gg \theta_{\mathrm{g}}$, the relaxation time is very small which means that equilibrium behavior is observed at this temperatures, $\theta_{\mathrm{v}} = \theta$. In this case, the non-equilibrium parts in Eq. (5.1) - (5.3) are vanishing. Second, for $\theta \ll \theta_{\mathrm{g}}$, the relaxation time is very large which means that the evolution of the internal temperature is frozen, $\dot{\theta}_{\mathrm{v}} = 0$. This state is refered to as glassy state. In both, the equilibrium and the glassy state, the model behavior is process-independent. Thus, it is evident that the temperature-dependency of the relaxation time is crucial for modeling of the glass transition.

5.2.2 Heat capacity

The isobaric heat capacity is the central property when describing the caloric behavior of solids. Thus, the pressure is prescribed for the considered processes and the free enthalpy arises as natural potential. In the following, the isobaric heat capacity for the viscocaloric model is derived. Replacing the internal energy by the enthalpy via Legendre transformation in Eq. (2.42) and assuming vanishing heat sources and isobaric conditions gives

$$\varrho \dot{h} = -\mathrm{div}\left(\boldsymbol{q}\right), \tag{5.6}$$

see Lion and Johlitz (2016). A process is considered where the heat ΔQ is transfered to a body with mass m within the time increment Δt. The enthalpy balance in Eq. (5.6) is integrated over the volume, giving

$$m\dot{h} = \int_V \varrho \dot{h}\,\mathrm{d}V = -\int_V \mathrm{div}\left(\boldsymbol{q}\right) = \dot{Q} \approx \frac{\Delta Q}{\Delta t}. \tag{5.7}$$

It is assumed that the heat power $\dot{Q}$ is constant. Under isobaric conditions, the heat ΔQ related to a temperature change $\Delta\theta$ is given by

$$\Delta Q = c_p m \Delta\theta. \tag{5.8}$$

With that and the assumption of a constant temperature rate, the isobaric heat capacity c_p is defined as

$$c_p = \left.\frac{\dot{h}}{\dot{\theta}}\right|_{p=\mathrm{const}}, \quad \dot{\theta} = \Delta\theta/\Delta t \tag{5.9}$$

(Lion and Johlitz, 2016). Evaluating Eq. (5.9) for the viscocaloric model under consideration of Eq. (5.3) gives the process-dependent (apparent)

heat capacity

$$c_p = \underbrace{c_p^{\mathrm{eq}} - C\theta}_{c_p^{\mathrm{gl}}} + C\frac{\theta_{\mathrm{v}}\dot{\theta}_{\mathrm{v}}}{\dot{\theta}}. \tag{5.10}$$

The heat capacity in the glassy state ($\dot{\theta}_{\mathrm{v}} = 0$) is denoted by c_p^{gl}. With that, the physical meaning of the parameter C is evident. It is a measure for the change of the heat capacity within the glass transition. A further useful property is the reduced heat capacity

$$c_p^{\mathrm{red}} = \frac{c_p - c_p^{\mathrm{gl}}}{c_p^{\mathrm{eq}} - c_p^{\mathrm{gl}}} = \frac{\theta_{\mathrm{v}}\dot{\theta}_{\mathrm{v}}}{\theta\dot{\theta}}. \tag{5.11}$$

During the glass transition, the reduced heat capacity changes from $c_p^{\mathrm{red}} = 0$ in the glassy state to $c_p^{\mathrm{red}} = 1$ in the equilibrium state. If a generalized thermorheological model is superposed, there are further contributions to the heat capacity. These contributions of the GMM and GKM are given in App. A.3 but neglected in this chapter.

5.2.3 Initial value problem

To evaluate the heat capacity for a specific temperature process, the initial value problem in Eq. (5.4) must be solved. Therefore, suitable initial values must be selected. In this chapter, two load cases are considered: cooling and heating under constant temperature rates between $\theta_{\max} \gg \theta_{\mathrm{g}}$ and $\theta_{\min} \ll \theta_{\mathrm{g}}$. As stated before, above the glass transition, it can be assumed that the material is in equilibrium. If a process starts above the glass transition, the previous temperature history does not influence the current behavior as the material state is fastly resetted above the glass transition. Thus, for the cooling loads, the initial value can be set to the equilibrium value of the internal temperature, $\theta_{\mathrm{v}0} = \theta(t = 0)$. For a heating load, this is not valid as the process starts in a frozen state that depends on the temperature history. If an experimental data set with unknown previous

temperature history is given, however, the initial value can be calculated numerically. By reformulating Eq. (5.11) and applying the chain rule, the following relation arises

$$\frac{1}{2}\gamma := c_p^{\mathrm{red}}\theta\dot{\theta} = \theta_{\mathrm{v}}\dot{\theta}_{\mathrm{v}} = \frac{1}{2}\frac{\mathrm{d}\theta_{\mathrm{v}}^2}{\mathrm{d}t}. \tag{5.12}$$

The term $\theta\dot{\theta}$ is given by the considered temperature process. If the functions of the equilibrium and the glassy heat capacity are already known, c_p^{red} and γ can be directly calculated from the experimental data. Then, integration over the considered time interval yields

$$\Gamma := \int_0^T \gamma \,\mathrm{d}t = \theta_{\mathrm{v}}^2(t=T) - \theta_{\mathrm{v}}^2(t=0). \tag{5.13}$$

The integral must be solved numerically. If a heating process that ends above the glass transition is considered, the final value of the internal temperature can be set to its equilibrium value, $\theta_{\mathrm{v}}(T) = \theta_{\max}$. With that, the initial value for a heating simulation is given by

$$\theta_{\mathrm{v}0} = \sqrt{\theta_{\max}^2 - \Gamma}. \tag{5.14}$$

Due to the nonlinearity of the WLF equation, the ODE in Eq. (5.4) must be solved numerically if a non-constant temperature is considered. An implicit Runge-Kutta method implemented in the `Python` library `scipy` is used for all numerical simulations in this work. In post-processing, Eq. (5.10) and (5.11) are evaluated based on the numerical solution of the internal temperature. The rate of the internal temperature is approximated by a finite difference scheme.

5.3 Entropy relaxation

5.3.1 Experimental input

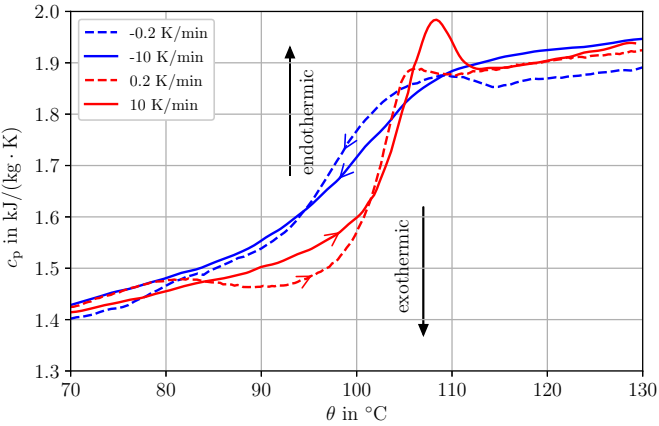

Figure 5.1: DSC measurements of the heat capacity of PS in the vicinity of the glass transition at 0.2 K/min and 10 K/min. The curves show montonic behavior during cooling (blue curves) and non-monotonic behavior during heating (red curves). The data at 10 K/min is extracted from Tropin et al. (2015), Figure 4.

In the following, the described viscocaloric model is applied in order to reproduce experimental measurements in the vicinity of the glass transition. As the model does not account for crystallization and semicrystallinity, amorphous PS is considered. A further advantage of PS is its low water absorption capacity. This means that, in contrast to PA, the influence of humidity can be neglected. The DSC measurements that are used as input for a parameter identification are shown in Fig. 5.1. The isobaric heat capacity is plotted over the temperature for cooling and

heating with constant temperature rates of $0.2\ \mathrm{K/min}$[2] and $10\ \mathrm{K/min}$[3]. In general, the value of the heat capacity changes significantly during the glass transition. Furthermore, the slope of the temperature-dependent heat capacity in the equilibrium state is smaller than in the glassy state. During cooling, the heat capacity decreases montonically. The slight kink of the dashed curve between $110°\mathrm{C}$ and $115°\mathrm{C}$ is assumed to be a measuring error. In case of cooling, the inflection point of the curve defines the glass transition temperature (Hess et al., 2013). Thus, it can be seen that the glass transition is shifted to higher temperatures for an increasing temperature rate. During heating, a non-monotonic behavior of the heat capacity is observed. This behavior is known as enthalpy relaxation in literature. However, as motivated in Sec. 3.2.2, the term entropy relaxation is used here. For both rates, a pronounced local maximum is observed which is related to endothermic effects. In case of the smaller temperature rate, furthermore, a local minimum related to exothermic behavior can be seen. In general, the curves show good agreement in the glassy state at low temperatures and in the equilibrium state at high temperatures. Thus, in these temperature ranges, the material behaves process-independent. Furthermore, it can be concluded that the samples used are comparable to each other.

5.3.2 Parameter identification

Glassy and equilibrium state. As first step of the parameter identification, the behavior of the heat capacity in the glassy and equilibrium state is considered. The following approach for the equilibrium heat capacity is used

$$c_p^{\mathrm{eq}}(\theta) = \frac{m_1 + m_2}{2}\theta - \frac{m_1 - m_2}{2\zeta} \ln\left(\frac{\cosh(\zeta(\theta - \theta_{\mathrm{T}}))}{\cosh(\zeta\theta_{\mathrm{T}})}\right) + c_0. \tag{5.15}$$

[2] Data provided by Michael Fischlschweiger, TU Clausthal (2023).
[3] Data extracted from Tropin et al. (2015).

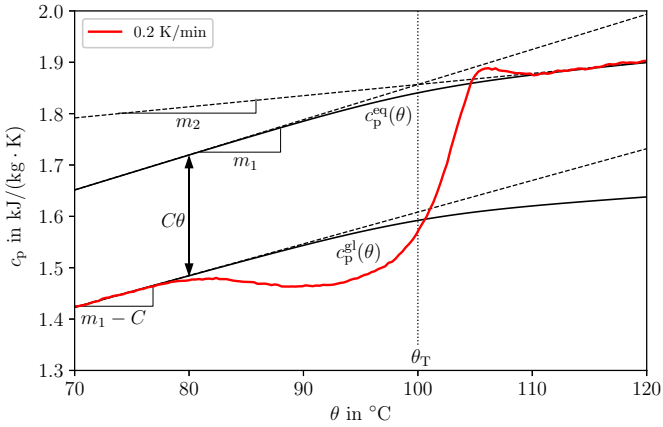

Figure 5.2: Representative construction of the glassy and equilibrium heat capacity. The transition temperature θ_T is specified as an asumption. The parameters m_1, m_2, c_0 and C are determined by the construction where c_0 is not shown here for clarity.

This approach is taken from Lion et al. (2017) and extended by the constant c_0. Due to c_0, the heat capacity does not approach zero for $\theta \to 0\,\mathrm{K}$. However, the model is not supposed to be applied far away from the considered temperature interval between $70°\mathrm{C}$ and $130°\mathrm{C}$. The glassy heat capacity is given by

$$c_p^\mathrm{gl}(\theta) = c_p^\mathrm{eq}(\theta) - C\theta. \tag{5.16}$$

Then, the following approximations are valid

$$\theta \ll \theta_\mathrm{T}: \quad c_p^\mathrm{eq} = m_1\theta + c_0, \quad c_p^\mathrm{gl} = \underbrace{(m_1 - C)}_{m_\mathrm{gl}}\theta + c_0^\mathrm{gl}, \tag{5.17}$$

$$\theta \gg \theta_\mathrm{T}: \quad c_p^\mathrm{eq} = m_2\theta + \underbrace{(m_1 - m_2)\theta_\mathrm{T} + c_0}_{c_0^\mathrm{eq}}. \tag{5.18}$$

For both limiting cases, Eq. (5.15) simplifies to a linear function. Note that the approximation for the equilibrium heat capacity in the glassy state is only of theoretical interest as the equilibrium state cannot be reached within finite times for low temperatures. The parameter ζ determines the width of the smooth transition between those linear functions at θ_T and is set to 0.1 (Lion et al., 2017). The transition temperature θ_T is set to $100°\mathrm{C}$ which is a rough approximation of the glass transition temperature of PS. Then, the parameters m_1, m_2, c_0 and C are determined by the construction representatively shown in Fig. 5.2. A linear approximation of the behavior in the glassy and the equilibrium state yields the slopes and the axis intercepts $m_\mathrm{gl}, m_2, c_0^\mathrm{gl}$ and c_0^eq. As $C\theta$ is the difference of the equations in (5.17), $c_0 = c_0^\mathrm{gl}$ holds. Last, by demanding that the linear curves with the slopes m_1 and m_2 intersect at θ_T, the parameters C and m_1 are given by

$$C = \frac{c_0^\mathrm{eq} - c_0^\mathrm{gl}}{\theta_\mathrm{T}} + m_2 - m_\mathrm{gl}, \quad m_1 = m_\mathrm{gl} + C. \tag{5.19}$$

The identified parameters for all four curves in Fig. 5.1 are given in Tab. 5.1. Note that the equilibrium behavior of the cooling curve at $0.2\ \mathrm{K/min}$ is approximated by the respective heating curve due to the suspected measuring error. With that, the curve can be continued monotonically. As the considered temperature range starts at about $340\ \mathrm{K}$, the slopes and the axis intercepts vary significantly although the resulting curves match well in the considered temperature range.

Glass transition regime. For the consideration of the glass transition regime, the reduced heat capacity of the experimental data, see Eq. (5.11), is evaluated by the before determined glassy and equilibrium heat capacities. With that, the temperature-dependency of the heat capacity in the glassy and equilibrium state is filtered out (Tropin et al., 2015). In literature, the WLF parameters are often set to $c_1 = 17.4$ and $c_2 = 51.6\ \mathrm{K}$ if the glass transition temperature is chosen as reference temperature. However,

$\dot{\theta}$ in $\mathrm{K/min}$	C in $\mathrm{J/(kgK^2)}$	c_0 in $\mathrm{J/(kgK)}$	m_1 in $\mathrm{J/(kgK^2)}$	m_2 in $\mathrm{J/(kgK^2)}$
0.2	0.67	-696	6.84	2.17
-0.2	0.69	-1012	7.69	2.17
10	0.84	0	4.96	2.67
-10	0.79	-372	6.04	2.17
$\theta_\mathrm{T} = 373.15\ \mathrm{K}, \quad \zeta = 0.1$				

Table 5.1: Identified parameters that define the glassy and equilibrium heat capacity for all considered curves.

$\lvert\dot{\theta}\rvert$ in $\mathrm{K/min}$	c_1 $-$	c_2 in K	θ_ref in K	λ_ref in s
0.2	11.7	51.6	373.15	1200
10	11.7	51.6	373.15	45

Table 5.2: Identified WLF parameters and relaxation times for the considered temperature rates

in the case considered here, this will lead to a smaller glass transition interval than observed in experiments. By reducing c_1 or by increasing c_2, the glass transition interval becomes broader as the WLF curve becomes flatter. For the parameter identification, c_1 is adjusted whilst c_2 is fixed. Furthermore, the reference relaxation time λ_ref must be determined. To start, the temperature rate of $0.2\ \mathrm{K/min}$ is considered. The parameters are determined based on the heating curve. By global least squares optimization regarding the reduced heat capacity, the parameters c_1 and λ_ref are identified and documented in Tab. 5.2. With the adjusted parameters, a simulation of the cooling process is conducted. The comparison of simulation and experimental results is shown in Fig. 5.3 for both the reduced heat capacity and the total heat capacity. It can be seen that the temperature interval of the glass transition is reproduced well for heating and cooling. The exothermic minimum and the endothermic maximum during heating are overestimated. However, the qualitative behavior is

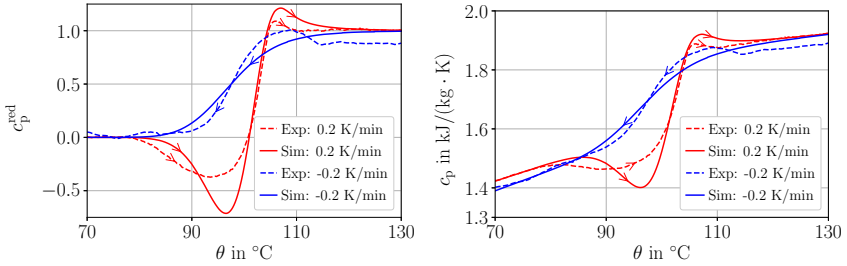

(a) Reduced heat capacity

(b) Total heat capacity

Figure 5.3: Comparison of experimental results and simulation for a temperature rate of $0.2\ \mathrm{K/min}$. The initial value for the heating simulation is $\theta_{v0} = 380.2\ \mathrm{K}$.

still fitted well. Next, the temperature rate of $10\ \mathrm{K/min}$ is considered. Due to the multiplicative seperation of temperature-dependency and rate-dependency in Eq. (5.5), the previously determined WLF parameters are adopted. The relaxation time is adjusted so that the temperature interval of the glass transition is reproduced, see Tab. 5.2. In Fig. 5.4, the comparison of simulation and experimental results is shown. For the cooling simulation, the results match well with the respective experimental data. The endothermic maximum of the heating curve is also fitted well. However, the simulation predicts a slight exothermic minimum that cannot be seen in the experimental curve. This corresponds with the overestimation of the exothermic minimum at $0.2\ \mathrm{K/min}$.

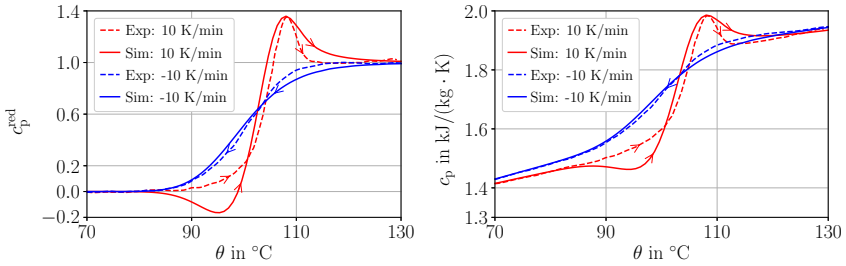

(a) Reduced heat capacity

(b) Total heat capacity

Figure 5.4: Comparison of experimental results and simulation for a temperature rate of 10 K/min. The initial value for the heating simulation is $\theta_{v0} = 373.3$ K.

5.3.3 Discussion of entropy relaxation

In the following, the behavior during the glass transition is explained in more detail from a model perspective. Figure 5.5 illustrates the behavior of the reduced heat capacity and the internal temperature for a representative simulation of cooling. The simulation starts in the equilibrium state where the internal temperature is identical to the physical temperature. With decreasing temperature, the relaxation time increases monotonically due to the WLF equation. Thus, the rate of the internal temperature decreases monotonically and the internal temperature starts to deviate from the equilibrium state. At low temperatures, the rate of the internal temperature is nearly vanishing and a frozen state is approached, the glassy state. Due to the monotonic behavior of the internal temperature, the heat capacity also decreases monotonically. If the cooling rate is increased, the internal temperature deviates more quickly from its equilibrium solution. Thus, the glass transition is shifted to higher temperatures. A representative heating simulation is depicted by Fig. 5.6. The simulation starts in the frozen state with the specified initial value of the internal temperature. Due to the temperature increase, the relaxation time decreases and the internal temperature begins to approach its equilibrium value. As the internal

temperature is still greater than the equilibrium solution at this point, the rate of the internal temperature is negative. This explains the undershoot in the heat capacity. As the relaxation time is not yet small enough, the internal temperature falls below the equilibrium solution, reaches a minimum and approaches the equilibrium solution again with decreasing relaxation time. Because the equilibrium solution is approached from below, the rate in this temperature interval is greater than the temperature rate. This leads to an overshoot in the heat capacity. How pronounced the undershoot and overshoot are, is determined by the initial value of the internal temperature and the heating rate. In Fig. 5.7, the influence of the initial value is depicted. The lower the initial value, the closer is the internal temperature to its equilibrium solution at the beginning. Thus, the undershoot becomes smaller. Furthermore, the intersection with the equilibrium solution is shifted to lower temperatures which then increases the overshoot. For very small initial values, the undershoot can vanish whilst the overshoot can vanish for very large initial values. In general, the non-monotonic behavior during heating is related with a relaxation to the equilibrium state. If the internal temperature approaches its equilibrium value, the non-equilibrium terms of the enthalpy and entropy are relaxing to zero, cf. Eq. (5.3). Thus, the terms enthalpy and entropy relaxation are motivated.

5.3.4 Glass transition temperature

In literature, a specific glass transition temperature is often indicated although the glass transition is observed in a temperature interval. The determination of a glass transition temperature is shortly discussed here. For the cooling curves, the definition of a glass transition temperature is unambigous. The behavior of the internal temperature in Fig. 5.5 is comparable to the behavior of the thermal strain in dilatometry, see, e.g, Simon et al. (2001) or Sanditov and Ojovan (2017). Thus, the glass transition temperature can be defined as the intersection point of the tangents

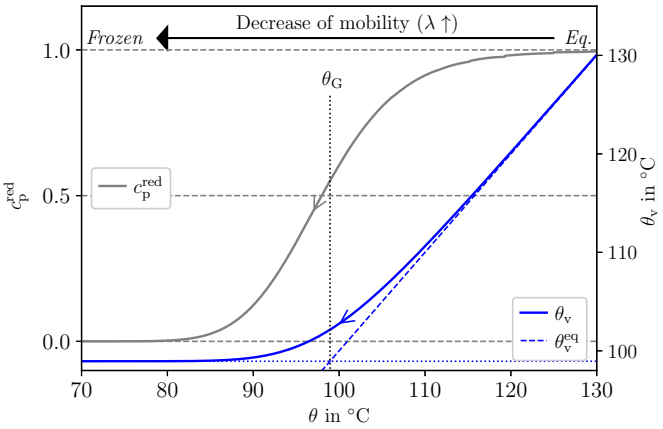

Figure 5.5: Behavior of the heat capacity and the internal temperature during cooling. A cooling rate of $\dot{\theta} = -2$ K/min is applied and the relaxation time set to $\lambda_{ref} = 137.4$ s.

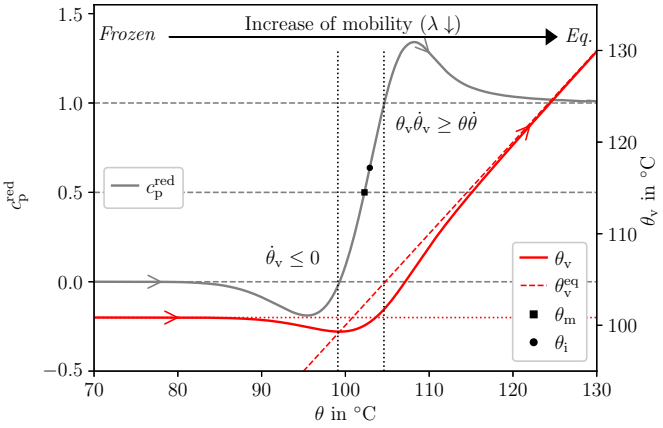

Figure 5.6: Behavior of the heat capacity and the internal temperature during heating. A heating rate of $\dot{\theta} = 10$ K/min is applied, the relaxation time and the initial value are set to $\lambda_{ref} = 45$ s and $\theta_{v0} = 374$ K.

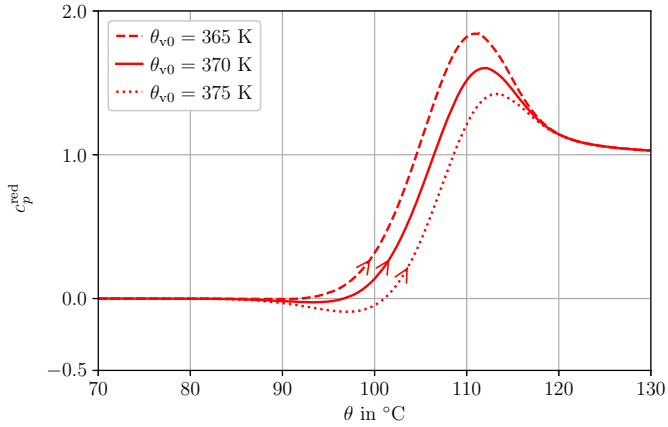

Figure 5.7: Varying initial value of the internal temperature. A heating rate of $\dot{\theta} = 10\ \mathrm{K/min}$ is applied and the relaxation time is set to $\lambda_{\mathrm{ref}} = 45$ s.

depicted in Fig. 5.5. As the equilibrium value of the internal temperature is identical to the physical temperature, the glass transition temperature is given by the final value of the internal temperature. The inflection point of the reduced heat capacity coincides with the glass transition temperature in this case. For the cooling simulations at $0.2\ \mathrm{K/min}$ and $10\ \mathrm{K/min}$, the glass transition temperatures are given by $98.3°\mathrm{C}$ and $101.1°\mathrm{C}$ respectively. Due to the non-monotonic behavior, the glass transition temperature is not unambiguous in the case of heating processes. Possible definitions of the glass transition temperature are summarized in the standard ASTM E1356-23 (2023). Two of these defintions are shown in Fig. 5.6. The inflection temperature θ_{i} is defined by the inflection point of the heat capacity. However, in this case, the inflection point does not coincide with the intersection point of the tangents. Thus, the determination of the inflection point is more complex and needs a numerical procedure. Furthermore, for the inflection point during heating, $c_p^{\mathrm{red}} \in \{0, 1\}$ does not

necessarily hold. Therefore, the midpoint temperature θ_{m}, defined as the temperature where $c_p^{\mathrm{red}} = 0.5$ holds, seems more reasonable. The heating simulations at $0.2\ \mathrm{K/min}$ and $10\ \mathrm{K/min}$ yield midpoint temperatures of $102.1°\mathrm{C}$ and $102°\mathrm{C}$, respectively. Note that the glass transition temperature during heating does depend on heating rate and the previous temperature history. Thus, the glass transition temperature is not necessarily higher for faster heating processes if samples with different temperature histories are compared.

5.4 Rate-dependent relaxation time

The fitted relaxation times for the two temperature rates deviate from each other by an order of magnitude. Thus, without considering a rate-dependent relaxation time, the rate-dependency of the glass transition is significantly overestimated by the model. Therefore, the function $d(\dot{\theta})$ is introduced in Eq. (5.5). If $d(\dot{\theta}) > 0$ holds, the dissipation inequality is still satisfied. As the relaxation time was adjusted for two temperature rates, the question arises how to interpolate the relaxation time between those points. In general, an increase of the cooling rate shifts the glass transition temperature to higher temperatures. By a linear interpolation of the relaxation time, this characteristic is not guaranteed. Instead, the rate-dependent relaxation time is interpolated by assuming that the glass transition temperature changes linearily in the considered cooling rate interval. This assumption is made as the glass transition temperature only changes by approximately $3°\mathrm{C}$ between both cooling rates. However, if a broader range of temperature rates is considered, the assumption should be reconsidered based on further experimental data. In the following, cooling processes are considered as the glass transition temperature is well-defined by the final value of the internal temperature in this case. For a specific temperature rate $\dot{\theta}$ between $\dot{\theta}_1 = 0.2\ \mathrm{K/min}$ and $\dot{\theta}_2 = 10\ \mathrm{K/min}$, the interpolated glass transition temperature θ_{gi} can be calculated based

on the values determined in the previous section,

$$\theta_{\mathrm{gi}}(\dot{\theta}) = \theta_{\mathrm{g}}(\dot{\theta}_1) + \frac{\dot{\theta} - \dot{\theta}_1}{\dot{\theta}_2 - \dot{\theta}_1}(\theta_{\mathrm{g}}(\dot{\theta}_2) - \theta_{\mathrm{g}}(\dot{\theta}_1)). \tag{5.20}$$

The required relaxation time λ_{ref} is then given by the root of

$$f(\lambda_{\mathrm{ref}}) = \theta_{\mathrm{gi}}(\dot{\theta}) - \theta_{\mathrm{v,end}}(\lambda_{\mathrm{ref}}, \dot{\theta}), \tag{5.21}$$

which must be solved numerically, e.g., by a bisection method. Within each iteration of the numerical scheme, a cooling process is simulated with the final value of the internal temperature $\theta_{\mathrm{v,end}}$ being the predicted glass transition temperature. As the glass transition temperature is shifted to higher temperatures for an increasing relaxation time and a constant cooling rate, a unique solution of Eq. (5.21) does exist. This procedure is applied for a logarithmic distribution of temperature rates with the resulting relaxation times being depicted in Fig. 5.8a by the black dots. The power law function

$$d(\dot{\theta}) = d_1 + d_2 \left(\frac{|\dot{\theta}|}{\dot{\theta}_0} \right)^{-k}, \quad \dot{\theta}_0 = 1\ \mathrm{K/s} \tag{5.22}$$

is used to analytically describe the rate-dependency of the relaxation time. No distinction is made between cooling and heating with the same temperature rate. By introducing the temperature rate $\dot{\theta}_0$, the constant d_2 becomes dimensionless. The power law should satisfy the conditions

$$d(\dot{\theta}_1) = 1, \quad d(\dot{\theta}_2) = \frac{\lambda_{\mathrm{ref}}(\dot{\theta}_2)}{\lambda_{\mathrm{ref}}(\dot{\theta}_1)}, \tag{5.23}$$

d_1	d_2	k
0.01862737	0.00308945	1.010025

Table 5.3: Parameters of the power law function to model $d(\dot{\theta})$

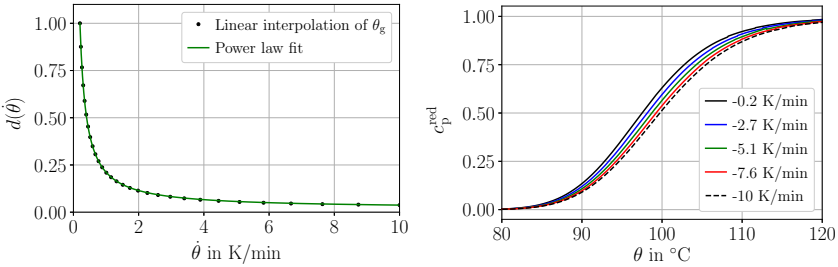

(a) Behavior of the function $d(\dot{\theta})$ if a linear interpolation of θ_g is applied.

(b) Resulting curves of the reduced heat capacity for varying cooling rates.

Figure 5.8: Rate-dependent relaxation time

where $\dot{\theta}_1$ is defined as the reference temperature rate. With these conditions, the coefficients of the power law function are given by

$$d_1 = 1 - d_2|\dot{\theta}_1|^{-k}, \quad d_2 = \frac{\frac{\lambda_{\mathrm{ref}}(\dot{\theta}_2)}{\lambda_{\mathrm{ref}}(\dot{\theta}_1)} - 1}{|\dot{\theta}_2|^{-k} - |\dot{\theta}_1|^{-k}}. \tag{5.24}$$

By curve fitting, the exponent k can then be determined. The result, depicted by the green curve in Fig. 5.8a, matches well. In Tab. 5.3, the determined parameters for the power law function are summarized. The prediction of the reduced heat capacity for varying cooling rate is shown in Fig. 5.8b.

5.5 Summary of results

In this chapter, the first order viscocaloric model described in Sec. 3.2 was discussed in more detail. It was shown how viscocaloric behavior within glass transition regime can be simulated using the internal temperature as an internal variable. For the relaxation time of the evolution of the internal temperature, a temperature dependency through the WLF equation and a rate dependence were assumed in a phenomenological approach. Then, the model was applied in order to reproduce DSC measurements of PS. The behavior of the heat capacity during heating and cooling was considered at two temperature rates. During heating, entropy relaxation with endothermic overshoots and exothermic undershoots was observed. In the first step of parameter identification, the process-independent behavior in the glassy and equilibrium state could be approximated by linear temperature-dependent functions. An analytical function from literature, that gives a smooth transition between the two limiting cases, was extended by an axis intercept. For the subsequent consideration of the glass transition regime, the reduced heat capacity of the experimental data was calculated. This allowed to compute the initial values of the heating simulations by numerical integration although the previous temperature history of the material was unknown. The lower heating rate was used to determine suitable WLF parameters and the relaxation time. For the larger temperature rate, the relaxation time had to be adjusted. Cooling simulations and the respective DSC measurements match well. For the considered heating processes, glass transition interval and qualitative behavior were also predicted well. The overshoots and undershoots were overestimated. Last, a linear rate-dependent glass transition temperature was assumed for the interpolation of the relaxation time between the considered temperature rates. It was shown that the rate-dependency of the relaxation time can be represented by a power law under this assumption.

Chapter 6

Summary and conclusions

6.1 Conclusion

In this work, the theory of linear thermoviscoelasticity was discussed, in particular for the thermomechanical modelling of thermoplastic polymers. This was followed by an application to two specific problems: Viscoelasticity of PA6 under hydrothermal influences and entropy relaxation of PS in the vicinity of the glass transition. In both cases, real experimental data served as input. The summary and conclusion of the individual sections is given below. At the end, a brief outlook is given.

Theory of thermoviscoelasticity. The models were derived by the Coleman-Noll procedure and linear irreversible thermodynamics to describe the dissipative processes. Viscoelasticity including thermal expansion and caloric behaviour were considered. For simplicity, the mechanical behavior was restricted to purely volumetric deformations. First, the simplest linear models were presented, first-order models. These are described by a single internal variable, the viscous strain or the internal temperature. The analogy between the mechanical and caloric model was emphasized. The structure of the free energy, consisting of a process-independent equilibrium part and a process-dependent, relaxing part, is identical. For the latter, a quadratic term, formulated in the deviation from equilibrium, was used. Due to the analogy, the term

viscocaloric behaviour was introduced for the process-dependent, caloric behaviour. Since the analogue quantity to the relaxing stress is a relaxing entropy, the term *entropy relaxation* was more appropriate than enthalpy relaxation in the context of this work. Furthermore, the generalization of the models was discussed, which allows for the superposition of several relaxation processes with different time constants. In particular, two model variants for viscoelastic behaviour, the GMM and GKM, including thermal expansion elements, were discussed. The models differ in their natural state variables, strain or stress, respectively. Thus, the GMM is the natural model for strain-driven processes and the GKM for stress-driven processes. In addition, the expression for the free enthalpy of the GKM was derived. By derivation of ordinary differential equations for GMM and GKM including thermal expansion elements, it was shwon that both models are equivalent. A conversion method was presented. Stiffnesses and viscosities can be converted using the method of Loy et al. (2015). Subsequently, a linear equation system must be solved for the conversion of the expansion coefficients.

Viscoelasticity of PA6. The viscoelastic behaviour of PA6 under uniaxial cyclic loading and hydrothermal influences was investigated. Temperature-frequency tests conducted by DMA served as input. Master curves of the viscoelastic properties were constructed by extended TTS using horizontal and vertical shifts. For this purpose, the arc length minimization method by Bae et al. (2011) was further developed by using normalization. Limitations regarding the temperature and frequency range, in which extended TTS can be applied, were identified. Based on the resulting master curves, the following conclusions could be drawn. For the measurements with dried samples, in contrast to measurements with conditioned samples, onsetting nonlinear behaviour could already be observed at a mean strain of 0.3%. The influence of moisture was succesfully taken into account by choosing the moisture-dependent glass

transition temperature as reference temperature of the master curves. A comparison of master curves from tests conducted with and without humidity control showed no significant deviations. It was concluded, that the influence of diffusion processes during temperature-frequency testing is neglectable. Furthermore, the parameter identification of a GMM by least squares optimization was discussed. It was shown that both storage and loss modulus should be considered in the residual. In addition, it was confirmed that between one and two Maxwell elements per frequency decade should be prescribed in a logarithmic distribution in order to obtain good results.

Entropy relaxation in PS. To model the behavior of the isobaric heat capacity of PS in the vicinity of the glass transition, the viscocaloric model was applied. The internal temperature of the model is thereby comparable to the fictive temperature introduced by Tool (1945). In comparison to the TNM or KAHR model, the viscocaloric model presented in this work is a simplification as only a temperature-dependency, modeled by the WLF equation, and a rate-dependent scaling factor of the relaxation time were considered. The qualitative behavior of the model was illustrated by cooling and heating simulations. Regarding parameter identification, heat capacity measurements at two temperature rates served as input. First, the behavior in the glassy and equilibrium state was approximated by linear functions. By construction, a function for the equilibrium heat capacity was fitted. This function was suggested by Lion et al. (2017) and, in this work, an axis intercept was added. For the consideration of the glass transition regime, the reduced heat capacity was calculated from the experimental data based on the equilibrium heat capacity determined before. It was shown that the initial values of the internal temperature in heating processes can be calculated from experimental data although the temperature history is unknown. Relaxation time and WLF equation were fitted based on the heating curve at the smaller temperature rate.

For the larger temperature rate, the relaxation time needed to be adjusted in order to not overestimate the rate-dependency of the glass transition temperature. Thus, the rate-dependent scaling factor of the relaxation time was motivated. Based on cooling simulations, it was shown that the scaling function is strongly nonlinear if a linear rate-dependency of the glass transition temperature is assumed. The qualitative behavior of the heating curves could be reproduced by the model. However, the exothermal undershoots and endothermal overshoots were overestimated. Cooling simulations predicted the experimental cooling curves well. In literature, the TNM and KAHR model, that use more complex formulations, also show inaccuracies. Therefore, it is concluded that the viscocaloric model presented here delivers acceptable results.

6.2 Outlook

In this thesis, selected aspects of the thermomechanical behaviour of thermoplastics and the corresponding modelling were dealt with. Thus, further aspects, that were not addressed and could be considered in extensions of the model, are to be mentioned here.

- Three-dimensional formulations of viscoelasticity are needed for structural calculations in, e.g., finite element frameworks. However, the GMM was only applied for a uniaxial load case in this work. For insights on three-dimensional viscoelasticity, the behavior of Poisson's ratio or shear modulus must also be taken into account.
- Regarding temperature-dependent viscoelasticity, limitations of extended TTS and onsetting nonlinearity were observed. This indicates that a nonlinear viscoelastic model is already needed in the small strain regime. Therefore, the modeling should not be restricted to linear irreversible thermodynamics.

- By the consideration of PA6 in different conditioning states, it becomes obvious that water uptake significantly influences the viscoelastic behavior of the material. If the moisture content is not fixed, a coupled model of diffusion and viscoelasticity is needed, cf. Dyck et al. (2024). In this case, the moisture content is an additional state variable.
- In the consideration of the caloric behavior, a coupling to the mechanical behavior was neglected in this work. However, if, e.g., a pressure-dependency of the heat capacity and entropy relaxation is analyzed, this coupling is necessary.
- For the consideration of caloric behavior in a field theory, heat conduction must also be taken into account, cf. Liu et al. (2013). The investigation of the change in heat conductivity during the glass transition could be a relevant research objective.
- PA6 is a semicrystalline polymer. However, in this work, this was not considered meaning that only the effective, macroscopic behavior of the semicrystalline material was considered. A coupled theory of crystallization and thermoviscoelasticity that accounts for crystalline and amorphous phases is needed for that, cf. Lion and Johlitz (2016).

Appendix A

Generalized thermorheological models

A.1 Derivation of differential equations

A.1.1 Generalized Maxwell model

Derivating the viscoelastic pressure, see Eq. (3.19), with respect to time and inserting the evolution equation (3.20) gives

$$\eta_{\mathrm{v}i}\dot{p}_{\mathrm{v}i} + K_i p_{\mathrm{v}i} = -K_i\eta_{\mathrm{v}i}\dot{\varepsilon}^{\mathrm{vol}} + 3\alpha_i K_i \eta_{\mathrm{v}i}\dot{\theta}. \tag{A.1}$$

For simplification, the temperature-dependency of the viscosities is not considered in the following. Applying Laplace transformation and assuming vanishing initial values then leads to

$$\mathcal{L}(p_{\mathrm{v}i}) = -\frac{K_i\eta_{\mathrm{v}i}s}{K_i+\eta_{\mathrm{v}i}s}\mathcal{L}(\varepsilon^{\mathrm{vol}}) + \frac{3\alpha_i K_i\eta_{\mathrm{v}i}s}{K_i+\eta_{\mathrm{v}i}s}\mathcal{L}(\Delta\theta). \tag{A.2}$$

With the Laplace transformation of the equilibrium pressure,

$$\mathcal{L}(p_{\mathrm{e}}) = -K_0\mathcal{L}(\varepsilon^{\mathrm{vol}}) + 3\alpha_0 K_0\mathcal{L}(\Delta\theta), \tag{A.3}$$

the Laplace transformation of the total pressure, due to linearity, is given by

$$\mathcal{L}(p) = \mathcal{L}(p_{\mathrm{e}}) + \sum_{i=1}^{N} \mathcal{L}(p_{\mathrm{v}i}). \tag{A.4}$$

Inserting Eq. (A.2) and applying the common denominator finally gives

$$\begin{aligned}
&\left(\prod_{j=1}^{N}(K_j + \eta_{\mathrm{v}j}s)\right)\mathcal{L}(p) \\
&= -\left(K_0\prod_{j=1}^{N}(K_j + \eta_{\mathrm{v}j}s) + \sum_{i=1}^{N} K_i\eta_{\mathrm{v}i}s\prod_{j=1,j\neq i}^{N}(K_j + \eta_{\mathrm{v}j}s)\right)\mathcal{L}(\varepsilon^{\mathrm{vol}}) \\
&\quad + 3\left(\alpha_0 K_0\prod_{j=1}^{N}(K_j + \eta_{\mathrm{v}j}s) + \sum_{i=1}^{N}\alpha_i K_i\eta_{\mathrm{v}i}s\prod_{j=1,j\neq i}^{N}(K_j + \eta_{\mathrm{v}j}s)\right)\mathcal{L}(\Delta\theta).
\end{aligned} \tag{A.5}$$

Regarding s, this is a polynom of degree N. By the rules of Laplace transformation, this is equivalent to an ODE of order N in the time domain, see Eq. (3.22). The coefficients of the ODE regarding the purely mechanical behavior are given by

$$a_k = \frac{1}{k!}\frac{\partial^k F_p(x)}{\partial x^k}\bigg|_{x=0}, \quad b_k = \frac{1}{k!}\frac{\partial^k F_\varepsilon(x)}{\partial x^k}\bigg|_{x=0}, \quad k = 0, 1, \ldots, N, \tag{A.6}$$

$$F_p(x) = \prod_{j=1}^{N}(K_j + \eta_{\mathrm{v}j}x), \tag{A.7}$$

$$F_\varepsilon(x) = K_0\prod_{j=1}^{N}(K_j + \eta_{\mathrm{v}j}x) + \sum_{i=1}^{N} K_i\eta_{\mathrm{v}i}x\prod_{j=1,j\neq i}^{N}(K_j + \eta_{\mathrm{v}j}x). \tag{A.8}$$

The remaining coefficients regarding thermal expansion are defined via

$$c_k = \sum_{l=0}^{N} A_{kl}\alpha_l, \quad k = 0, 1, \ldots, N, \tag{A.9}$$

$$A_{k0} = \frac{K_0}{k!}\frac{\partial^k f_0(x)}{\partial x^k}\bigg|_{x=0}, \quad A_{kl} = \frac{K_l\eta_l}{k!}\frac{\partial^k f_l(x)}{\partial x^k}\bigg|_{x=0}, \quad l = 1, \ldots, N, \tag{A.10}$$

$$f_0(x) = \prod_{j=1}^{N}(K_j + \eta_{\mathrm{v}j}x), \quad f_l(x) = x\prod_{j=1, j\neq l}^{N}(K_j + \eta_{\mathrm{v}j}x). \tag{A.11}$$

A.1.2 Generalized Kelvin model

Applying Laplace transformation to Eq. (3.26) and assuming vanishing initial values leads to

$$\mathcal{L}(\widetilde{\varepsilon}_{\mathrm{v}i}^{\mathrm{vol}}) = -\left(\frac{1}{\widetilde{K}_i + \widetilde{\eta}_{\mathrm{v}i}s}\right)\mathcal{L}(p) + 3\left(\frac{\widetilde{K}_i\widetilde{\alpha}_i}{\widetilde{K}_i + \widetilde{\eta}_{\mathrm{v}i}s}\right)\mathcal{L}(\Delta\theta), \quad i = 0, 1, \ldots, N. \tag{A.12}$$

To shorten the following expressions, the single spring element is assumed to be a Kelvin-Voigt element with vanishing viscosity, $\widetilde{\eta}_{\mathrm{v}0} = 0$. Applying Laplace transformation to the total strain and using the additive decomposition gives

$$\mathcal{L}(\varepsilon^{\mathrm{vol}}) = \sum_{i=0}^{N}\mathcal{L}(\widetilde{\varepsilon}_{\mathrm{v}i}^{\mathrm{vol}}). \tag{A.13}$$

By using Eq. (A.12) and applying the common denominator, this gives

$$\left(\sum_{i=0}^{N}\prod_{j=0,j\neq i}^{N}(\widetilde{K}_j+\widetilde{\eta}_{\mathrm{v}j}s)\right)\mathcal{L}(p)$$
$$=-\left(\prod_{j=0}^{N}(\widetilde{K}_j+\widetilde{\eta}_{\mathrm{v}j}s)\right)\mathcal{L}(\varepsilon^{\mathrm{vol}})+3\left(\sum_{i=0}^{N}\widetilde{\alpha}_i\widetilde{K}_i\prod_{j=0,j\neq i}^{N}(\widetilde{K}_j+\widetilde{\eta}_{\mathrm{v}j}s)\right)\mathcal{L}(\Delta\theta). \tag{A.14}$$

In the time domain, this is an ODE of order N, see Eq. (3.28). The coefficients regarding the purely mechanical behavior are given by

$$\widetilde{a}_k=\frac{1}{k!}\frac{\partial^k\widetilde{F}_p(x)}{\partial x^k}\bigg|_{x=0},\quad \widetilde{b}_k=\frac{1}{k!}\frac{\partial^k\widetilde{F}_\varepsilon(x)}{\partial x^k}\bigg|_{x=0},\quad k=0,1,\ldots,N, \tag{A.15}$$

$$\widetilde{F}_p(x)=\sum_{i=0}^{N}\prod_{j=0,j\neq i}^{N}(\widetilde{K}_j+\widetilde{\eta}_{\mathrm{v}j}x),\quad \widetilde{F}_\varepsilon(x)=\prod_{j=0}^{N}(\widetilde{K}_j+\widetilde{\eta}_{\mathrm{v}j}x). \tag{A.16}$$

The remaining coefficients regarding thermal expansion are

$$\widetilde{c}_k=\sum_{l=0}^{N}\widetilde{A}_{kl}\widetilde{\alpha}_l,\quad k=0,1,\ldots,N, \tag{A.17}$$

$$\widetilde{A}_{kl}=\frac{\widetilde{K}_l}{k!}\frac{\partial^k\widetilde{f}_l(x)}{\partial x^k}\bigg|_{x=0},\quad \widetilde{f}_l(x)=\prod_{j=0,j\neq l}^{N}(\widetilde{K}_j+\widetilde{\eta}_{\mathrm{v}j}x). \tag{A.18}$$

A.2 Prony series conversion

To convert the stiffnesses and viscosities of a GMM and a GKM numerically, the method of Loy et al. (2015) can be used. Here, a short summary of the method and its derivation is given. The method is based on the Prony series representation, see Eq. (3.37) and (3.39).

Laplace transformation. The Laplace transformations of the Boltzmann superposition integrals in Eq. (3.38) and (3.40) are given by

$$-\mathcal{L}(p) = \mathcal{L}(K)s\mathcal{L}(\varepsilon^{\mathrm{vol}}), \tag{A.19}$$

$$\mathcal{L}(\varepsilon^{\mathrm{vol}}) = -\mathcal{L}(J)s\mathcal{L}(p). \tag{A.20}$$

Combining these equations yields

$$\mathcal{L}(J)\mathcal{L}(K) = \frac{1}{s^2}. \tag{A.21}$$

Applying inverse Laplace transformation gives the convolution integrals

$$t = \int_0^t J(t-s)K(s)\,\mathrm{d}s = \int_0^t K(t-s)J(s)\,\mathrm{d}s. \tag{A.22}$$

The Laplace transformation of the bulk relaxation modulus in Eq. (3.37) is

$$\mathcal{L}(K)(s) = \frac{K_0}{s} + \sum_{i=1}^{N} \frac{K_i}{s+a_i}, \quad a_i = \frac{1}{\tau_{\mathrm{v}i}}, \tag{A.23}$$

and the Laplace transformation of the bulk creep compliance in (3.39) is

$$\mathcal{L}(J)(s) = \frac{j_0}{s} - \sum_{i=1}^{N} \frac{j_i}{s+b_i}, \quad b_i = \frac{1}{\widetilde{\tau}_{\mathrm{v}i}},$$

$$j_0 = \sum_{j=0}^{N} \widetilde{K}_j^{-1}, \quad j_i = \widetilde{K}_i^{-1}, \quad i = 1, \ldots, N. \tag{A.24}$$

Retardation and relaxation times. The work of Whittaker (1918) has important implications for the relation between relaxation modulus and creep compliance:

- The number of Prony series elements N is the same for $K(t)$ and $J(t)$.

- $\mathcal{L}(K)(s)$ has simple poles at $s = -a_1, \ldots, -a_N$ which coincide with roots of $\mathcal{L}(J)(s)$.
- $\mathcal{L}(J)(s)$ has simple poles at $s = -b_1, \ldots, -b_N$ which coincide with roots of $\mathcal{L}(K)(s)$.
- $\tau_{\mathrm{v}1} < \widetilde{\tau}_{\mathrm{v}1} < \tau_{\mathrm{v}2} < \cdots < \tau_{\mathrm{v}N-1} < \widetilde{\tau}_{\mathrm{v}N-1} < \tau_{\mathrm{v}N} < \widetilde{\tau}_{\mathrm{v}N}$

The retardation times $\widetilde{\tau}_{\mathrm{v}i}$ or the relaxation times $\tau_{\mathrm{v}i}$ are determined by finding the roots of $\mathcal{L}(K)(s)$ or $\mathcal{L}(K)(s)$, respectively. For that, Loy et al. (2015) proposed to use a bisection method.

Prony series coefficients. If the retardation or relaxation times are known, the Prony series coeffiecients can be calculated via residue calculus, see, e.g., Marsden and Hoffman (1999). Therefore, the Laurent series is helpful. The Laurent series of a complex function $f(s)$ about a point a,

$$f(s) = \sum_{k=1}^{\infty} \frac{a_{-k}}{(s-a)^k} + \sum_{k=0}^{\infty} a_k (s-a)^k, \tag{A.25}$$

can be used to describe the behavior of $f(s)$ in the vicinity of an isolated singularity a. The residue of $f(s)$ at the singularity a is equal to the Laurent series coefficient a_{-1}. If

$$f(s) = \frac{g(s)}{h(s)}, \quad g(a) \neq 0, \quad h(a) = 0, \quad h'(a) \neq 0 \tag{A.26}$$

holds, the residue can be calculated by

$$\mathrm{Res}(f, a) = a_{-1} = \frac{g(a)}{h'(a)}. \tag{A.27}$$

The properties in Eq. (A.26) are satisfied by Eq. (A.21) if

$$g(s) = \frac{1}{s^2}, \quad h(s) = \mathcal{L}(K)(s), \quad f(s) = \mathcal{L}(J)(s). \tag{A.28}$$

This yields

$$\mathrm{Res}(\mathcal{L}(J), -b_i) = a_{-1,i} = \left(b_i^2 \frac{\mathrm{d}\mathcal{L}(K)}{\mathrm{d}s}\bigg|_{s=-b_i} \right)^{-1}, \quad i = 1, \ldots, N. \tag{A.29}$$

In the vicinity of the singularity $-b_i$, $\hat{J}(s)$ can be approximated by

$$\mathcal{L}(J)(s) \approx -\frac{j_i}{s + b_i}. \tag{A.30}$$

By comparing Eq. (A.25) and Eq. (A.30), it can be seen that

$$-\frac{j_i}{s + b_i} = \frac{a_{-1,i}}{s + b_i} \tag{A.31}$$

holds, yielding $j_i = -a_{-1,i}$. Thus, the Prony series coefficients are given by

$$j_i = -\left(b_i^2 \frac{\mathrm{d}\mathcal{L}(K)}{\mathrm{d}s}\bigg|_{-b_i} \right)^{-1}, \quad i = 1, \ldots, N. \tag{A.32}$$

Applying the same procedure to the relaxation modulus gives

$$K_i = \left(a_i^2 \frac{\mathrm{d}\mathcal{L}(J)}{\mathrm{d}s}\bigg|_{-a_i} \right)^{-1}, \quad i = 1, \ldots, N. \tag{A.33}$$

Both, $\mathcal{L}(J)(s)$ and $\mathcal{L}(K)(s)$, have another simple pole at $s = 0$. To determine j_0 or K_0, the convolution integral in Eq. (A.22) is considered for $t \to 0$ (Lion, 2007). Therefore, the substitution $s = tx$ is used,

$$t = \int_0^t J(t - tx) R(tx) t \, \mathrm{d}x. \tag{A.34}$$

Dividing by t,

$$1 = \int_0^1 J(t(1-x))R(tx)\,\mathrm{d}x, \tag{A.35}$$

and considering $t \to 0$ gives

$$1 = J(0)R(0). \tag{A.36}$$

Using Eq. (A.36) and the already known coefficients, j_0 or K_0 can be calculated by

$$j_0 = \left(\sum_{i=0}^{N} K_i\right)^{-1} + \sum_{i=1}^{N} j_i, \tag{A.37}$$

$$K_0 = \left(j_0 - \sum_{i=1}^{N} j_i\right)^{-1} - \sum_{i=1}^{N} K_i. \tag{A.38}$$

The stiffnesses of the GKM can be determined by the Prony series coefficients via Eq. (A.24), whilst the stiffnesses of the GMM are directly given.

A.3 Heat capacity of generalized thermorheological models

In Ch. 5, the heat capacity of a viscocaloric model is discussed. However, if a thermoviscoelastic model is superposed, further contributions to the process-dependent heat capacity arise. These contributions are given here. Under isobaric conditions, the GKM is the natural model and should be used. With the free enthalpy defined in Eq. (3.24), the contribution of the

GKM to the isobaric heat capacity is given by

$$\begin{aligned} c_p^{\mathrm{GKM}} &= \frac{\dot{h}}{\dot{\theta}}\bigg|_{p=\mathrm{const}} = \frac{\dot{g} + s\dot{\theta} + \dot{s}\theta}{\dot{\theta}}\bigg|_{p=\mathrm{const}} \\ &= \sum_{i=1}^{N} \left[-\frac{9\widetilde{\alpha}_i^2 \widetilde{K}_i \theta}{\varrho_0} + \left(p + \widetilde{K}_i (\widetilde{\varepsilon}_{\mathrm{v}i}^{\mathrm{vol}} + 3\widetilde{\alpha}_i \theta_0) \right) \frac{\dot{\widetilde{\varepsilon}}_{\mathrm{v}i}^{\mathrm{vol}}}{\varrho_0 \dot{\theta}} \right]. \end{aligned} \tag{A.39}$$

If, instead, an iscochoric process is considered, the GMM should be used. The derivation of the isochoric heat capacity is analog to the derivation of the isobaric heat capacity, giving

$$\begin{aligned} c_v^{\mathrm{GMM}} &= \frac{\dot{e}}{\dot{\theta}}\bigg|_{v=\mathrm{const}} = \frac{\dot{\psi} + s\dot{\theta} + \dot{s}\theta}{\dot{\theta}}\bigg|_{p=\mathrm{const}} \\ &= -\frac{9\alpha_0^2 K_0 \theta}{\varrho_0} + \sum_{i=1}^{N} \left[-\frac{9\alpha_i^2 K_i \theta}{\varrho_0} - K_i \left(\varepsilon^{\mathrm{vol}} - \varepsilon_{\mathrm{v}i}^{\mathrm{vol}} + 3\alpha_i \theta_0 \right) \frac{\dot{\varepsilon}_{\mathrm{v}i}^{\mathrm{vol}}}{\varrho_0 \dot{\theta}} \right]. \end{aligned} \tag{A.40}$$

Note that the equilibrium stiffness and equilibrium thermal expansion coefficient also contribute to the isochoric heat capacity. For the isobaric heat capacity, this is not the case. In a purely caloric model, the difference between the isochoric and the isobaric heat capacity vanishes.

Appendix B

Thermoviscoelasticity of PA6

B.1 Cole-Cole plots

To check if TTS is applicable, Cole-Cole plots can be used (Cole and Cole, 1941). In these plots, the storage modulus is plotted over the loss modulus for all considered temperatures and frequencies. If TTS is valid, smooth master curves of storage and loss modulus can be constructed, see Fig. 4.7. Due to the monotonic behavior of the storage modulus, each value of the storage modulus is assigned to a unique value of the loss modulus. Furthermore, the master curves are smooth functions. Thus, the Cole-Cole plots must also be smooth if TTS is applicable (Guedes, 2011; Sodeifian and Haghtalab, 2004). As an example, the Cole-Cole plots of temperature-frequency tests with DAM samples at various mean strains are shown in Fig. B.1.1. For $\varepsilon_0 = 0.1\%$, the middle part of the Cole-Cole plot is smooth, which indicates that TTS is applicable in the corresponding temperature range. At the left end, data points are stacked and at the right end, the plot is not smooth. The corresponding data points were not considered in Sec. 4.4.2. In case of $\varepsilon_0 = 0.5\%$, the Cole-Cole plot shows that TTS is invalid.

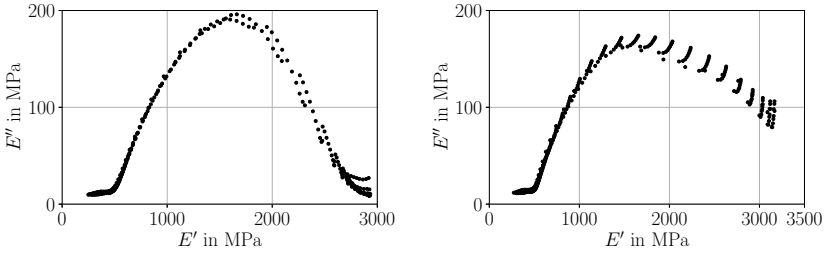

(a) DAM, $\varepsilon_0 = 0.1\%$ **(b)** DAM, $\varepsilon_0 = 0.5\%$

Figure B.1.1: Cole-Cole plots of temperature-frequency tests with DAM samples. For $\varepsilon_0 = 0.1\%$, the Cole-Cole plot is smooth. For $\varepsilon_0 = 0.5\%$, it is not. These plots are taken from Figure 14 and Figure 15 in Kehrer et al. (2023).

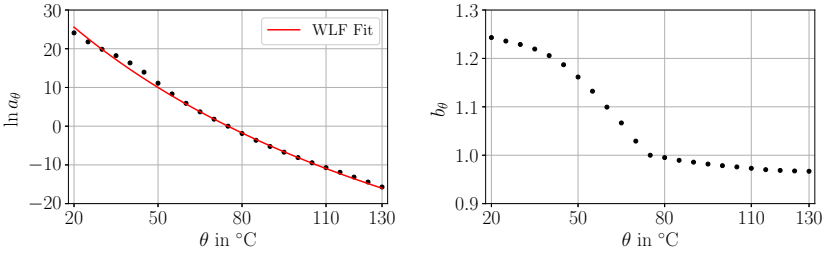

(a) Horizontal shift factors and WLF fit **(b)** Vertical shift factors

Figure B.1.2: The horizontal shift factors corresponding to the master curves in Fig. 4.6 and 4.7 are shown by black dots. In the left plot, the red line shows a fit of the WLF equation with $\theta_{\text{ref}} = 75°\text{C}$, $c_1 = 85.9$, $c_2 = 239.8$ K. The left plot is an adaption of Figure 4 in Keursten et al. (2023), where a different reference temperature was used.

B.2 Shift factors

The horizontal and vertical shift factors corresponding to the master curves in Fig. 4.6 and 4.7 are shown in Fig. B.1.2. Both horizontal and vertical shift decrease with increasing temperature. This means that the viscosities and the stiffnesses are smaller for higher temperatures. Regarding the horizontal shifts, a WLF equation is fitted to the data points by least squares optimization, see Fig. B.1.2a. In the considered temperature interval, the course of the determined WLF equation matches well with the shift factors. This includes temperatures above and below the glass transition temperature of $75°\mathrm{C}$. In contrast, a kink of the vertical shift is observed at the glass transition temperature. Last, it is noted that the impact of the horizontal shift (temperature-dependency of the viscosities) is much larger than the impact of the vertical shift (temperature-dependency of the stiffnesses). The vertical shift factor is close to 1, whilst the horizontal shift factor covers multiple decades.

B.3 GMM parameters

For completeness, the determined values of the GMM parameters (stiffnesses and relaxation times) regarding the parameter identification depicted in Fig. 4.13 are given in Tab. B.1

Figure 4.13a			Figure 4.13b		
i	E_i in MPa	τ_i in s	i	E_i in MPa	τ_i in s
0	459.2		0	422.8	
1	22.41	1.0e-12	1	87.53	1.0e-15
2	6.29	4.52e-12	2	71.48	5.74e-15
3	16.97	2.04e-11	3	82.1	3.29e-14
4	14.1	9.24e-11	4	88.36	1.89e-13
5	20.76	4.18e-10	5	91.56	1.08e-12
6	24.42	1.89e-09	6	95.7	6.21e-12
7	31.83	8.53e-09	7	97.8	3.56e-11
8	43.89	3.86e-08	8	102.15	2.04e-10
9	55.77	1.74e-07	9	103.13	1.17e-09
10	79.57	7.88e-07	10	112.57	6.72e-09
11	102.59	3.56e-06	11	119.26	3.86e-08
12	131.95	1.61e-05	12	131.55	2.21e-07
13	157.2	7.28e-05	13	146.83	1.27e-06
14	170.07	3.29e-04	14	162.89	7.28e-06
15	170.95	1.49e-03	15	172.77	4.18e-05
16	158.64	6.72e-03	16	169.1	2.4e-04
17	140.45	3.04e-02	17	156.97	1.37e-03
18	118.99	1.37e-01	18	134.69	7.88e-03
19	99.85	6.21e-01	19	113.74	4.52e-02
20	80.91	2.81e00	20	95.46	2.59e-01
21	63.24	1.27e01	21	76.64	1.49e00
22	48.31	5.74e01	22	60.24	8.43e00
23	36.14	2.59e02	23	45.85	4.89e01
24	27.65	1.17e03	24	34.47	2.81e02
25	21.15	5.3e03	25	25.66	1.61e03
26	17.75	2.4e04	26	20.62	9.24e04
27	15.33	1.08e05	27	16.83	5.3e04
28	13.75	4.89e05	28	15.04	3.04e05
29	13.92	2.21e06	29	14.55	1.74e06
30	16.61	1.0e07	30	17.01	1.0e07

Table B.1: Identified GMM parameters for DAM samples tested at a mean strain of $\varepsilon_0 = 0.1\%$ (left) and $\varepsilon_0 = 0.3\%$ (right) with $\theta_{\mathrm{ref}} = 75°\mathrm{C}$. The fits are depicted in Fig. 4.13. This table is taken from Table 8 and Table 9 in Kehrer et al. (2023).

Bibliography

Adam, G., Gibbs, J., 1965. On the temperature dependence of cooperative relaxation properties in glass-forming liquids. Journal of Chemical Physics 43 (1), 139–146.

Alwis, K., Burgoyne, C., 2006. Time-temperature superposition to determine the stress-rupture of aramid fibres. Applied Composite Materials 13 (4), 249–264.

Andreozzi, L., Faetti, M., Giordano, M., Zulli, F., 2005. Molecular-weight dependence of enthalpy relaxation of PMMA. Macromolecules 38 (14), 6056–6067.

Androsch, R., Schick, C., Schmelzer, J., 2014. Sequence of enthalpy relaxation, homogeneous crystal nucleation and crystal growth in glassy polyamide 6. European Polymer Journal 53, 100–108.

Argatov, I., Kocherbitov, V., 2021. Analysis of the minimal model for the enthalpy relaxation and recovery in glass transition: application to constant-rate differential scanning calorimetry. Continuum Mechanics and Thermodynamics 33 (1), 107–123.

Arhant, M., Le Gac, P., Le Gall, M., Burtin, C., Briançon, C., Davies, P., 2016. Modelling the non Fickian water absorption in polyamide 6. Polymer Degradation and Stability 133, 404–412.

Arikoglu, A., 2014. A new fractional derivative model for linearly viscoelastic materials and parameter identification via genetic algorithms. Rheologica Acta 53 (3), 219–233.

ASTM E1356-23, 2023. Standard test method for assignment of the glass transition temperatures by differential scanning calorimetry. ASTM International, West Conshohocken, PA, USA.

Badrinarayanan, P., Zheng, W., Li, Q., Simon, S., 2007. The glass transition temperature versus the fictive temperature. Journal of Non-Crystalline Solids 353 (26), 2603–2612.

Bae, J., Cho, K., Seo, K., Kang, D., 2011. Application of geometric algorithm of time-temperature superposition to linear viscoelasticity of rubber compounds. Korea-Australia Rheology Journal 23 (2), 81–87.

Banks, H., Hu, S., Kenz, Z., 2011. A brief review of elasticity and viscoelasticity for solids. Advances in Applied Mathematics and Mechanics 3 (1), 1–51.

Beijer, J., Spoormaker, J., 2002. Solution strategies for FEM analysis with nonlinear viscoelastic polymers. Computers & Structures 80 (14-15), 1213–1229.

Bertilsson, H., Jansson, J., 1975. The limits of linear viscoelasticity in poly(methyl methacrylate) and poly(ethyl methacrylate). Journal of Applied Polymer Science 19 (7), 1971–1978.

Böhlke, T., Henning, F., Hrymak, A., Kärger, L., Weidenmann, K., Wood, J., 2019. Continuous-Discontinuous Fiber-Reinforced Polymers. Carl Hanser Verlag, München.

Bonet, J., 2001. Large strain viscoelastic constitutive models. International Journal of Solids and Structures 38 (17), 2953–2968.

Bradshaw, R., Brinson, L., 1997. A sign control method for fitting and interconverting material functions for linearly viscoelastic solids. Mechanics of Time-Dependent Materials 1 (1), 85–108.

Brinson, H., Brinson, L., 2015. Polymer Engineering Science and Viscoelasticity, 2nd Edition. Springer Science+Business Media, New York.

Broudin, M., Le Gac, P., Le Saux, V., Champy, C., Robert, G., Charrier, P., Marco, Y., 2015. Water diffusivity in PA66: Experimental characterization and modeling based on free volume theory. European Polymer Journal 67, 326–334.

Capodagli, J., Lakes, R., 2008. Isothermal viscoelastic properties of PMMA and LDPE over 11 decades of frequency and time: a test of time-temperature superposition. Rheologica Acta 47 (7), 777–786.

Caracciolo, R., Giovagnoni, M., 1996. Frequency dependence of Poisson's ratio using the method of reduced variables. Mechanics of Materials 24 (1), 75–85.

Chen, D., Yang, P., Lai, Y., 2012. A review of three-dimensional viscoelastic models with an application to viscoelasticity characterization using nanoindentation. Microelectronics Reliability 52 (3), 541–558.

Cho, K., 2009. Geometric interpretation of time-temperature superposition. Korea-Australia Rheology Journal 21 (1), 13–16.

Cho, K., Hyun, K., Ahn, K., Lee, S., 2005. A geometrical interpretation of large amplitude oscillatory shear response. Journal of Rheology 49 (3), 747–758.

Cole, K., Cole, R., 1941. Dispersion and absorption in dielectrics I. Alternating current characteristics. The Journal of Chemical Physics 9 (4), 341–351.

Coleman, B., Noll, W., 1963. The thermodynamics of elastic materials with heat conduction and viscosity. Archive for Rational Mechanics and Analysis 13 (1), 167–178.

Crochon, T., Schönherr, T., Li, C., Lévesque, M., 2010. On finite-element implementation strategies of Schapery-type constitutive theories. Mechanics of Time-dependent Materials 14 (4), 359–387.

Dealy, J., Plazek, D., 2009. Time-temperature superposition - a users guide. Rheology Bulletin 78 (2), 16–31.

Diani, J., Gilormini, P., Frédy, C., Rousseau, I., 2012. Predicting thermal shape memory of crosslinked polymer networks from linear viscoelasticity. International Journal of Solids and Structures 49 (5), 793–799.

Domininghaus, H., Elsner, P., Eyerer, P., Hirth, T., 2012. Kunststoffe, 8th Edition. Springer-Verlag, Heidelberg.

Doolittle, A., Doolittle, D., 1957. Studies in Newtonian flow. V. Further verification of the free-space viscosity equation. Journal of Applied Physics 28 (8), 901–905.

Dyck, A., Groß, L., Keursten, J., Kehrer, L., Böhlke, T., 2024. Modeling and FE simulation of coupled water diffusion and viscoelasticity in relaxation tests of polyamide 6. Continuum Mechanics and Thermodynamics 36, 935–953.

Ehrenstein, G., 2011. Polymer Werkstoffe, 3rd Edition. Carl Hanser Verlag, München.

Engelhard, M., Lion, A., 2013. Modelling the hydrothermomechanical properties of polymers close to glass transition. ZAMM-Journal of Applied Mathematics and Mechanics/Zeitschrift für Angewandte Mathematik und Mechanik 93 (2-3), 102–112.

Ewoldt, R., Bharadwaj, N., 2013. Low-dimensional intrinsic material functions for nonlinear viscoelasticity. Rheologica Acta 52 (3), 201–219.

Fabre, V., Quandalle, G., Billon, N., Cantournet, S., 2018. Time-temperature-water content equivalence on dynamic mechanical response of polyamide 6,6. Polymer 137, 22–29.

Ferry, J., 1980. Viscoelastic Properties of Polymers, 3rd Edition. John Wiley & Sons, New York.

Findley, W., Lai, J., Onaran, K., 1989. Creep and Relaxation of Nonlinear Viscoelastic Materials. Dover Publications, New York.

Fulcher, G., 1925. Analysis of recent measurements of the viscosity of glasses. Journal of the American Ceramic Society 8 (6), 339–355.

Gedde, U., 1999. Polymer Physics, 3rd Edition. Springer Science+Business Media, Dordrecht.

Gergesova, M., Saprunov, I., Emri, I., 2016. Closed-form solution for horizontal and vertical shiftings of viscoelastic material functions in frequency domain. Rheologica Acta 55 (5), 351–364.

Gergesova, M., Zupančič, B., Saprunov, I., Emri, I., 2011. The closed form t-T-P shifting (CFS) algorithm. Journal of Rheology 55 (1), 1–16.

Ghobadi, E., Sivanesapillai, R., Musialak, J., Steeb, H., 2015. Thermo-rheological characterization of polyetherurethane: Parameter optimization and validation. In: Marvalova, B., Petrikova, I. (Eds.), Constitutive Models for Rubbers IX. CRC Press/Balkema, Leiden, pp. 157–163.

Gibbs, J., DiMarzio, E., 1958. Nature of the glass transition and the glassy state. The Journal of Chemical Physics 28 (3), 373–383.

Göhler, J., 2011. Das dreidimensionale Stoffverhalten im großen Temperatur- und Zeitbereich am Beispiel eines in der automobilen Aufbau- und Verbindungstechnik verwendeten Epoxidharzklebstoffs. Berichte aus der Materialwissenschaft. Shaker Verlag, Aachen.

Görthofer, J., Meyer, N., Pallicity, T., Schöttl, L., Trauth, A., Schemmann, M., Hohberg, M., Pinter, P., Elsner, P., Henning, F., Hrymak, A., Seelig, T., Weidenmann, K., Kärger, L., Böhlke, T., 2019. Virtual process chain of sheet molding compound: Development, validation and perspectives. Composites Part B: Engineering 169, 133–147.

Guedes, R., 2011. A viscoelastic model for a biomedical ultra-high molecular weight polyethylene using the time-temperature superposition principle. Polymer Testing 30 (3), 294–302.

Gurtin, M., Fried, E., Anand, L., 2010. The Mechanics and Thermodynamics of Continua. Cambridge University Press, New York.

Gutierrez-Lemini, D., 2014. Engineering Viscoelasticity. Springer Science+Business Media, New York.

Gutzow, I., Schmelzer, J., Petroff, B., 2008. Phenomenological theories of glass transition: Classical approaches, new solutions and perspectives. Journal of Non-Crystalline Solids 354 (2-9), 311–324.

Halphen, B., Nguyen, Q., 1975. Sur les matériaux standard généralisés. Journal de Mécanique 14 (1), 39–63.

Hammami, I., Hammami, H., Soulestin, J., Arous, M., Kallel, A., 2019. Thermal and dielectric behavior of polyamide-6/clay nanocomposites. Materials Chemistry and Physics 232, 99–108.

Haupt, P., 2002. Continuum Mechanics and Theory of Materials, 2nd Edition. Advanced Texts in Physics. Springer-Verlag, Berlin.

Hermida, E., Povolo, F., 1994. Analytical-numerical procedure to determine if a set of experimental curves can be superimposed to form a master curve. Polymer Journal 26 (9), 981–992.

Hess, M., Allegra, G., He, J., Horie, K., Kim, J., Meille, S., Metanomski, V., Moad, G., Stepto, R., Vert, M., Vohlídal, J., 2013. Glossary of terms relating to thermal and thermo mechanical properties of polymers (IUPAC recommendations 2013). Pure and Applied Chemistry 85 (5), 1017–1046.

Hirschberg, V., Wilhelm, M., Rodrigue, D., 2020. Fourier transform fatigue analysis of the stress in tension/tension of HDPE and PA6. Polymer Engineering and Science 61 (4), 993–1006.

Hodge, I., 1991. Adam-Gibbs formulation of non-linear enthalpy relaxation. Journal of Non-Crystalline Solids 131-133, 435–441.

Hodge, I., 1994. Enthalpy relaxation and recovery in amorphous materials. Journal of Non-Crystalline Solids 169 (3), 211–266.

Höhne, G., Hemminger, W., Flammersheim, H., 2003. Differential Scanning Calorimetry, 2nd Edition. Springer-Verlag, Berlin.

Honerkamp, J., Weese, J., 1989. Determination of the relaxation spectrum by a regularization method. Macromolecules 22 (11), 4372–4377.

Honerkamp, J., Weese, J., 1990. Tikhonovs regularization method for ill-posed problems. Continuum Mechanics and Thermodynamics 2 (1), 17–30.

Honerkamp, J., Weese, J., 1993. A note on estimating mastercurves. Rheologica Acta 32 (1), 57–64.

Hu, X., Luo, W., Liu, X., Li, M., Huang, Y., Bu, J., 2013. Temperature and frequency dependent rheological behaviour of carbon black filled natural rubber. Plastics, Rubber and Composites 42 (10), 416–420.

Ishisaka, A., Kawagoe, M., 2004. Examination of the time-water content superposition on the dynamic viscoelasticity of moistened polyamide 6 and epoxy. Journal of Applied Polymer Science 93 (2), 560–567.

ISO 291, 2008. Plastics - Standard atmospheres for conditioning and testing, 4th Edition. International Organization for Standardization, Geneva, CH.

Jalocha, D., Constantinescu, A., Neviere, R., 2015. Revisiting the identification of generalized Maxwell models from experimental results. International Journal of Solids and Structures 67-68, 169–181.

Janeschitz-Kriegl, H., 2018. Crystallization Modalities in Polymer Melt Processing, 2nd Edition. Springer International Publishing, Cham.

Jia, N., Fraenkel, H., Kagan, V., 2004. Effects of moisture conditioning methods on mechanical properties of injection molded nylon 6. Journal of Reinforced Plastics and Composites 23 (7), 729–737.

Jia, N., Kagan, V., 2001. Mechanical performance of polyamides with influence of moisture and temperature-accurate evaluation and better understanding. In: Moalli, J. (Ed.), Plastics Failure Analysis and Prevention. William Andrew, Norwich, pp. 95–104.

Johlitz, M., Steeb, H., Diebels, S., Chatzouridou, A., Batal, J., Possart, W., 2007. Experimental and theoretical investigation of nonlinear viscoelastic polyurethane systems. Journal of Materials Science 42 (23), 9894–9904.

Kaliske, M., Rothert, H., 1997. Formulation and implementation of three-dimensional viscoelasticity at small and finite strains. Computational Mechanics 19 (3), 228–239.

Kehrer, L., Keursten, J., Hirschberg, V., Böhlke, T., 2023. Dynamic mechanical analysis of PA 6 under hydrothermal influences and viscoelastic material modeling. Journal of Thermoplastic Composite Materials 36 (11), 4630–4664.

Keursten, J., Enders, S., Böhlke, T., 2025. Constitutive theory and simulation of entropy and enthalpy relaxation in the glass transition regime. Accepted for publication in Advanced Structured Materials .

Keursten, J., Kehrer, L., Böhlke, T., 2023. Linear and nonlinear thermoviscoelastic behavior of polyamide 6. Proceedings in Applied Mathematics and Mechanics 22 (1), e202200145.

Kießling, R., Ihlemann, J., 2020. The dependence of the viscoelastic properties of polyamide 6 on temperature and moisture content: experiment and modeling. Materials Today: Proceedings 32, 83–87.

Kohlrausch, R., 1854. Theory of the electric residue in the Leyden jar. Annalen der Physik und Chemie 91, 179–213.

Kovacs, A., Aklonis, J., Hutchinson, J., Ramos, A., 1979. Isobaric volume and enthalpy recovery of glasses. II. A transparent multiparameter theory. Journal of Polymer Science: Polymer Physics Edition 17 (7), 1097–1162.

Krawietz, A., 1986. Materialtheorie. Springer-Verlag, Berlin.

Lai, J., Bakker, A., 1996. 3-D Schapery representation for non-linear viscoelasticity and finite element implementation. Computational Mechanics 18 (3), 182–191.

Lim, L., Britt, I., Tung, M., 1999. Sorption and transport of water vapor in nylon 6,6 film. Journal of Applied Polymer Science 71 (2), 197–206.

Lion, A., 1997. On the thermodynamics of fractional damping elements. Continuum Mechanics and Thermodynamics 9 (2), 83–96.

Lion, A., 2007. Einführung in die Lineare Viskoelastizität. Vol. 4/07 of Beiträge zur Materialtheorie. Univ.-Prof. Dr.-Ing. habil. Alexander Lion, Universität der Bundeswehr München.

Lion, A., Johlitz, M., 2016. A thermodynamic approach to model the caloric properties of semicrystalline polymers. Continuum Mechanics and Thermodynamics 28 (3), 799–819.

Lion, A., Mittermeier, C., Johlitz, M., 2017. Heat capacities and volumetric changes in the glass transition range: a constitutive approach based on the standard linear solid. Continuum Mechanics and Thermodynamics 29 (5), 1061–1079.

Liu, G., Li, L., Zheng, Y., Zuo, Y., 2013. Temperature gradient in sample and its effect on enthalpy relaxation model fitting of polystyrene. Journal of Non-Crystalline Solids 365, 13–22.

Liu, I., 2002. Continuum Mechanics. Advanced Texts in Physics. Springer-Verlag, Berlin.

Loy, R., de Hoog, F., Anderssen, R., 2015. Interconversion of Prony series for relaxation and creep. Journal of Rheology 59 (5), 1261–1270.

Luk-Cyr, J., Crochon, T., Li, C., Lévesque, M., 2013. Interconversion of linearly viscoelastic material functions expressed as prony series: A closure. Mechanics of Time-Dependent Materials 17 (1), 53–82.

Maiti, A., 2016. A geometry-based approach to determining time-temperature superposition shifts in aging experiments. Rheologica Acta 55 (1), 83–90.

Marsden, J., Hoffman, M., 1999. Basic Complex Analysis, 3rd Edition. W. H. Freeman and Company, New York.

Menard, K., 2008. Dynamic Mechanical Analysis. CRC Press, Boca Raton.

Menges, G., Haberstroh, E., Michaeli, W., Schmachtenberg, E., 2011. Menges Werkstoffkunde Kunststoffe, 6th Edition. Carl Hanser Verlag, München.

Mittermeier, C., 2017. Beitrag zur kontinuumsmechanischen Modellierung des Glasübergangs und der daraus resultierenden physikalischen Alterung. Doctoral Thesis, Department of Aerospace Engineering, University of the Bundeswehr Munich .

Monson, L., Braunwarth, M., Extrand, C., 2008. Moisture absorption by various polyamides and their associated dimensional changes. Journal of Applied Polymer Science 107 (1), 355–363.

Moynihan, C., Macedo, P., Montrose, C., Gupta, P., DeBolt, M., Dill, J., Dom, B., Drake, P., Easteal, A., Elterman, P., Moeller, R., Sasabe, H., Wilder, J., 1976. Structural relaxation in vitreous materials. Annals of the New York Academy of Sciences 279 (1), 15–35.

Müller, I., 2001. Grundzüge der Thermodynamik, 3rd Edition. Springer-Verlag, Berlin.

Narayanaswamy, O., 1971. A model of structural relaxation in glass. Journal of the American Ceramic Society 54 (10), 491–498.

Naya, S., Meneses, A., Tarrío-Saavedra, J., Artiaga, R., López-Beceiro, J., Gracia-Fernández, C., 2013. New method for estimating shift factors in time-temperature superposition models. Journal of Thermal Analysis and Calorimetry 113 (2), 453–460.

Ngai, K., 1999. Modification of the Adam-Gibbs model of glass transition for consistency with experimental data. The Journal of Physical Chemistry B 103 (28), 5895–5902.

Nikonov, A., Davies, A., Emri, I., 2005. The determination of creep and relaxation functions from a single experiment. Journal of Rheology 49 (6), 1193–1211.

Oseli, A., Aulova, A., Gergesova, M., Emri, I., 2016. Time-temperature superposition in linear and non-linear domain. Materials Today: Proceedings 3 (4), 1118–1123.

Oskui, I., Hashemi, A., 2016. Dynamic tensile properties of bovine periodontal ligament: A nonlinear viscoelastic model. Journal of Biomechanics 49 (5), 756–764.

Papanicolaou, G., Xepapadaki, A., Karagounaki, K., Zaoutsos, S., 2008. Time and temperature effect on the linear-nonlinear viscoelastic transition threshold of a polymeric system. Journal of Applied Polymer Science 108 (1), 640–649.

Park, S., Schapery, R., 1999. Methods of interconversion between linear viscoelastic material functions. Part I - a numerical method based on Prony series. International Journal of Solids and Structures 36 (11), 1653–1675.

Pettermann, H., DeSimone, A., 2018. An anisotropic linear thermo-viscoelastic constitutive law. Mechanics of Time-Dependent Materials 22 (4), 421–433.

Picard, E., Gérard, J., Espuche, E., 2008. Water transport properties of polyamide 6 based nanocomposites prepared by melt blending: On the importance of the clay dispersion state on the water transport properties at high water activity. Journal of Membrane Science 313 (1-2), 284–295.

Preda, F., Alegria, A., Bocahut, A., Fillot, L., Long, D., Sotta, P., 2015. Investigation of water diffusion mechanisms in relation to polymer relaxations in polyamides. Macromolecules 48 (16), 5730–5741.

Reimschuessel, H., 1978. Relationships on the effect of water on glass transition temperature and Young's modulus of nylon 6. Journal of Polymer Science: Polymer Chemistry Edition 16 (6), 1229–1236.

Rouleau, L., Deü, J., Legay, A., Le Lay, F., 2013. Application of Kramers-Kronig relations to time-temperature superposition for viscoelastic materials. Mechanics of Materials 65, 66–75.

Rouse, P., 1953. A theory of the linear viscoelastic properties of dilute solutions of coiling polymers. The Journal of Chemical Physics 21 (7), 1272–1280.

Sakatsuji, W., Konishi, T., Miyamoto, Y., 2013. Enthalpy relaxation and annealing effect in polystyrene. Physical Review E 88 (1), 012605.

Sambale, A., Kurkowski, M., Stommel, M., 2019. Determination of moisture gradients in polyamide 6 using stepscan DSC. Thermochimica Acta 672, 150–156.

Sambale, A., Maisl, M., Herrmann, H., Stommel, M., 2021a. Characterisation and modelling of moisture gradients in polyamide 6. Polymers 13 (18), 3141.

Sambale, A., Stanko, M., Emde, J., Stommel, M., 2021b. Characterisation and FE modelling of the sorption and swelling behaviour of polyamide 6 in water. Polymers 13 (9), 1480.

Sanditov, D., Ojovan, M., 2017. On relaxation nature of glass transition in amorphous materials. Physica B: Condensed Matter 523, 96–113.

Schapery, R., 1969. On the characterization of nonlinear viscoelastic materials. Polymer Engineering and Science 9 (4), 295–310.

Schapery, R., Park, S., 1999. Methods of interconversion between linear viscoelastic material functions. Part II - an approximate analytical method. International Journal of Solids and Structures 36 (11), 1677–1699.

Scherer, G., 1984. Use of Adam-Gibbs equation in the analysis of structural relaxation. Journal of the American Ceramic Society 67 (7), 504–511.

Scott, D., Lai, J., Zureick, A., 1995. Creep behavior of fiber-reinforced polymeric composites: A review of the technical literature. Journal of Reinforced Plastics and Composites 14 (6), 588–617.

Serra-Aguila, A., Puigoriol-Forcada, J., Reyes, G., Menacho, J., 2019. Viscoelastic models revisited: characteristics and interconversion formulas for generalized Kelvin-Voigt and Maxwell models. Acta Mechanica Sinica 35 (6), 1191–1209.

Serra-Aguila, A., Puigoriol-Forcada, J., Reyes, G., Menacho, J., 2022. Estimation of tensile modulus of a thermoplastic material from dynamic mechanical analysis: Application to polyamide 66. Polymers 14 (6), 1210.

Sharma, P., Diebels, S., 2021. A mixture theory for the moisture transport in polyamide. Continuum Mechanics and Thermodynamics 33 (4), 1891–1905.

Sharma, P., Sambale, A., Stommel, M., Maisl, M., Herrmann, H., Diebels, S., 2020. Moisture transport in PA6 and its influence on the mechanical properties. Continuum Mechanics and Thermodynamics 32 (2), 307–325.

Sihn, S., Tsai, S., 1999. Automated shift for time-temperature superposition. In: Proceedings of the 1999 International Conference on Composite Materials, Paris, France.

Šilhavý, M., 1997. The Mechanics and Thermodynamics of Continuous Media. Texts and Monographs in Physics. Springer-Verlag, Berlin.

Simon, S., 1997. Enthalpy recovery of poly(ether imide): Experiment and model calculations incorporating thermal gradients. Macromolecules 30 (14), 4056–4063.

Simon, S., Sobieski, J., Plazek, D., 2001. Volume and enthalpy recovery of polystyrene. Polymer 42 (6), 2555–2567.

Sodeifian, G., Haghtalab, A., 2004. Discrete relaxation spectrum and K-BKZ constitutive equation for PVC, NBR and their blends. Applied Rheology 14 (4), 180–189.

Sorvari, J., Malinen, M., 2007. Numerical interconversion between linear viscoelastic material functions with regularization. International Journal of Solids and Structures 44 (3-4), 1291–1303.

Starkova, O., Papanicolaou, G., Xepapadaki, A., Aniskevich, A., 2011. A method for determination of time- and temperature-dependences of stress threshold of linear-nonlinear viscoelastic transition: Energy-based approach. Journal of Applied Polymer Science 121 (4), 2187–2192.

Stommel, M., Stojek, M., Korte, W., 2018. FEM zur Berechnung von Kunststoff- und Elastomerbauteilen, 2nd Edition. Carl Hanser Verlag, München.

Svoboda, R., Málek, J., 2013. Description of enthalpy relaxation dynamics in terms of TNM model. Journal of Non-Crystalline Solids 378, 186–195.

Tammann, G., Hesse, W., 1926. Die Abhängigkeit der Viscosität von der Temperatur bei unterkühlten Flüssigkeiten. Zeitschrift für Anorganische und Allgemeine Chemie 156 (1), 245–257.

Tool, A., 1945. Relaxation of stresses in annealing glass. Journal of Research of the National Bureau of Standards 34, 199–211.

Tropin, T., Schmelzer, J., Schick, C., 2011a. On the dependence of the properties of glasses on cooling and heating rates. Journal of Non-Crystalline Solids 357 (4), 1291–1302.

Tropin, T., Schmelzer, J., Schick, C., 2011b. On the dependence of the properties of glasses on cooling and heating rates II. Journal of Non-Crystalline Solids 357 (4), 1303–1309.

Tropin, T., Schulz, G., Schmelzer, J., Schick, C., 2015. Heat capacity measurements and modeling of polystyrene glass transition in a wide range of cooling rates. Journal of Non-Crystalline Solids 409, 63–75.

Troyer, K., Shetye, S., Puttlitz, C., 2012. Experimental characterization and finite element implementation of soft tissue nonlinear viscoelasticity. Journal of Biomechanical Engineering 134 (11), 114501.

Tschoegl, N., 1989. The Phenomenological Theory of Linear Viscoelastic Behavior. Springer-Verlag, Berlin.

Tschoegl, N., Knauss, W., Emri, I., 2002a. The effect of temperature and pressure on the mechanical properties of thermo- and/or piezorheologically simple polymeric materials in thermodynamic equilibrium - a critical review. Mechanics of Time-Dependent Materials 6 (1), 53–99.

Tschoegl, N., Knauss, W., Emri, I., 2002b. Poisson's ratio in linear viscoelasticity - a critical review. Mechanics of Time-Dependent Materials 6 (1), 3–51.

van Gurp, M., Palmen, J., 1998. Time-temperature superposition for polymeric blends. Rheology Bulletin 67 (1), 5–8.

Venoor, V., Park, J., Kazmer, D., Sobkowicz, M., 2021. Understanding the effect of water in polyamides: a review. Polymer Reviews 61 (3), 598–645.

Vlasveld, D., Groenewold, J., Bersee, H., Picken, S., 2005. Moisture absorption in polyamide-6 silicate nanocomposites and its influence on the mechanical properties. Polymer 46 (26), 12567–12576.

Vogel, H., 1921. Das Temperaturabhängigkeitsgesetz der Viskosität von Flüssigkeiten. Physikalische Zeitschrift 22, 645–646.

Walter, H., Dermitzaki, E., Wunderle, B., Michel, B., 2010. Influence of moisture on humidity sensitive material parameters of polymers used in microelectronic applications. In: 3rd Electronic System-Integration Technology Conference ESTC. IEEE, Piscataway, NJ.

Wetzel, P., Sambale, A., Uhlig, K., Stommel, M., Schneider, B., Kaiser, J., 2023. Hygromechanical behavior of polyamide 6.6: Experiments and modeling. Polymers 15 (16), 3387.

Weyer, S., Merzlyakov, M., Schick, C., 2001. Application of an extended Tool-Narayanaswamy-Moynihan model. Part 1. Description of vitrification and complex heat capacity measured by temperature-modulated DSC. Thermochimica Acta 377 (1-2), 85–96.

Weyer, S., Merzlyakov, M., Schick, C., 2005. Application of an extended Tool-Narayanaswamy-Moynihan model. Part 2. Frequency and cooling rate dependence of glass transition from temperature-modulated DSC. Polymer 46 (26), 12240–12246.

Whittaker, E., 1918. On the numerical solution of integral-equations. Proceedings of the Royal Society A 94 (662), 367–383.

Williams, G., Watts, D., 1970. Non-symmetrical dielectric relaxation behaviour arising from a simple empirical decay function. Transactions of the Faraday Society 66, 80–85.

Williams, M., Landel, R., Ferry, J., 1955. The temperature dependence of relaxation mechanisms in amorphous polymers and other glass-forming liquids. Journal of the American Chemical Society 77 (14), 3701–3707.

Xu, Q., Engquist, B., Solaimanian, M., Yan, K., 2020. A new nonlinear viscoelastic model and mathematical solution of solids for improving prediction accuracy. Scientific Reports 10 (1), 2202.

Zink, T., 2021. Thermomechanische Modellierung von Polyamid 6. Bachelor Thesis, Institute of Engineering Mechanics, Chair for Continuum Mechanics, Karlsruhe Institute of Technology (KIT) .

Zink, T., Kehrer, L., Hirschberg, V., Wilhelm, M., Böhlke, T., 2022. Nonlinear Schapery viscoelastic material model for thermoplastic polymers. Journal of Applied Polymer Science 139 (17), e52028.

Zocher, M., Groves, S., 1997. A three-dimensional finite element formulation for thermoviscoelastic orthtropic media. International Journal for Numerical Methods in Engineering 40 (12), 2267–2288.

Schriftenreihe Kontinuumsmechanik im Maschinenbau
Karlsruher Institut für Technologie (KIT)
(ISSN 2192-693X)

Band 1 Felix Fritzen
Microstructural modeling and computational homogenization of the physically linear and nonlinear constitutive behavior of micro-heterogeneous materials.
ISBN 978-3-86644-699-1

Band 2 Rumena Tsotsova
Texturbasierte Modellierung anisotroper Fließpotentiale.
ISBN 978-3-86644-764-6

Band 3 Johannes Wippler
Micromechanical finite element simulations of crack propagation in silicon nitride.
ISBN 978-3-86644-818-6

Band 4 Katja Jöchen
Homogenization of the linear and non-linear mechanical behavior of polycrystals.
ISBN 978-3-86644-971-8

Band 5 Stephan Wulfinghoff
Numerically Efficient Gradient Crystal Plasticity with a Grain Boundary Yield Criterion and Dislocation-based Work-Hardening.
ISBN 978-3-7315-0245-6

Band 6 Viktor Müller
Micromechanical modeling of short-fiber reinforced composites.
ISBN 978-3-7315-0454-2

Die Bände sind unter www.ksp.kit.edu als PDF frei verfügbar oder als Druckausgabe bestellbar.

Band 7 Florian Rieger
Work-hardening of dual-phase steel.
ISBN 978-3-7315-0513-6

Band 8 Vedran Glavas
Micromechanical Modeling and Simulation of Forming Processes.
ISBN 978-3-7315-0602-7

Band 9 Eric Bayerschen
Single-crystal gradient plasticity with an accumulated plastic slip: Theory and applications.
ISBN 978-3-7315-0606-5

Band 10 Bartholomäus Brylka
Charakterisierung und Modellierung der Steifigkeit von langfaserverstärktem Polypropylen.
ISBN 978-3-7315-0680-5

Band 11 Rudolf Neumann
Two-Scale Thermomechanical Simulation of Hot Stamping.
ISBN 978-3-7315-0714-7

Band 12 Mauricio Lobos Fernández
Homogenization and materials design of mechanical properties of textured materials based on zeroth-, first- and second-order bounds of linear behavior.
ISBN 978-3-7315-0770-3

Band 13 Malte Schemmann
Biaxial Characterization and Mean-field Based Damage Modeling of Sheet Molding Compound Composites.
ISBN 978-3-7315-0818-2

Band 14 Jürgen Albiez
Finite element simulation of dislocation based plasticity and diffusion in multiphase materials at high temperature.
ISBN 978-3-7315-0918-9

Die Bände sind unter www.ksp.kit.edu als PDF frei verfügbar oder als Druckausgabe bestellbar.

Band 15 Maria Loredana Kehrer
Thermomechanical Mean-Field Modeling and Experimental Characterization of Long Fiber-Reinforced Sheet Molding Compound Composites.
ISBN 978-3-7315-0924-0

Band 16 Peter Hölz
A dynamic and statistical analysis of the temperature- and fatigue behavior of a race power unit – The effect of different thermodynamic states.
ISBN 978-3-7315-0988-2

Band 17 Andreas Prahs
A Gradient Crystal Plasticity Theory Based on an Extended Energy Balance.
ISBN 978-3-7315-1025-3

Band 18 Johannes Ruck
Modeling martensitic phase transformation in dual phase steels based on a sharp interface theory.
ISBN 978-3-7315-1072-7

Band 19 Hannes Erdle
Modeling of Dislocation - Grain Boundary Interactions in Gradient Crystal Plasticity Theories.
ISBN 978-3-7315-1196-0

Band 20 Johannes Görthofer
Microstructure generation and micromechanical modeling of sheet molding compound composites.
ISBN 978-3-7315-1205-9

Band 21 Daniel Wicht
Efficient fast Fourier transform-based solvers for computing the thermomechanical behavior of applied materials.
ISBN 978-3-7315-1220-2

Band 22 Juliane Lang
Thermomechanical Modeling and Experimental Characterization of Sheet Molding Compound Composites.
ISBN 978-3-7315-1232-5

Die Bände sind unter www.ksp.kit.edu als PDF frei verfügbar oder als Druckausgabe bestellbar.

Band 23 Julian Karl Bauer
Fiber Orientation Tensors and Mean Field Homogenization: Application to Sheet Molding Compound.
ISBN 978-3-7315-1262-2

Band 24 Sebastian Gajek
Deep material networks for efficient scale-bridging in thermomechanical simulations of solids.
ISBN 978-3-7315-1278-3

Band 25 Jannick Kuhn
Microstructure modeling and crystal plasticity parameter identification for predicting the cyclic mechanical behavior of polycrystalline metals.
ISBN 978-3-7315-1272-1

Band 26 Felix Ernesti
A computational multi-scale approach for brittle materials.
ISBN 978-3-7315-1285-1

Band 27 Patrick Arthur Hessman
On multi-scale modeling of fatigue in short glass fiber reinforced thermoplastics.
ISBN 978-3-7315-1398-8

Band 28 Benedikt Sterr
Machine learning aided multiscale mechanics of fiber suspensions.
ISBN 978-3-7315-11421-3

Band 29 Maximilian Krause
Local Stresses and Strains in Polycrystals.
ISBN 978-3-7315-1411-4

Band 30 Johannes Keursten
Thermoviscoelastic Modeling of Thermoplastic Polymers.
ISBN 978-3-7315-1422-0

When considering the thermomechanical behavior of thermoplastic polymers, the glass transition is a central phenomenon associated with significant changes of the material parameters and process-dependent behavior. To model these effects, first, an introduction on the theory of linear thermoviscoelasticity is given. Generalized thermorheological models are presented within the framework of linear irreversible thermodynamics. An analogy between viscoelastic stress relaxation and caloric entropy relaxation is shown. The viscoelastic part of the model is discussed in detail by considering the viscoelastic behavior of polyamide 6 under hydrothermal influences. Application and limitations of time-temperature superposition and generalized Maxwell model are discussed based on experimental temperature-frequency sweeps. The influence of humidity is considered by a humidity-dependent reference temperature. Last, the caloric part of the models is applied to heating and cooling curves of the heat capacity of polystyrene in the vicinity of the glass transition. Compared to the literature, a simplified model with an internal temperature as internal variable is considered. The evolution of the internal variable depends on temperature and temperature rate. A stepwise parameter identification regarding equilibrium and glassy state, and glass transition regime is discussed.

ISSN 2192-693X
ISBN 978-3-7315-1422-0

Gedruckt auf FSC-zertifiziertem Papier